Final Report, June 5, 2006

On

Feasibility of an Ultrasonic Based Instrument for Assessing In-situ Pipeline Coatings

Contract Number DTRT57-06-C-10005
Project # 186

DOT SBIR PROGRAM OFFICE, DTS-22
U.S. Department of Transportation
Volpe National Transportation Systems Center
55 Broadway
Cambridge, MA 02142-1093

Mr. James Merritt
R&D Program Manager
Office of Pipeline Safety
793 Countrybriar Lane
Denver, CO 80129

Mr. Joseph Kelly
New Contract Administrator
US DOT/RITA/Volpe Center
55 Broadway
Cambridge, MA 02142-1093

By
FBS, Inc.
143 Hawbaker Industrial Dr., Suite 102
State College, Pennsylvania 16803
(814) 234-3437
fbsworldwide.com

Contacts: Mike Avioli, Mavioli@fbsworldwide.com
Joe Rose, Jrose@fbsworldwide.com
Jason Van Velsor, Jkv2@psu.edu

Executive Summary

Ultrasonic guided-waves offer a brilliant solution for the efficient nondestructive evaluation of inaccessible pipeline. Overwhelming demand of this relatively young technology has led to a rapid transfer from its experimental beginnings to commercial application. While defect detection and localization techniques have been mastered for bare pipe conditions, virtually all pipe used in the energy transmission industry have some variation of protective coating applied to the outer surface. Until this point, inspection outfits relied on brute force to inspect pipeline with highly viscoelastic coatings. This lack of finesse presents a problem as special consideration of the coating material can lead to altered inspection parameters which, in-turn, lead to increased defect sensitivity and penetration power.

The primary reason for the disregard of coating effects is a lack of practical means by which to obtain the material properties of the coating. With this motivation, FBS, inc. has proposed the development of an in-situ coating evaluation instrument whose end-product will be the optimal guided-wave inspection parameters for the specific pipe and coating under investigation. Such a tool would also be useful for the creation of a coating database, which would include such information as coating properties, age, and details on the environment to which the coating was subject.

FBS, inc. has gone beyond the stage of feasibility testing and has begun prototyping an instrument for in-situ coating evaluation. The instrument works on a test protocol, developed as part of the Phase I effort, which can be viewed in detail in this report. A conceptualization and photograph of the tool's, first generation, sensor package can be seen in Figure 1. This sensor package will be incorporated with a handheld excitation and processing device pending Phase II funding.

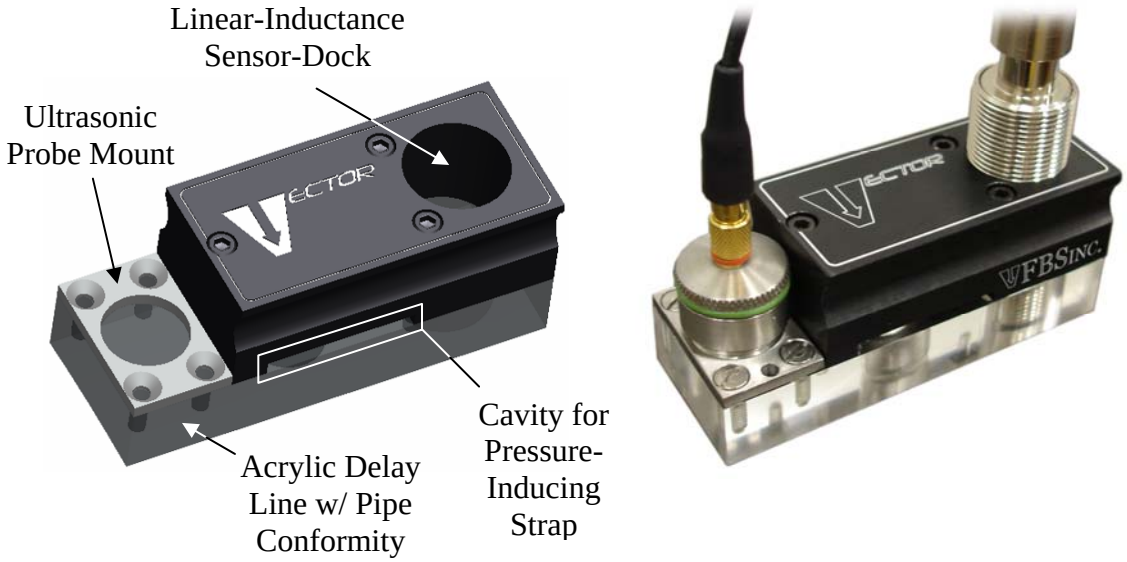

Figure 0.1. Conceptualization and photograph of completed, first generation, sensor package for in-situ coating property measurement.

The prototype tool, VECTOR, was field tested at NY Search testing facility in Johnson City, New York with very encouraging results. These results are presented within this report. A proof-of-concept study regarding the property measurement techniques is also contained herein.

Additional studies were carried out on eight different pipe specimens, each with a different coating and one reference pipe with no coating. Coatings were applied to 10ft. sections of 4in. diameter pipe. Detailed descriptions of the coatings can be found within the report. Using these specimens, attenuation, focusing, and interface studies were performed. Based on the measured material properties numerical models were generated and were in good agreement with the observed experimental results.

Overall, the measurement techniques and prototype tool developed throughout the tenure of the Phase I effort, have produced results meriting the continuation of the development of a fully portable, in-situ coating evaluation instrument. The type of inspection guidance provided by such an instrument would be invaluable for generating increased penetration power and defect sensitivity. Considerable interest in this tool has already been shown by representatives from several major energy transmission companies, including ConEdison, Rochester G&E, and PECO, with several of these companies expressing interest in providing additional coated pipe specimens for evaluation.

Table of Contents

List of Figures

Figure 6.2 Phase velocity dispersion curve for a pipe with B50 coating. Results are shown for the actual coating density, half actual-density, and double actual-density. The results show that variation in density has very little effect on phase velocity. A very small difference can be seen in the L(0,2) and T(0,1) modes for double the actual density. This suggests that errors in density measurement, as large as 100%, will have only a minor effect on phase velocity.

Figure 6.3 Attenuation dispersion curve for a pipe with B50 coating, illustrating the effect of variation in coating density. Results are shown for the actual coating density, half actual-density, and double actual-density. Results show that variations in density produce significant changes in the attenuation dispersion curves. For the L(0,2) and T(0,1) modes, the variation is relatively small at low frequencies with differences increasing with frequency. The L(0,1) modes appears to be sensitive to density changes even at low frequencies.

Figure 6.4 Phase velocity dispersion curve for a pipe with B50 coating, illustrating the effect of variation in coating thickness. Results are shown for the actual coating thickness, double actual-thickness, and triple actual-thickness. Results show that coating thickness has a noticeable effect on the L(0,2) and T(0,1) phase velocity dispersion curves, while the L(0,1) mode is unaffected. Though the variations in the curves are relatively small, they are noticeable and increase with frequency.

Figure 6.5 Attenuation dispersion curve for a pipe with B50 coating, illustrating the effect of variation in coating thickness. Results are shown for the actual coating thickness, double actual-thickness, and triple actual-thickness. Results show significant changes in the dispersion curves for different coating thicknesses. Variations for the L(0,2) and T(0,1) mode are relatively small at low frequencies and increase dramatically with frequency. The L(0,1) mode is very sensitive to coating thickness, even at low frequencies. This indicates that accurate measurement of coating thickness is critical.

Figure 6.6 Figure 6.5 with an expanded y-axis to better see the attenuation trends at higher frequencies. Results show regions where attenuation reaches a maximum and then begins to decrease again. This is very useful information for high-frequency guided-wave inspection.

Figure 6.7 Phase velocity dispersion curve for a pipe with B50 coating, illustrating the effect of variation in wave velocity. Results are shown for the ratio of shear velocity to longitudinal velocity. The actual ratio is plotted along with the common shear wave velocity approximation of $0.6C_L$ and a smaller approximation of $0.25C_L$. Results show virtually no change in phase velocity for any of the velocity ratios plotted.

Figure 6.8 Attenuation dispersion curve for a pipe with B50 coating, illustrating the effect of variation in wave velocity. Results are shown for the ratio of shear velocity to longitudinal velocity. The actual ratio is plotted along with the common shear wave velocity approximation of $0.6C_L$ and a smaller approximation of $0.25C_L$. Results show that the L(0,2) is relatively inert at low frequencies. The T(0,1) and L(0,1) modes are

more drastically affected at low frequencies. Varying the velocity ratio changes the shape of the attenuation dispersion curves rather than just scaling them.

Figure 6.9 Phase velocity dispersion curve for a pipe with B50 coating, illustrating the effect of variation in attenuation constants. Results are shown for the shear attenuation constant as a multiple of the longitudinal attenuation constant. The actual relationship is displayed as well as a smaller approximation of $\alpha_S=2\alpha_L$ and a larger approximation of $\alpha_S=10\alpha_L$. Results show that variation in bulk wave attenuation has no effect on phase velocity.

Figure 6.10 Attenuation dispersion curve for a pipe with B50 coating, illustrating the effect of variation in attenuation constants. Results are shown for the shear attenuation constant as a multiple of the longitudinal attenuation constant. The actual relationship is displayed as well as a smaller approximation of $\alpha_S=2\alpha_L$ and a larger approximation of $\alpha_S=10\alpha_L$. Results show that variations in bulk wave attenuation have a scaling effect on the attenuation dispersion curves. The effects of the variations increase monotonically with frequency for the range shown. Effects on L(0,2) and T(0,1) are minor at low frequencies.

Figure 7.1 Schematic of a handheld, ultrasonic, coating-evaluation tool.

Figure 7.2 Dimensions of VECTOR sensor package

Figure 7.3 Illustrated model of VECTOR device showing key design points

Figure 7.4 Photograph of Prototype VECTOR sensor-housing device.

Figure 7.5 LabView code and interface designed for control of the linear inductance sensor.

Figure 8.1 Photograph of VETOR tool on 12” diameter pipe with Fusion Bonded Epoxy coating.

Figure 8.2a RF Waveform showing multiple reflections from the coating-pipe interface.

Figure 8.2b Fourier Transforms of the reflected signals. The reference waveform is not shown in (1a).

Figure 8.3 Bulk wave attenuation trend for Fusion Bonded Epoxy coating on 12” diameter pipe.

Figure 8.4 Phase velocity dispersion curve for 12” diameter pipe with Fusion Bonded Epoxy coating.

Figure 8.5 Attenuation dispersion curve for 12” diameter pipe with Fusion Bonded Epoxy coating.

Figure 8.6a VECTOR tool on 16” diameter pipe with Fibrous Coal Tar coating.

Figure 8.7a RF Waveform showing single reflection from the coating-pipe interface.

Figure 8.7b Fourier Transforms of the reflected signals.

Figure 8.8 Bulk wave attenuation trend for Fibrous Coal Tar coating on 16” diameter pipe.

Figure 8.9 Phase velocity dispersion curve for 16” diameter pipe with Fibrous Coal Tar coating.

Figure 8.10 Attenuation dispersion curve for 16” diameter pipe with Fibrous Coal Tar coating.

Figure 10.1 7-cycle, Hanning-windowed, 40kHz toneburst used for L(0,2) mode generation.

Figure 10.2 Comparison of 40kHz, L(0,2) mode propagation in a bare pipe (top) and a wax coated pipe (bottom). The green dotted-lines represent forward propagation and the red dotted-lines represent backward propagation. These results show that in addition to being highly attenuative, the wax coating alters the group velocity of the wave propagating in the coated pipe.

Figure 10.3 Contracted view of pipe showing energy leakage from the pipe wall into the wax coating. The gray color represents energy saturation in reference to the scale shown.

Figure 10.4 Contracted view of pipe showing energy leakage from the pipe wall into the wax coating. The gray color represents energy saturation in reference to the scale shown. This means that the energy present in the pipe is much large than that in the coating.

Figure 10.5 RF waveform obtained from FEM analysis for bare pipe.

Figure 10.6 Analytic envelopes of bare pipe (black), 2LFBE coated pipe (blue), and wax tape coated pipe (red).

Figure 11.1 (a) Illustration of tool configuration for axisymmetric loading showing all transducers connected to one channel. (b) Tool configuration for focusing, which allows time delays (phasing) to be applied to individual channels.

Figure 11.2 (a) Illustration of distribution of wave energy for axisymmetric loading. (b) Illustration of distribution of wave energy for focusing via phased loading.

Figure 11.3 Experimental setup for guided wave focusing experiment.

Figure 11.4 Focusing results for a bare pipe. The plot on the left shows the difference in dB as referenced to the axisymmetric amplitude. The figure on the right shows the focusing profile.

Figure 11.5 Focusing results for pipe with a 0.2mm Bitumastic 50 coal-tar mastic coating. The plot on the left shows the difference in dB as referenced to the axisymmetric amplitude. The figure on the right shows the focusing profile.

Figure 11.6 Focusing results for pipe with 0.15mm Bitumastic 300M coal-tar epoxy coating. The plot on the left shows the difference in dB as referenced to the axisymmetric amplitude. The figure on the right shows the focusing profile.

Figure 11.7 Focusing results for pipe with cold-applied 0.8mm bitumen tape coating. The plot on the left shows the difference in dB as referenced to the axisymmetric amplitude. The figure on the right shows the focusing profile.

Figure 11.8 Focusing results for pipe with 0.25mm single layer fusion-bonded epoxy coating. The plot on the left shows the difference in dB as referenced to the axisymmetric amplitude. The figure on the right shows the focusing profile.

Figure 11.9 Focusing results for pipe with 1.5mm dual layer fusion-bonded epoxy coating. The plot on the left shows the difference in dB as referenced to the axisymmetric amplitude. The figure on the right shows the focusing profile.

Figure 11.10 Focusing results for pipe with 0.13mm enamel paint coating. The plot on the left shows the difference in dB as referenced to the axisymmetric amplitude. The figure on the right shows the focusing profile.

Figure 11.11 Focusing results for pipe with 2.5mm wax-wrap coating. The plot on the left shows the difference in dB as referenced to the axisymmetric amplitude. The figure on the right shows the focusing profile.

Figure 11.12 Illustration of the concept of penetration improvement with the use of focusing. The focusing response at 10 ft. is equivalent to the axisymmetric response at 5 ft. Thus 5 ft. of penetration has been gained.

Figure 12.1 (a) Experimental setup for coating interface study. (b) Clean Bitumen Tape as was removed from the pipe after the water interface study. (c) Soiled Bitumen Tape used to simulate a dirty bonding condition.

Figure 12.2 Analytic envelope of the RF waveform obtained from the L(0,2) mode propagating in a bare pipe. The red line is the analytic envelope. The blue line represents the echo-peak data, and the black line is a normalized exponential attenuation trend.

Figure 12.3 Attenuation trends of the L(0,2) mode for various coating interface conditions. The trends are labeled according to the interface (Int.) condition.

Figure 12.4 Attenuation trends of the T(0,1) mode for various coating interface conditions. The trends are labeled according to the interface (Int.) condition.

List of Tables

1. Introduction

To study the effects of different types of coatings on guided wave propagation and attenuation, and to develop an in situ material property measurement technique and device, seven different pipe coatings were obtained and applied to 10ft. sections of 4in. diameter pipe. Descriptions and photographs of these coating, along with the abbreviations which will be used throughout this report, are contained in Section 2. Information on coating type, manufacturer, and application process can be found here.

Sections 3 and 4 describe the techniques used to characterize the coating material properties. Section 3 provides detailed information regarding coating density measurement using bulk-wave ultrasound. Bulk-wave velocity measurement is also discussed. Section 4 contains details regarding bulk-wave attenuation measurement techniques for various coating thicknesses.

Section 5 presents a proof-of-concept study, showing that the material property measurement techniques described in Sections 3 and 4 provide reliable guided-wave attenuation predictions. In Section 5, a guided-wave attenuation experiment is presented in which attenuation data is extracted from actual experimental data. The experimentally obtained attenuation is then compared to the attenuation rates predicted using the measured coating properties. Results are in good agreement, therefore verifying the procedures described in Sections 3 and 4.

Section 6 offers a study of the effects of various input parameters on the theoretical phase velocity and attenuation dispersion curves. Here, the effects of coating thickness, density, wave velocity, and bulk-wave attenuation are examined. Dispersion curves are studied relative to the curves for a coal-tar mastic coating with known material properties. Such a study reveals the criticality of each parameter in the accurate determination of guided-wave velocity and attenuation properties and thus indicates which coating material properties must be measured with a high accuracy.

Sections 7 and 8 deal with the conceptualization, prototyping, and field testing of a first generation, in situ, coating evaluation instrument named VECTOR. Section 7 presents a hypothetical design for a handheld coating evaluation instrument that would result as part of a Phase II effort. A first-prototype of the sensor package portion of the device is presented with several key design features introduced. Section 8 presents the field-testing results of the sensor package. Field-testing was hosted by the Northeast Gas Association and took place at NY Search's testing grounds in Johnson City, NY from May 16th -19th, 2006.

Section 9 explains the calculation of the complex viscoelastic material properties of the coatings, which are needed for the finite-element modeling presented in Section 10. Section 10 introduces finite-element techniques for modeling wave propagation in pipe with viscoelastic coatings. The viscoelastic coating effects are visualized, showing changes in propagation velocity and increased guided-wave attenuation. Modeling results

are shown to agree well with the experimental and predicted trends described in Section 5.

Section 11 introduces the concepts and benefits of guided-wave focusing. An experimental investigation of the effects of coating on focusing ability is presented. The seven different coated specimens described in Section 2 were used for the investigation.

Section 12 illustrates the effect of coating bond and interface condition on guided-wave attenuation. Experimental data is presented for a bitumen tape coating with three different bonding conditions: a clean interface, a wetted interface, and a soiled interface. Each condition is representative of a circumstance which may appear in actual pipeline. The main goal of this study is to determine whether or not bond characterization need be included in the final design of a coating evaluation tool.

Finally, Section 13 provides a concise review of the major results presented within this report. Section 14 discusses some areas which will be studied further, possibly as part of a Phase II effort. Section 15 contains the detailed references of other's work, cited herein.

2. Coated-Pipe Specimen Descriptions

For experimental and theoretical comparison, a library of coated-pipe specimens was assembled. Coating materials were chosen based on diversity and availability with several of the coating being categorized as field-applied and several as factory-applied. In a factory process, pipe surfaces are generally sandblasted to published standards before the coating is applied. For field-applied coatings, sandblasting is often not possible and coatings are sometimes applied to somewhat crude surfaces. For this reason, factory-applied coatings are usually more complex in nature, requiring several processing steps.

To ensure uniformity amongst steel pipe specimens, ten 10 ft. lengths of 4 in. diameter schedule 40 pipes were obtained for coating. Field-applied coatings were applied in the laboratory while factory-applied coatings were outsourced for coating. Seven different coating types were applied, leaving one bare pipe for comparison reasons, and two pipes for bonding interface studies. The specimens are shown in Figures 2.1 and 2.2.

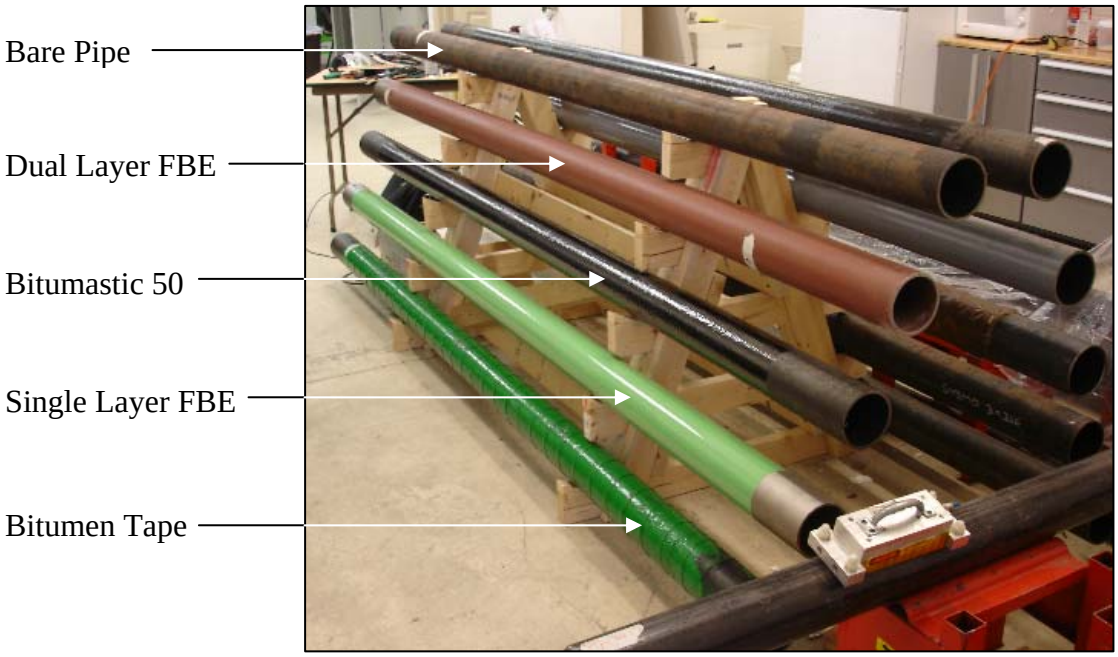

Figure 2.1 Photograph of 10 ft. Schedule 40 Steel pipe specimens which were used for experimental verification. Each Pipe is labeled with the type of coating that was applied to its outer surface.

Figure 2.2 Photograph of additional 10 ft. Schedule 40 Steel pipe specimens which were used for experimental verification. Each Pipe is labeled with the type of coating that was applied to its outer surface.

Table 2.1, on the following page, contains details on the different coatings, including manufacturer, coating type, and product description. The coating type abbreviations listed in the table will be used throughout this report.

Coating	Type	Abrv.	Field or Factory Applied	Product Description
3M Scotchkote 6233	Dual Layer Fusion Bonded Epoxy (FBE)	2LFBE	Factory	*6233* - One-part, heat curable, thermosetting epoxy coating powder designed for corrosion protection of pipe
3M Scotchkote 6352				*6352* - A Fusion Bonded Epoxy Dual Coating System that is a hard, mechanically strong top coating for all Scotchkote fusion bonded pipeline corrosion protection coatings
Carboline Bitumastic 50	Bitumen Paint	B50	Field	Ultra-high build, single-component coal tar mastic for protecting steel and concrete substrates subject to aggressive conditions and for below grade damp proofing requirements
3M Scotchkote 413	Single Layer Fusion Bonded Epoxy (FBE)	1LFBE	Factory	One-part, heat curable, thermosetting epoxy coating designed for the protection of reinforcing steel
Royston One-Step Tape	Bitumen Tape	BT	Field	Cold-applied, state-of-the-art pressure sensitive pipe wrap, that requires no primer and is designed for wrapping steel pipes, joints, fittings and valves for protection against above and below ground corrosion. It is the result of an extensive research program in which the latest developments in materials were utilized.
Carboline Bitumastic 300M	Bitumen Epoxy	B300M	Field or Factory	Renowned high build coal tar epoxy for protection for steel and concrete in single or two-coat applications in a broad variety of aggressive industrial applications.
Rust-oleum High Performance Protective Enamel	Enamel Paint	EP	Field or Factory	Oil-based Enamel ideal for corrosion prevention when applied directly to metal surface
Trenton Wax Tape #1	Wax Tape	WT	Field	Wax-Tape is a plastic-fiber felt, saturated with a blend of microcrystalline waxes, plasticizers and corrosion inhibitors, forming a tape wrapper. Ideal because of its excellent conformability over irregular surfaces.

Table 2.1 Information regarding the different types of coatings that were used to coat the pipe specimens. Coatings that are categorized as being field or factory-applied were actually applied in the laboratory and not in a factory.

3. Coating Density Measurement Using Bulk Wave Ultrasound

Reflection measurements are very useful for determining the properties of a material if the properties on side of the interface are previously known. Chapters 4 and 5 of Rose [1999] and Chapter 5 of Graff [1975] provide an excellent review of reflection fundamentals. Following Rose with the interface conditions illustrated in Figure 3.1,

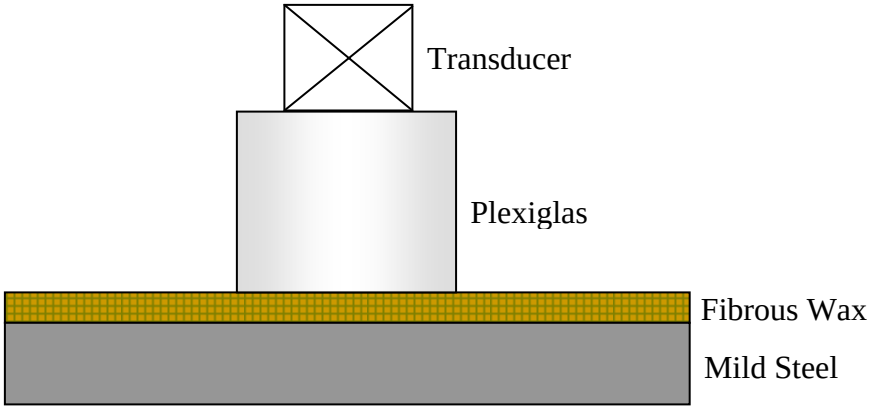

Figure 3.1 Experimental setup for the in-situ density measurement of a Fibrous Wax coating

the reflection coefficient between the Plexiglas delay line and the Fibrous Wax coating is described by Eq. [3.1],

$$R_{plexi/wax} = \frac{W_{wax} - W_{plexi}}{W_{wax} + W_{plexi}}, \qquad [3.1]$$

where W is the acoustic impedance of the respective materials and can be calculated using Eq. [3.2],

$$W = \rho c_L . \qquad [3.2]$$

Therefore, if the acoustic properties of the Plexiglas are known, the density of the Fibrous Wax coating can be determined from Eq. [3.3],

$$\rho_{wax} = \frac{c_{plexi}\rho_{plexi}(R_{plexi/wax} + 1)}{c_{wax}(1 - R_{plexi/wax})}, \qquad [3.3]$$

if the longitudinal wave velocity and reflection coefficient can be measured by experiment. The process for obtaining the longitudinal wave velocity and Plexi/Wax reflection coefficient are described in the following sections.

Velocity Measurement

Longitudinal velocity can be easily measured from time-of-flight information. An assumption for this process is that the longitudinal velocity is constant with frequency. This will be assumed for now and verified in the next section.

In order to measure the longitudinal velocity in the Fibrous Wax, two sets of data were taken, the difference between the two being the thickness of the wax coating. Data was collected using a spike-pulse excitation and a 5MHz highly-damped broadband transducer. The analytic envelopes of the RF waveforms were calculated in order to precisely locate peaks.

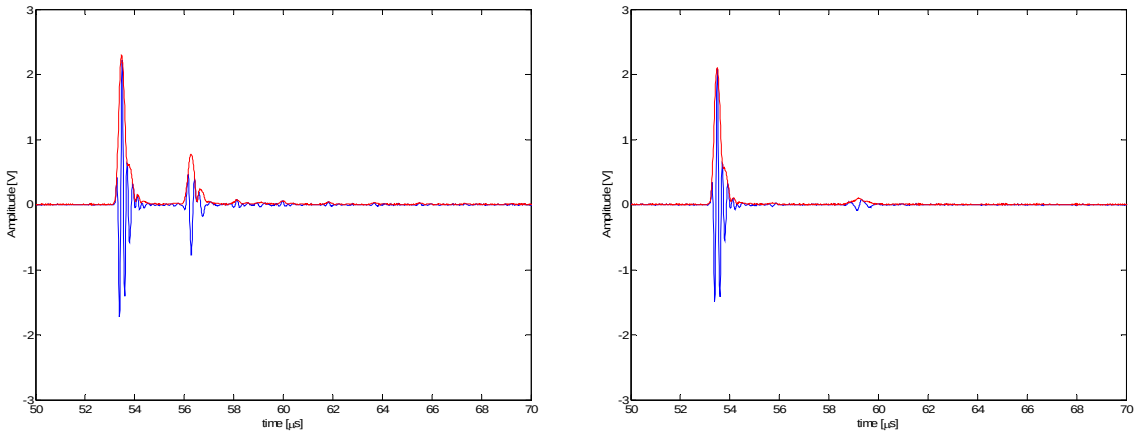

Figure 3.2 RF waveforms and analytic envelopes of pulse echo data collected from a Fibrous Wax coating. The plot on the left corresponds to a coating thickness of 2.4mm and the plot on the right corresponds to a coating thickness of 4.8mm.

The coating thickness was measured to an accuracy of 0.1mm using a linear inductance, dry-film thickness gauge. The linear inductance sensor allows for in-situ coating thickness measurement with access to only on side of the coating. The calculated longitudinal velocity of the Fibrous Wax was found to be,

$$c_{Lwax} = 1.6 \ \ mm/\mu s \qquad [3.4]$$

Plexi/Wax Reflection Coefficient Measurement

With the longitudinal velocity of the wax known, the reflection coefficient from the plexi-wax interface must be measured. There are several methods by which to gather this information. Since acoustic properties of viscoelastic materials often vary with frequency, it is desirable to measure the reflection coefficient as a function of frequency. For this reason, amplitude information will be gathered from the frequency domain as opposed to the time domain. If the ultrasonic pulse is broadbanded, information about the reflection coefficient can be gathered over a significant frequency range.

When the incident pulse p_I encounters the plexi-wax interface, the reflected portion of the pulse can be expressed as,

$$p_R(t) = p_I(t)R_{plexi/wax}. \qquad [3.5]$$

If the Plexiglas delay line is exposed to air, as opposed to being put on the coating, then the reflection coefficient from the plexi-air interface, $R_{plexi/air}$, can be approximated as being unity and the reflected wave has an amplitude equal to that of the incident pulse, minus any attenuation caused by the Plexiglas material. This is equivalent to measuring P_I in Eq. [3.5]. Therefore, the reflection coefficient can be approximated as being the ratio of the signal amplitude of the plexi-wax case to the amplitude of the plexi-air case.

$$R_{plexi/wax} = -\frac{p_R(t)}{p_0(t)} \qquad [3.6]$$

The negative sign accounts for the 180° phase shift that occurs at the plexi-air interface. Since the Plexiglas delay line is present in both measurements, any attenuation introduced by the material is deconvolved when calculating Eq. [3.6], and therefore will not affect the final calculation of $R_{plexi/wax}$.

By taking the Fourier Transform of the reflected pulses, the reflection coefficient as a function of frequency can be obtained. Therefore,

$$R_{plexi/wax}(f) = -\frac{\int_{-\infty}^{\infty} p_R(t)e^{-j2\pi ft}dt}{\int_{-\infty}^{\infty} p_0(t)e^{-j2\pi ft}dt}. \qquad [3.7]$$

The FFT's of p_R and p_0 are shown in Figure 3.3.

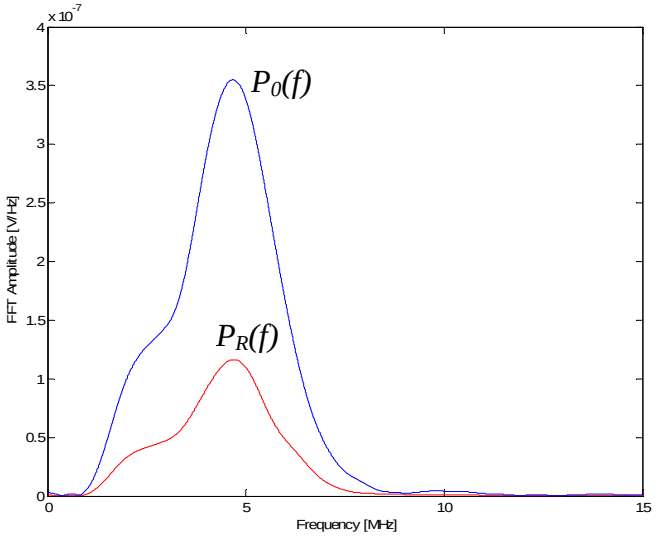

Figure 3.3 Fourier Transform of the plexi-air reference signal (blue) and of the reflected signal from the plexi-wax interface.

Given the two frequency spectrums in Figure 3.3, the reflection coefficient as a function of frequency can be calculated as in Eq. [3.7]. This is shown in Figure 3.4.

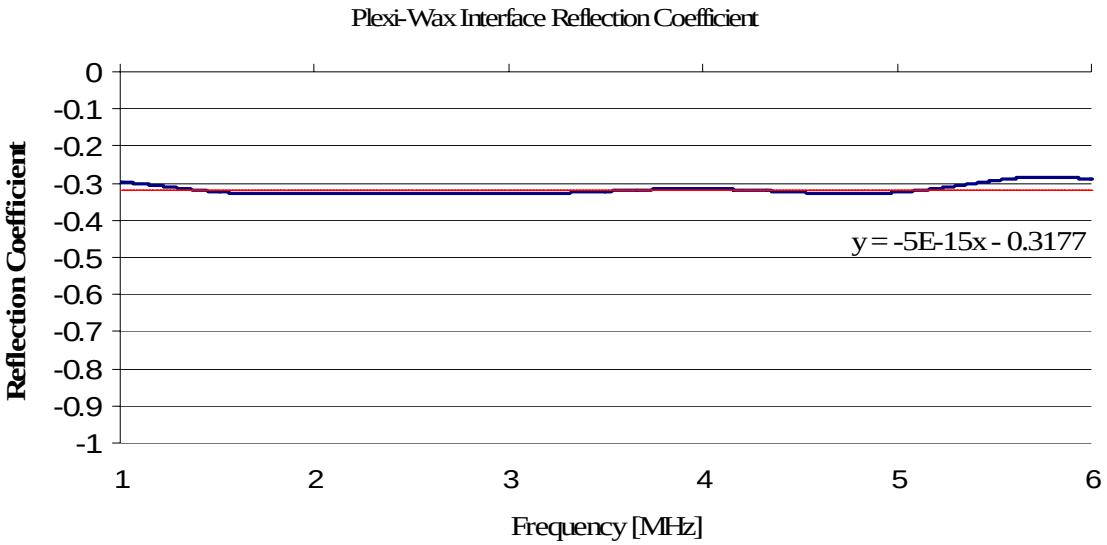

Figure 3.4 Reflection coefficient of a Plexiglas – Fibrous Wax interface, shown as a function of frequency. The blue line represents the ratio of the spectrums and the red dotted line is the average value over this frequency range.

The reflection coefficient data shown in Figure 3.4 is relatively constant over this particular frequency range. Since the density and velocity in the Plexiglas are assumed constant, and the density of the wax is also constant, the only reason that there would be a non-constant trend in the reflection coefficient would be if the longitudinal velocity of the wax was a function of frequency. Therefore, the constant velocity assumption that was made in the previous section is valid. In Figure 3.4, the red dotted line represents the average value over the 1-6 MHz range. The relevant portion of the linear fit in this case is the y-intercept, which indicates an $R_{plexi/wax} = -0.3177$. Over the range of interest, the standard deviation from the average value is 0.0132. The negative sign indicates a 180° shift in phase between the two signals, a result of the ultrasonic wave traveling from a more elastic to a less elastic material.

Fibrous Wax Density Calculation

With the longitudinal velocity and plexi-wax reflection coefficient determined, the density of the wax can now be calculated. Using $c_{Lwax} = 1.6\ mm/\mu s$, $c_{Lplexi} = 2.67\ mm/\mu s$, $\rho_{plexi} = 1.18\ g/cm^3$, and $R_{plexi/wax} = -0.32$, the density of the wax as calculated from Eq. [3.3] is,

$$\boxed{\rho_{wax} = 1.0\ g/cm^3} \qquad [3.8]$$

Results for Bitumen Tape Coating

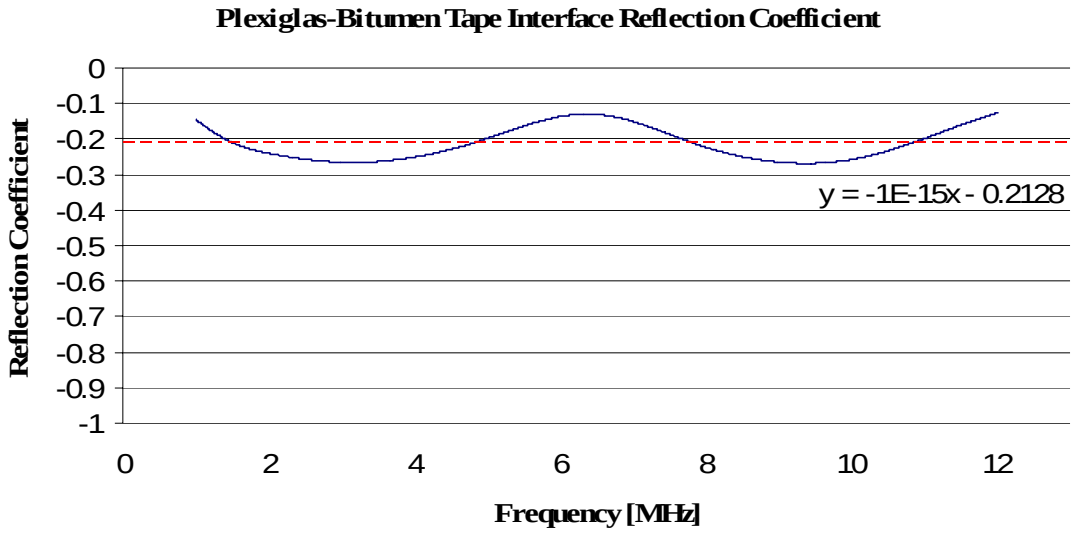

Figure 3.5 Measured reflection coefficient for a Plexiglas-Bitumen Tape interface. Blue line represents experimental data and red dotted line represents the average value of the data. A linear trend was fit to the average so as to see the y-intercept value. This equation is shown on the plot.

The average value of the reflection coefficient seen in Figure 3.5, having a standard deviation of 0.046, was used to calculate the density of the Bitumen Tape using Eq. [3.3],

$$\rho_{BT} = 1.2\ g/cm^3 \qquad [3.9]$$

To assess the accuracy of this technique, the measured density was compared to that of a sample of Bitumen Tape coating that was measured using gas pycnometry by Luo [2005]. Using this technique, the Bitumen Tape sample was found to have a density of 1.1073 g/cc with a standard deviation of 0.0001 g/cc. Comparing this value to that of Eq. [3.9], a 7% experimental error is seen. It has been shown by dispersion analysis in Section 6 that an error of this magnitude is acceptable.

4. Coating Attenuation Measurement Using Bulk Wave Ultrasound

Bulk wave attenuation properties of viscoelastic coatings are of interest as they are needed for analytic and numerical wave propagation calculations. Kline[1984] and Mak [1991] present several techniques that exist for these types of measurements. For field pipe evaluations, it will be necessary to perform in-situ material analyses as the material properties vary depending on manufacturer, age, and environment. Two methods for performing in-situ attenuation measurements are described in the following sections. The first technique is reserved for coatings with sufficient thickness as to resolve both a frontwall and backwall echo from the coating. The second section addresses coatings which are too thin to obtain separate echoes.

Attenuation Measurement for Thick Coatings

The term “thick”, as used here, refers to the ability to resolve front and backwall echoes from the coating. While this may be difficult for very thin coatings, like fusion bonded epoxies, it works well with field applied coatings such as bitumen and wax tapes. This is significant since these types of coatings often exhibit larger attenuation properties than factory applied coatings. A Fibrous Wax coating will be used here for the purpose of an example. Longitudinal wave input is used in for this example, although, the same technique applies to shear wave attenuation measurement. Consider the in-situ experimental setup illustrated in Figure 4.1.

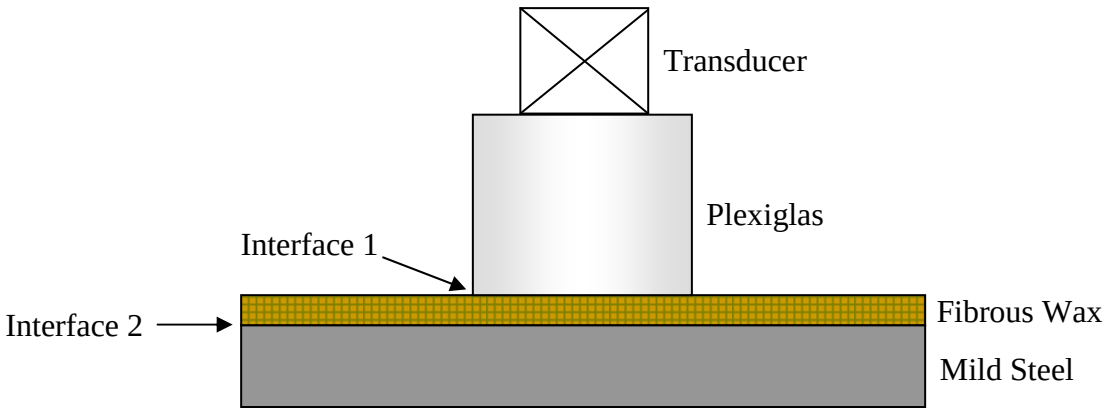

Figure 4.1 Experimental setup for the in-situ attenuation property measurement of viscoelastic coatings.

If the end of the Plexiglas delay line is left exposed to air (not in contact with coating) and a pulse is sent to the transducer, a reference signal can be obtained. This signal represents the amount of energy that is impinging upon the interface when the delay line is put into contact with the coating. It is described by,

$$p_0(t) = p_I(t) R_{plexi/air}\,, \qquad [4.1]$$

where $p_0(t)$ is the time series signal obtained when the delay line is exposed to air. If the plexi-air refelction coefficient, $R_{plexi/air}$, is assumed to be unity (with a 180° phase shift), then the time series signal obtained from the energy impinging upon the plexi-air interface, $p_I(t)$, is exactly equal to the reference signal with a 180° phase shift. Given this information, the energy transferred into the coating can be described by,

$$p_{T1}(t) = -p_0(t)(1 - R_{plexi/wax}). \quad [4.2]$$

The numerical subscript in Eq. [4.2] refers to the interface number labeled in Figure 4.1. This transmitted energy then propagates through the coating material and encounters the coating-steel interface. The reflected portion of the wave can be expressed as,

$$p_{R2}(t) = p_{T1}(t)R_{wax/steel}. \quad [4.3]$$

The reflection coefficient from the plexi-wax interface can be obtained by experiment and then used to calculate the wax density (see section on density measurement). This information, coupled with a velocity measurement, can be used to calculate the reflection coefficient for the wax-steel interface. Before returning to the transducer, the energy packet again encounters the first interface where a portion of the energy is reflected and the portion received by the transducer is described by,

$$p_{rec}(t) = p_{R2}(t)(1 - R_{wax/plexi}) = p_{R2}(t)(1 + R_{plexi/wax}). \quad [4.4]$$

Equaitons [4.1] – [4.4] can be combined to express the reference signal in terms of the final received signal,

$$p_{rec}(t) = p_0(t)R_{wax/steel}(R^2_{plexi/wax} - 1). \quad [4.5]$$

Equation [4.5] accounts for all the energy lost from reflection and transmission phenomena but not for energy lost due to material attenuation. Therefore, Eq. [4.5] is acceptable for perfectly elastic materials but must be modified to account for signal attenuation introduced during propagation through the viscous wax coating. Assuming the Plexiglas delay and steel are lossless, the received signal, including attenuation introduced by the wax coating, can be expressed as follows,

$$p_{rec}(t) = e^{-\alpha 2L}p_0(t)R_{wax/steel}(R^2_{plexi/wax} - 1), \quad [4.6]$$

where L is the coating thickness and α is the attenuation coefficient. To analyze the frequency dependence of the attenuation coefficient it is useful to work in the frequency domain and therefore the Fourier Transform of the time series signals is used in place of the time series. The transforms are described in Eqs. [4.7] and [4.8] on the next page.

$$P_{rec}(f) = \int_{-\infty}^{\infty} p_F(t)e^{-j2\pi t}dt \quad [4.7]$$

$$P_0(f) = \int_{-\infty}^{\infty} p_0(t) e^{-j2\pi t} dt \qquad [4.8]$$

Making the transformation to the frequency domain and rearranging Eq. [4.6], the attenuation is found to be,

$$\alpha(f) = -\frac{1}{2L} \ln\left(\frac{P_{rec}(f)}{P_0(t)} \frac{1}{R_{wax/steel}(R^2_{plexi/wax} - 1)} \right), \qquad [4.9]$$

where,

$$R_{plexi/wax} = -\frac{P_{R1}(t)}{P_0(t)}. \qquad [4.10]$$

More information regarding the calculation of Eq. [4.10] may be found in Section 2, regarding density measurement. Figure 4.2 shows the frequency spectrums of the three signals required to calculate the attenuation coefficient.

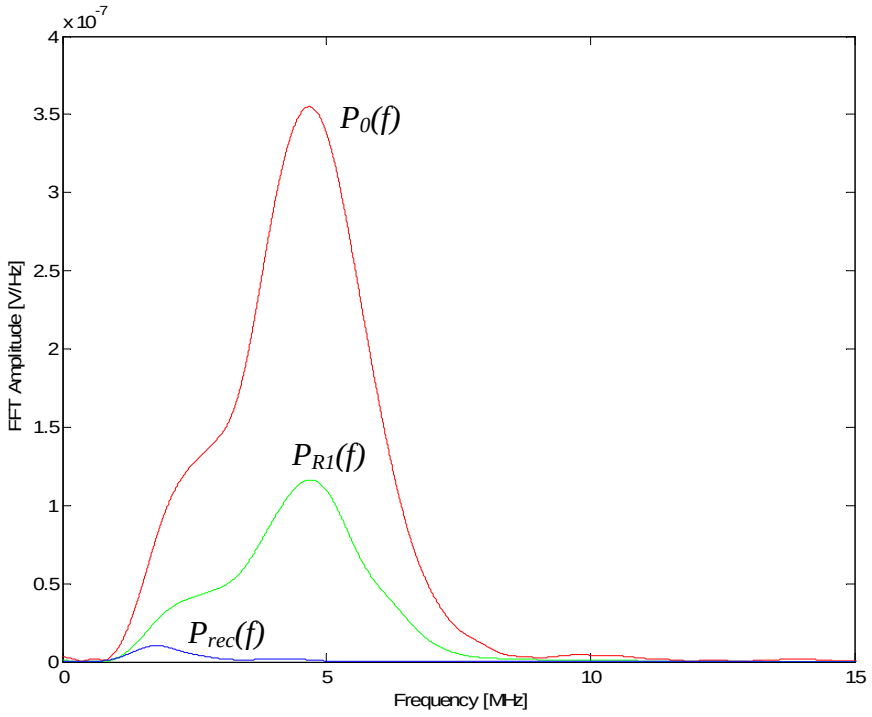

Figure 4.2 Frequency spectrums of signals required for the calculation of attenuation. The red line represents the FFT of the time series reflected from a plexi-air interface. The green line represents the FFT of the time series reflected from the plexi-wax interface. The blue line represents the FFT of the time series reflected from the wax-steel interface.

The reflection coefficient calculated using the transformed signals and Eq. [4.10] is shown in Figure 4.3. Figure 4.4 is a plot of the attenuation coefficient, as per Eq. [4.9], showing a nearly-linear trend with frequency. The slope of the linear fit is the longitudinal attenuation constant used for theoretical and numerical modeling.

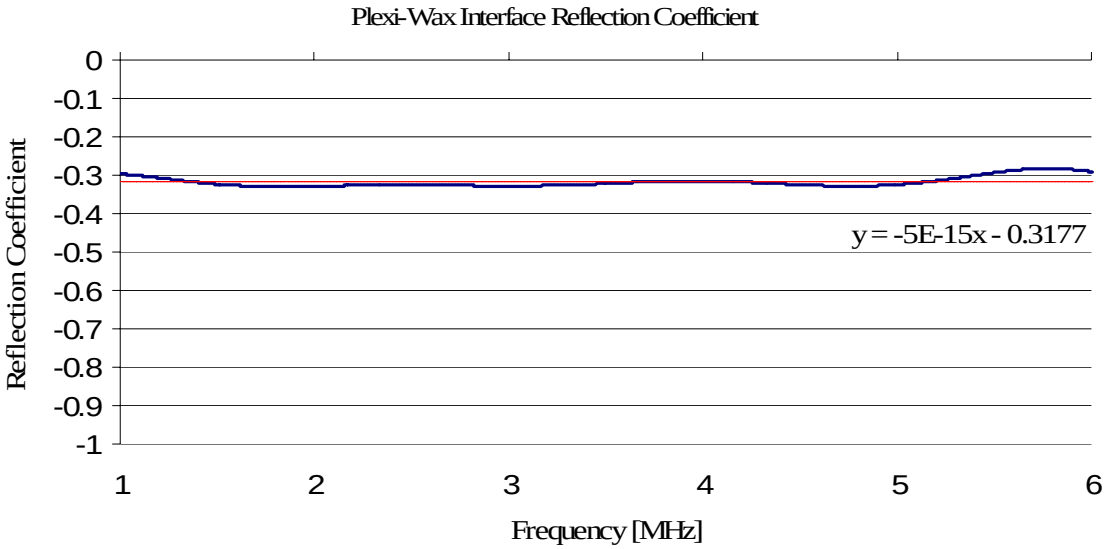

Figure 4.3 Experimentally measured reflection coefficient for a Plexiglas/Fibrous-Wax interface. The blue line represents the experimental data. The red dotted line represents the average value over the range of interest. More information on this measurement may be found in the section concerning density measurement.

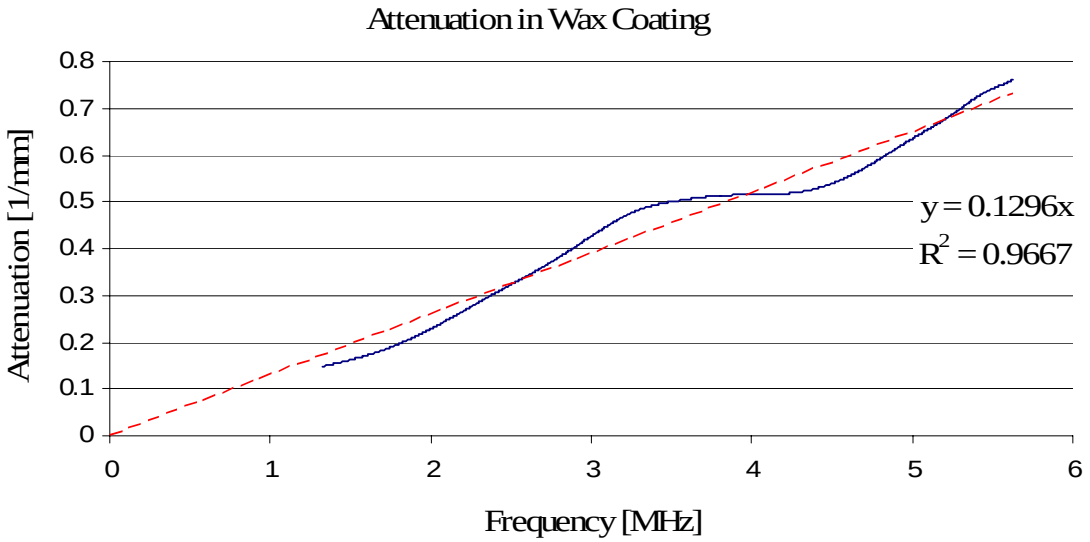

Figure 4.4 Experimentally determined attenuation trend in a fibrous wax coating. The blue line represents the experimental data. The red dotted-line represents a linear fit to the experimental data. The slope of the linear fit is the longitudinal attenuation constant used for theoretical and numerical modeling.

The same technique described on the previous pages was used to measure the longitudinal wave attenuation in a bitumen-tape coating. The measurement in this case wave performed with a highly-damped, broadband 10MHz transducer. The results are shown in Figure 4.5.

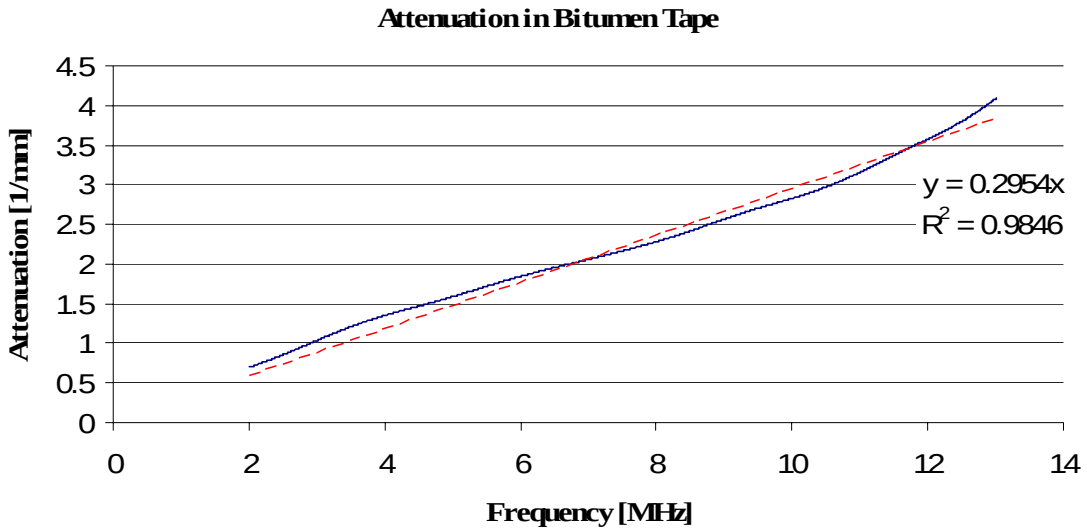

Figure 4.5 Experimentally determined attenuation trend in a bitumen-tape coating. The blue line represents the experimental data. The red dotted-line represents a linear fit to the experimental data. The slope of the linear fit is the longitudinal attenuation constant used for theoretical and numerical modeling.

Attenuation Measurement for Thin Coatings

For very thin coatings, it may not be possible to discern the back-wall echo of the coating and the front-wall echo of the coating. In this event, the technique described for thick coatings may not be applicable and a different technique is needed. For such occurrences, there are two applicable techniques. The first technique involves an approximation using the back-wall echo of the steel pipe and the second technique utilizes a Normalized Amplitude Spectrum (NAS) and was developed by Guo et al [1995] based on work by Haines et al [1978].

The first attenuation measurement technique for thin coatings produces an approximate measurement. The process is the same as that for the attenuation measurement of thick coatings but instead of using the back-wall echo of the coating, the back-wall echo of the steel pipe is used. The reason this solution is approximate is because it does not account for the reflection of energy at the coating-pipe interface. Through intelligent data acquisition, it is possible to reduce this error to a negligible level. First, a lower frequency transducer should be selected for the measurement. In general, the wavelength should be several times larger than the coating thickness. Examination of the RF waveform should show little or no sign of coating reflections. The attenuation caused by the steel, which is

obtained by a separate measurement, is then subtracted from the attenuation of the coating-steel system. A sample result for B300M coating can be seen in Figs. 4.6 and 4.7.

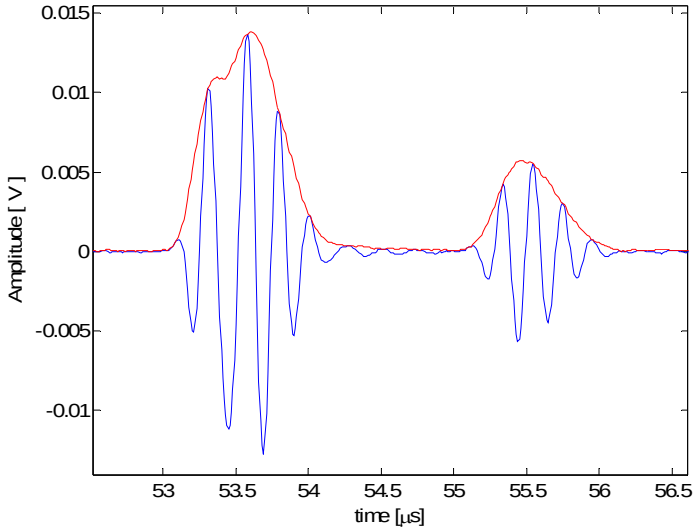

Figure 4.6 RF waveform showing the front-wall echo from the coating and the back-wall echo from the steel pipe. The red line is the analytic envelope of the waveform.

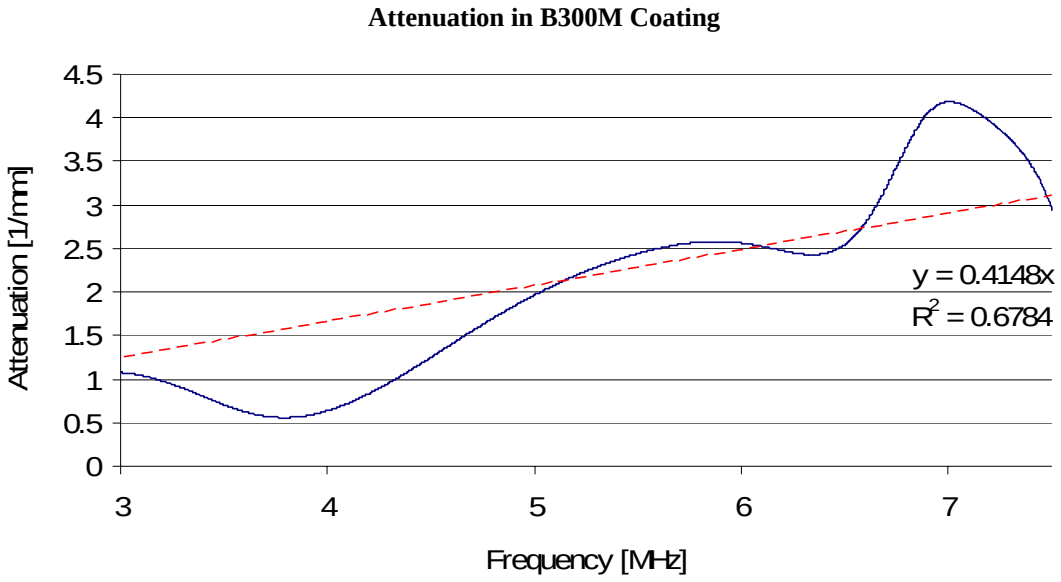

Figure 4.7 Attenuation plot for B300M coating using the pipe back-wall approximation.

The results in Figure 4.7 show more variation with frequency than those of Figures 4.4 and 4.5. This is due to the reflection from the coating-steel interface which was neglected in the calculation but can be seen slightly in the analytic envelope of the first wave packet in Figure 4.6. The data in Figure 4.7 is then corrected by removing the attenuation caused by the steel itself. Figure 4.8 is a plot of the attenuation caused by the steel.

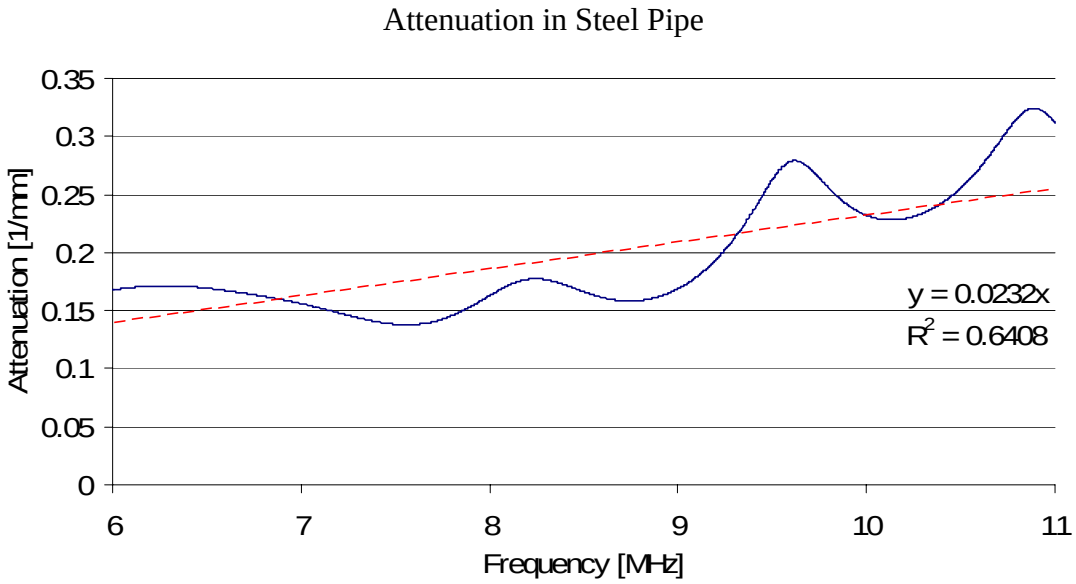

Figure 4.8 Bulk-wave attenuation plot for a steel pipe with no coating.

The NAS is another echo technique, developed by Guo et al [1995], and provides further means of attenuation measurement for thin coatings. The NAS, or Normalized Amplitude Spectrum, is the FFT of the echo-train created by the coating reflections normalized by the FFT of the front wall echo. The idea behind this technique is that the FFT of the echo-train will have equally spaced recessions corresponding to the repetition rate of the coating echoes. Figure 4.9 shows the FFT results for the front-wall echo and echo-train in 1LFBE coating. Figure 4.10, the NAS, is the result of normalizing the echo-train FFT by the front-wall echo FFT. In the notation of Guo, the peaks and corresponding frequencies of the NAS can be used to calculate the attenuation using,

$$A_\alpha^2 = \frac{|R_{ca}|(S_{\max} - 1)}{|R_{ba}|(1 - R_{ca}^2 S_{\max})}, \qquad [4.11]$$

and,

$$\alpha = -\frac{1}{2L}\ln(A_\alpha^2). \qquad [4.12]$$

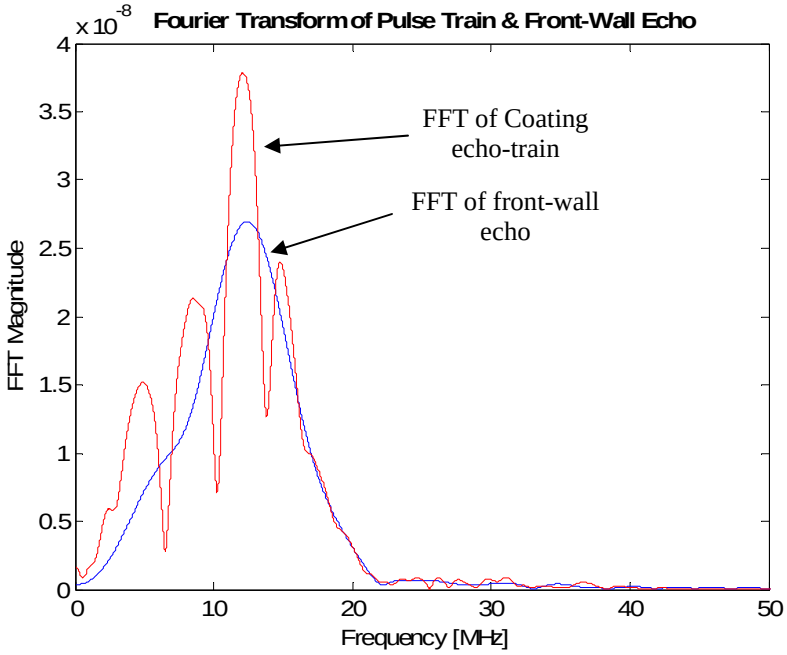

Figure 4.9 Fourier transforms of the front-wall echo (blue) and the coating echo-train (red) for 1LFBE. The recessions in the echo-train FFT correspond to the repetition rate of the echoes.

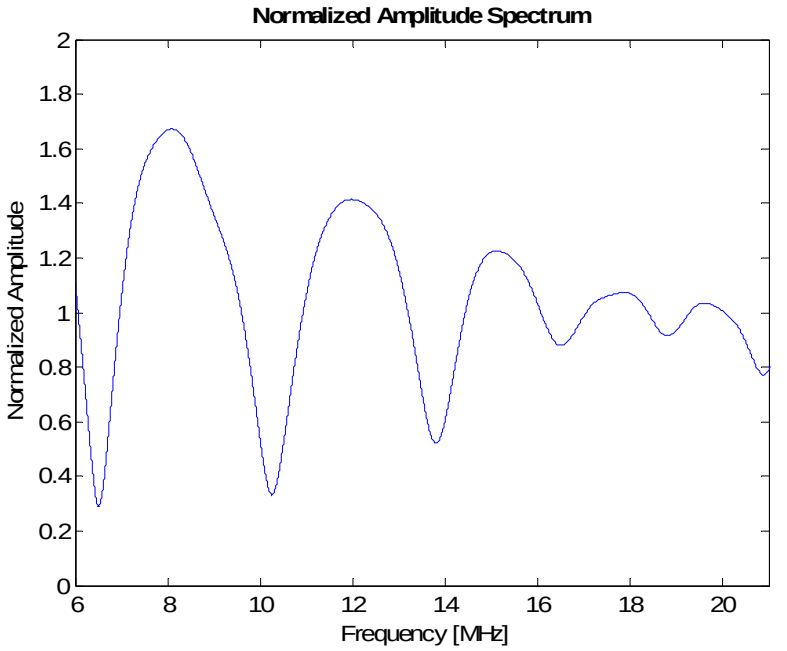

Figure 4.10 Normalized Amplitude Spectrum (NAS) for 1LFBE coating. The peaks of the NAS are used for the attenuation calculation.

Figure 4.11 shows the attenuation results obtained using the data from Figure 4.10 and Equations [4.11] and [4.12]. The attenuation trend appears to be parabolic in frequency and therefore a linear fit to all data points would over-estimate the attenuation for low frequencies. For this reason, a linear fit (green line) was used for the frequency range of interest. In general, using a linear fit to all the data points would not produce a significant amount of error.

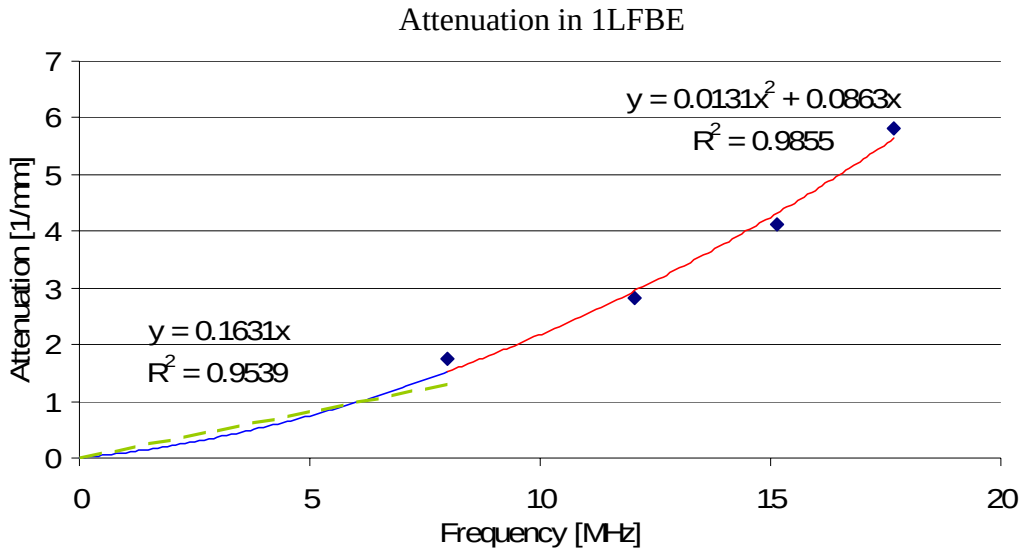

Figure 4.11 Attenuation plot for 1LFBE obtained using NAS technique. Blue diamonds represent data points taken from the NAS. The blue-red compound line represents a parabolic fit to the data points. The green dotted line represents a linear fit to the frequency region of interest.

Results

Table 4.1 contains the measured properties for all of the coatings. All shear properties listed were generated using the using the approximations that were developed in the section regarding the study of the theoretical phase velocity and attenuation dispersion curves. Based on a Poisson Ratio study, the shear wave velocity was assumed to be 0.45 time the longitudinal wave velocity. Based on available data and theoretical dispersion studies, the shear wave attenuation for epoxy-based coatings was assumed to be 5 times the longitudinal attenuation and 10 times the longitudinal attenuation for bituminous-type coatings. As an example, the shear wave velocity for B50 coating is known to be 0.75 mm/us. If approximated using the discussed guidelines, the predicted value would be 0.86 mm/us. As shown in the dispersion study, such as small error is irrelevant to the theoretical dispersion calculations.

Coating	t (mm)	ρ (g/cc)	C_L (mm/us)	C_S (mm/us)	α_L/ω (1/mm)	α_S/ω (1/mm)
2LFBE	1.5	0.4	3.0	1.35	0.021	0.105
B50	0.27	1.2	1.9	0.75	0.052	0.52
1LFBE	0.23	0.8	1.9	0.86	0.026	0.13
BT	0.74	1.2	1.9	0.86	0.047	0.47
B300M	0.2	0.6	1.5	0.68	0.062	0.31
EP	0.13	1.0	1.68	0.77	0.048	0.48
WT	2.4	1.0	1.6	0.72	0.021	0.21

Table 4.1 Coating properties as determined using ultrasonic wave analysis and theoretically based approximation.

5. Proof-of-Concept

It has yet to be proven that the measured coating properties produce reasonable guided-wave attenuation predictions. With this goal, an experiment was designed in which data was collected for a sufficient amount of time so as to obtain multiple backwall-echoes from the 10 ft. coated specimens. The echo peaks where then extracted and fit with an exponential curve. The first torsional mode, T(0,1), was used for this experiment as it is slightly more attenuative than the second longitudinal mode, L(0,2), at low frequencies. This increased attenuation was needed to produce as much separation between coating attenuation trends as possible, within in the low-frequency operating range of the guided-wave instrument. Tests were performed at 40kHz. An example data set can be seen in Figure 5.1, showing the analytic envelope of the RF waveform, the peak data, and the normalized exponential trendline.

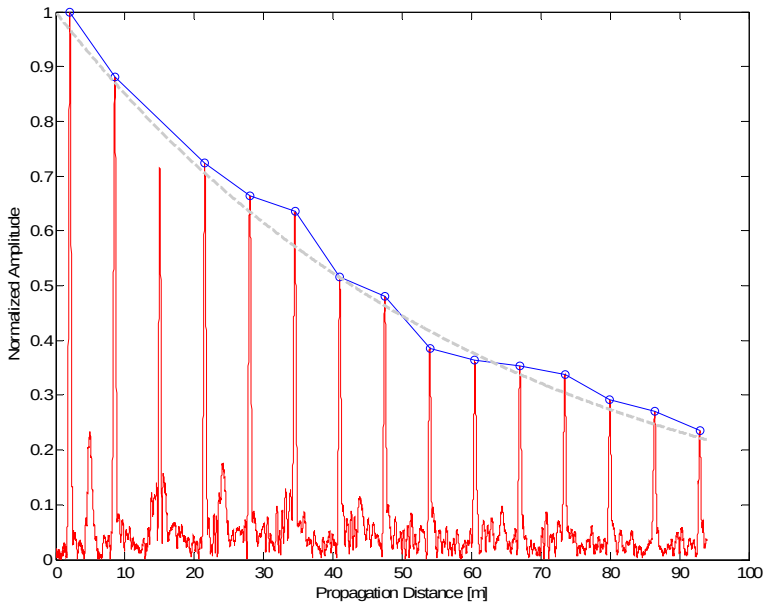

Figure 5.1 Analytic envelope (red) of RF waveform obtained using the T(0,1) mode at 40kHz showing attenuation over distance. The blue line connects to peak data which are represented by the blue circles. The gray dotted-line is the normalized exponential trend fit to the peak data. Results shown are for the 10ft. pipe specimen with 1LFE coating.

The attenuation trends for a bare pipe specimen and all coated specimens were calculated and can be seen in Figure 5.2 on the following page. Of the coating specimens, the wax tape coating and the bitumen tape coating were particularly attenuative with the dual-layer fusion bonded epoxy also being noticeably more attenuative than the other coatings. Figure 3 shows the predicted guided-wave attenuation dispersion curves for the T(0,1) mode in the pipe specimens with different coatings. The results in Figure 5.3 are a prediction based on the measured material properties of the coatings. Figure 5.4 is the same as Figure 5.3 but with an expanded y-axis.

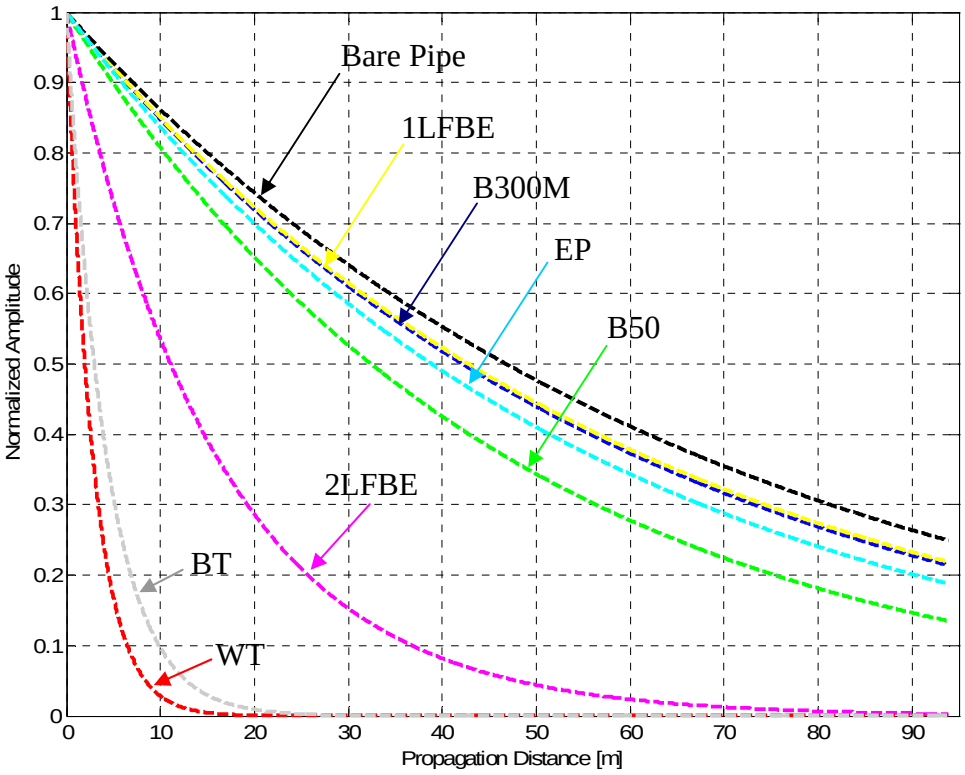

Figure 5.2 Genuine guided wave attenuation trends in coated pipe specimens as obtained by experimental investigation. Trends were obtained using T(0,1) mode excited at 40kHz. These trends represent actual measured guided-wave attenuation rates and are not based on any prediction made using bulk wave measurements.

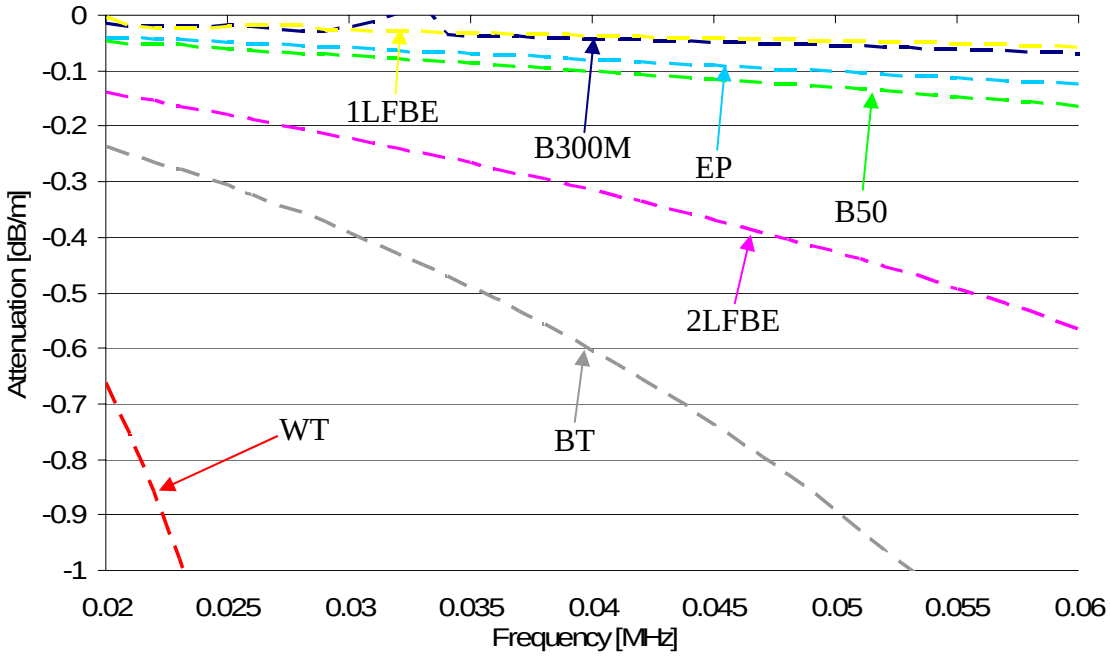

Figure 5.3 Predicted guided-wave attenuation results for the T(0,1) mode at 40kHz, based on bulk-wave measurements.

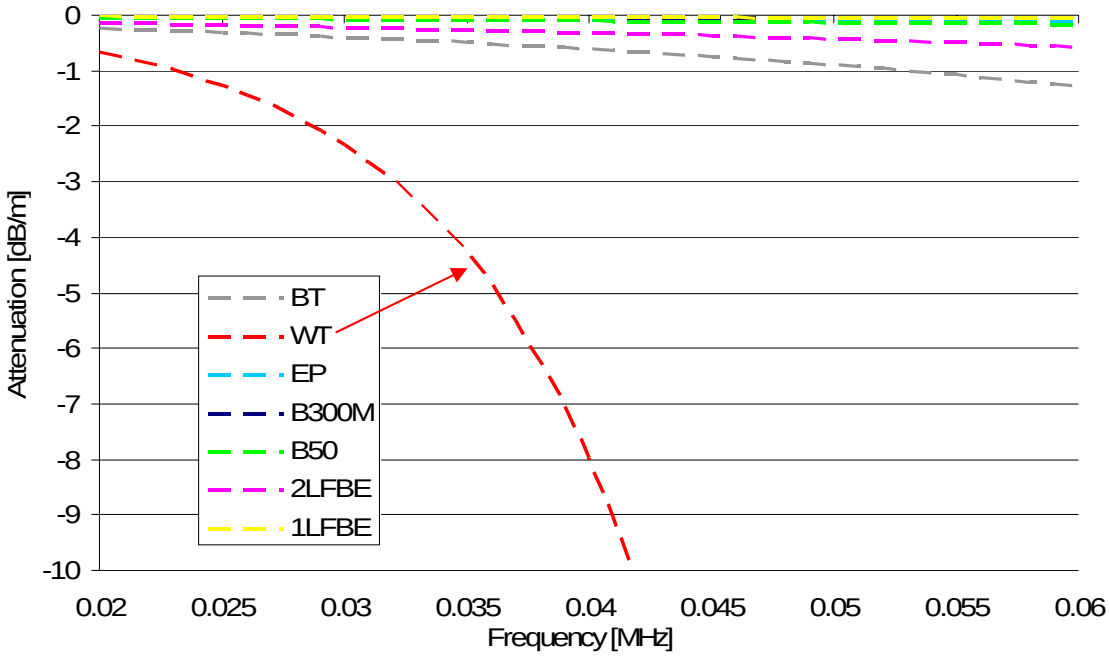

Figure 5.4 Figure 5.3 with an expanded y-axis to better see the attenuation trend of the pipe specimen with wax tape (WT) coating.

Predicted Attenuation vs. Actual Attenuation

	Rank	Predicted	Actual
Least Attenuative	1	Bare	Bare
	2	1LFBE	1LFBE
	3	B300M	B300M
	4	EP	EP
	5	B50	B50
	6	2LFBE	2LFBE
	7	BT	BT
Most Attenuative	8	WT	WT

Table 5.1 Comparison of predicted attenuation results and actual attenuation results showing 100% agreement for the given thicknesses and types of coatings. The predictions, based on bulk wave measurements, correctly ranked the specimens according to attenuation of guided waves. This is a key result demonstrating the ability to correctly predict the coating effects on guided-wave propagation.

Discussion

It can be seen from Figures 5.2 and 5.3, and Table 5.1 that the actual experimental results and the theoretical results, based on the measured coating material properties, agree very well. In the case of the enamel paint (EP) coating, the theoretical results correctly predicted that there would be more attenuation than the 1LFBE and B300M coatings. This was against human intuition as the enamel paint coating was the thinnest of all coatings and was not expected to produce any noticeable attenuation. This is a key example and demonstration of the usefulness of an in-situ coating evaluation instrument.

The attenuation values seen in Figures 5.3 and 5.4 were generated under the assumption of lossless propagation in a bare pipe. If an attenuation curve was drawn for a bare pipe, it would appear in these figures as a line at zero attenuation for all frequencies. From Figure 2 it can be seen that guided-wave propagation in a bare pipe is not actually lossless. Energy is lost to material absorption and geometrical diffraction. An overall guided-wave attenuation factor can be obtained by adding the attenuation due to viscoelastic coating and the attenuation due solely to the pipe material. As the study of energy loss in a bare pipe is not of immediate interest, it will be held for later consideration.

6. Theoretical Dispersion Study

Theoretical dispersion curves are an invaluable tool for the analysis of guided wave propagation in pipe. A parametric study of the attenuation and phase velocity dispersion curves for coated pipe is presented here using a dispersion code developed by Barshinger [2002] and modified by Luo [2005]. Variations in density, coating thickness, shear and longitudinal velocities, and shear and longitudinal attenuation constants are examined. The goal of this study is to determine which of the material properties have the most significant effect on the phase velocity and attenuation dispersion curves. This will give an indication of the accuracy with which these properties must be measured.

To perform the parametric study, B50 was chosen as a representative coating. The values shown in Table 6.1 represent the actual properties of this coating. These base values were varied, where the effects of the variations can be seen in Figures 6.2 through 6.10.

Parameter	Actual Value
Pipe Inner Radius	50.8 (mm)
Pipe Outer Radius	56.35 (mm)
Coating Thickness	0.4 (mm)
Long. Velocity (steel)	5.92 (mm/us)
Shear Velocity (steel)	3.23 (mm/us)
Long. Att. (steel)	0 (1/mm)
Shear Att. (steel)	0 (1/mm)
Long. Velocity (B50)	1.86 (mm/us)
Shear Velocity (B50)	0.75 (mm/us)
Long. Att. (B50)	0.023 (1/mm)
Shear Att. (B50)	0.24 (1/mm)
Density (steel)	7.8 (g/cc)
Density (B50)	1.5 (g/cc)

Table 6.1. Unaltered parameters for the coated pipe used for theoretical dispersion studies with dispersion code developed by Barshinger [2001] and modified by Luo [2005].

Variation in Density

To examine the effects of coating density on the dispersion curves, density was varied independently of all other parameters. Figures 6.2 and 6.3 show the results for three different density values: the actual density, the halved density, and the doubled density. Figure 6.2 shows the phase velocity results for the first two longitudinal modes and the first torsional mode. Figure 6.3 shows the attenuation results for the same modes.

Variation in Coating Thickness

Coating thickness was varied independently of the other parameters. Because the actual coating is relatively thin, only larger thicknesses were examined. Results can be seen for the actual thickness, double the actual thickness, and triple the actual thickness. Figure 6.4 shows the phase velocity results for the first two longitudinal modes and the first torsional mode. Figure 6.5 shows the attenuation results for the same modes. Figure 6.6 is the same plot as Figure 6.5 but with an expanded y-axis. By expanding the y-axis the attenuation behavior at higher frequencies can be seen.

Variation in Wave Velocity

Rather than varying the longitudinal and shear wave velocities independently, the ratio of shear wave velocity to longitudinal wave velocity was varied. This was done because of the innate relationship between these two parameters. As illustrated by Eq. [6.1] for elastic materials, the shear wave velocity is a function of Poisson's ratio and longitudinal velocity.

$$c_T^2 = \frac{c_L^2(1-2\nu)}{2(1-\nu)}. \qquad [6.1]$$

Therefore, if the longitudinal wave velocity is known, the relationship between Poisson's ratio and the shear-wave to longitudinal-wave velocity-ratio can be plotted, as seen in Figure 6.1 for a longitudinal velocity equal to that of the B50 coating.

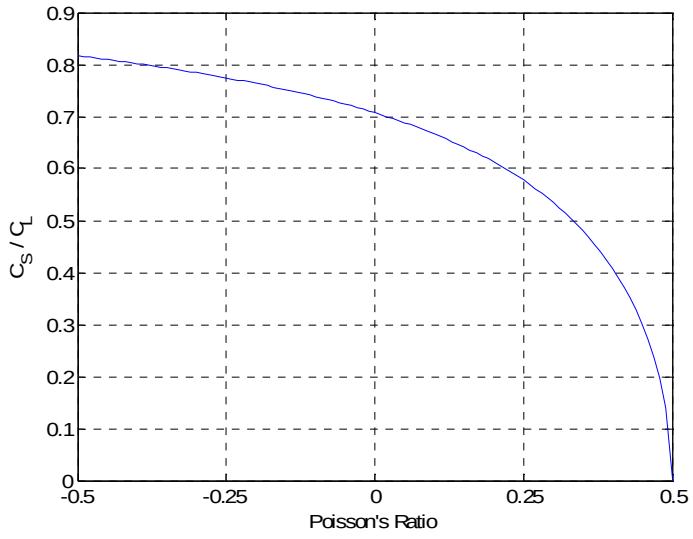

Figure 6.1 Relationship between Poisson's ratio and shear wave to longitudinal wave velocity-ratio for a longitudinal velocity equal to that of B50 coating (c_L=1.86 mm/us).

Materials which exhibit a negative Poisson ratio are called Auxetic materials and are typically specially-crafted polymers that are not of interest in this study. Therefore, the area of interest, in Figure 6.1, is from $\nu = 0$ to $\nu = 0.5$. The important information to gather from Figure 6.1 is that the shear wave velocity never exceeds the longitudinal wave velocity and that the ratio of shear wave velocity to longitudinal wave velocity decreases parabolically with increasing Poisson ratio. Additionally, a theoretical cap for the velocity ratio can be obtained from this plot. For the B50 coating, this ratio-cap is at approximately 0.7.

Based on this information, Figures 6.7 and 6.8 were generated for the actual velocity-ratio, the common velocity-ratio approximation of 0.6, and a smaller approximation of 0.25. Figure 6.7 shows the phase velocity results for the first two longitudinal modes and the first torsional mode. Figure 6.8 shows the attenuation results for the same modes.

Attenuation Constant Variation

The final parameters studied were the shear and longitudinal attenuation constants. Again, these two variables were varied dependently. Due to the viscous nature of viscoelastic materials, shear waves attenuate more rapidly than longitudinal waves. A review of published properties of viscoelastic materials, Barshinger [2001] and Luo [2005], has shown that shear wave attenuation is typically multiple times larger than the longitudinal wave attenuation. Therefore, the shear wave attenuation constant was varied as a multiple of the longitudinal wave attenuation. Figures 6.9 and 6.10 were generated for the actual attenuation constant relationship, a shear attenuation constant twice the magnitude of the longitudinal, and a shear attenuation constant ten times the magnitude of the longitudinal attenuation constant. Figure 6.9 shows the phase velocity results for the first two longitudinal modes and the first torsional mode. Figure 6.10 shows the attenuation results for the same modes.

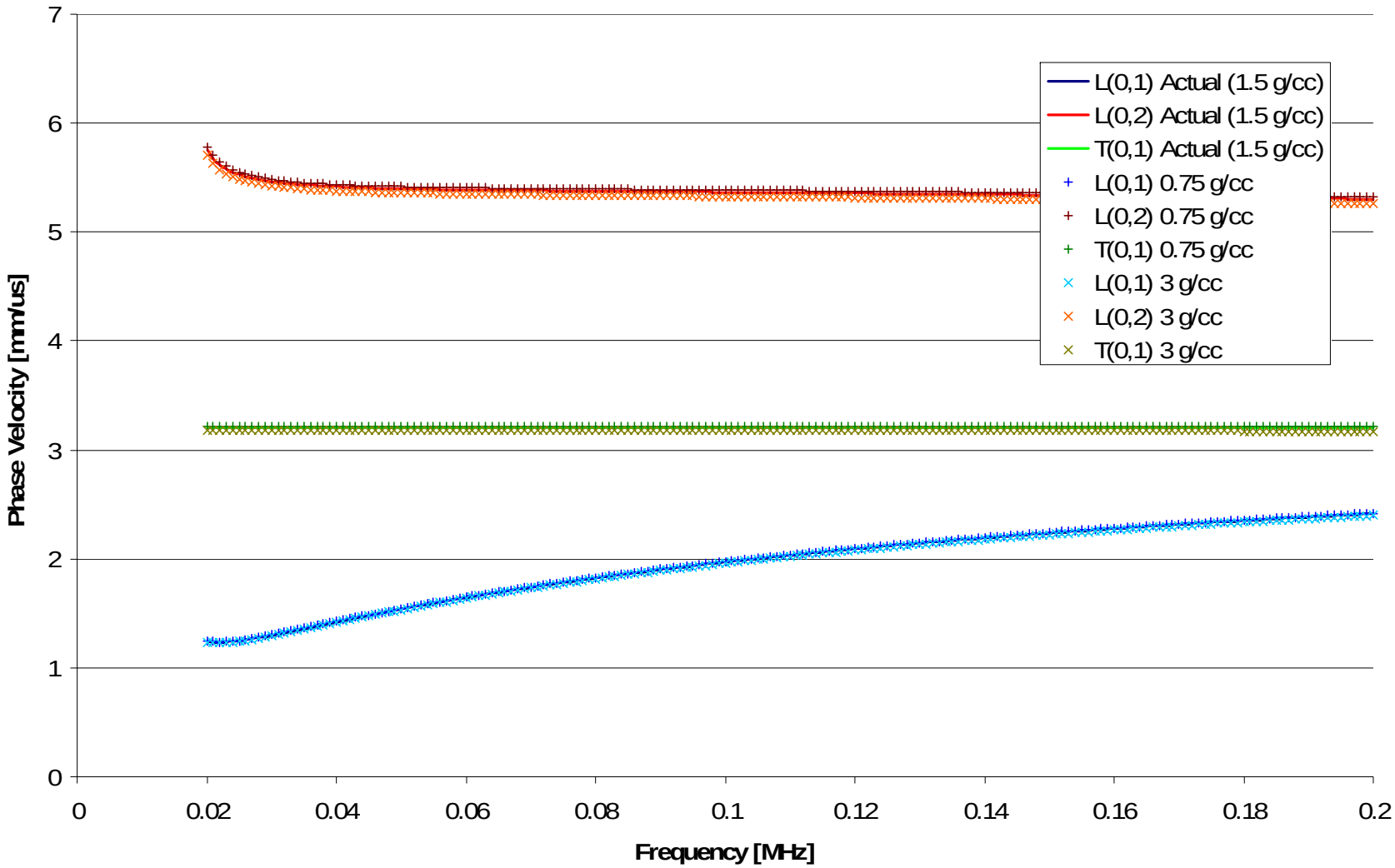

Figure 6.2 Phase velocity dispersion curve for a pipe with B50 coating. Results are shown for the actual coating density, half actual-density, and double actual-density. The results show that variation in density has very little effect on phase velocity. A very small difference can be seen in the L(0,2) and T(0,1) modes for double the actual density. This suggests that errors in density measurement, as large as 100%, will have only a minor effect on phase velocity.

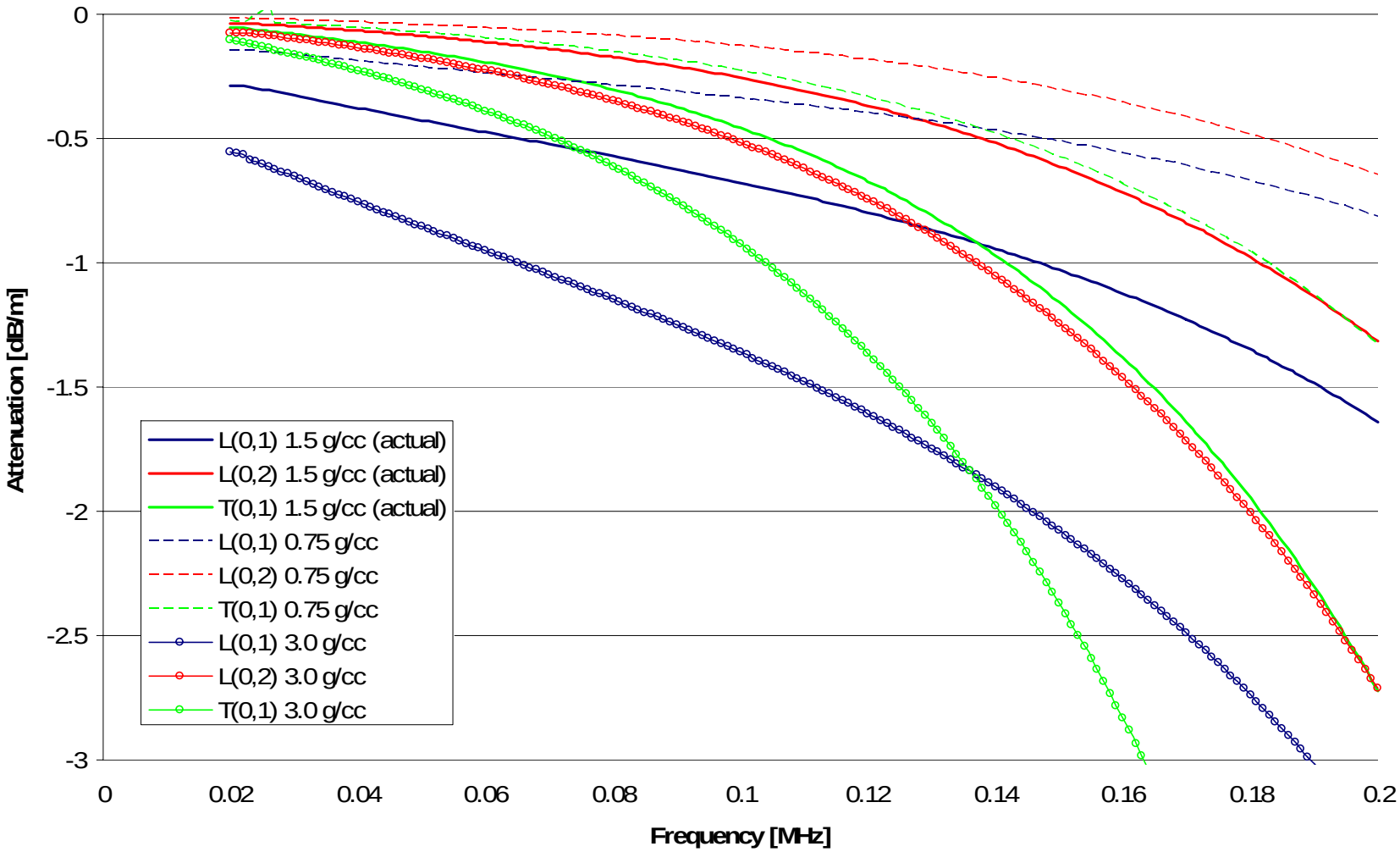

Figure 6.3 Attenuation dispersion curve for a pipe with B50 coating, illustrating the effect of variation in coating density. Results are shown for the actual coating density, half actual-density, and double actual-density. Results show that variations in density produce significant changes in the attenuation dispersion curves. For the L(0,2) and T(0,1) modes, the variation is relatively small at low frequencies with differences increasing with frequency. The L(0,1) modes appears to be sensitive to density changes even at low frequencies.

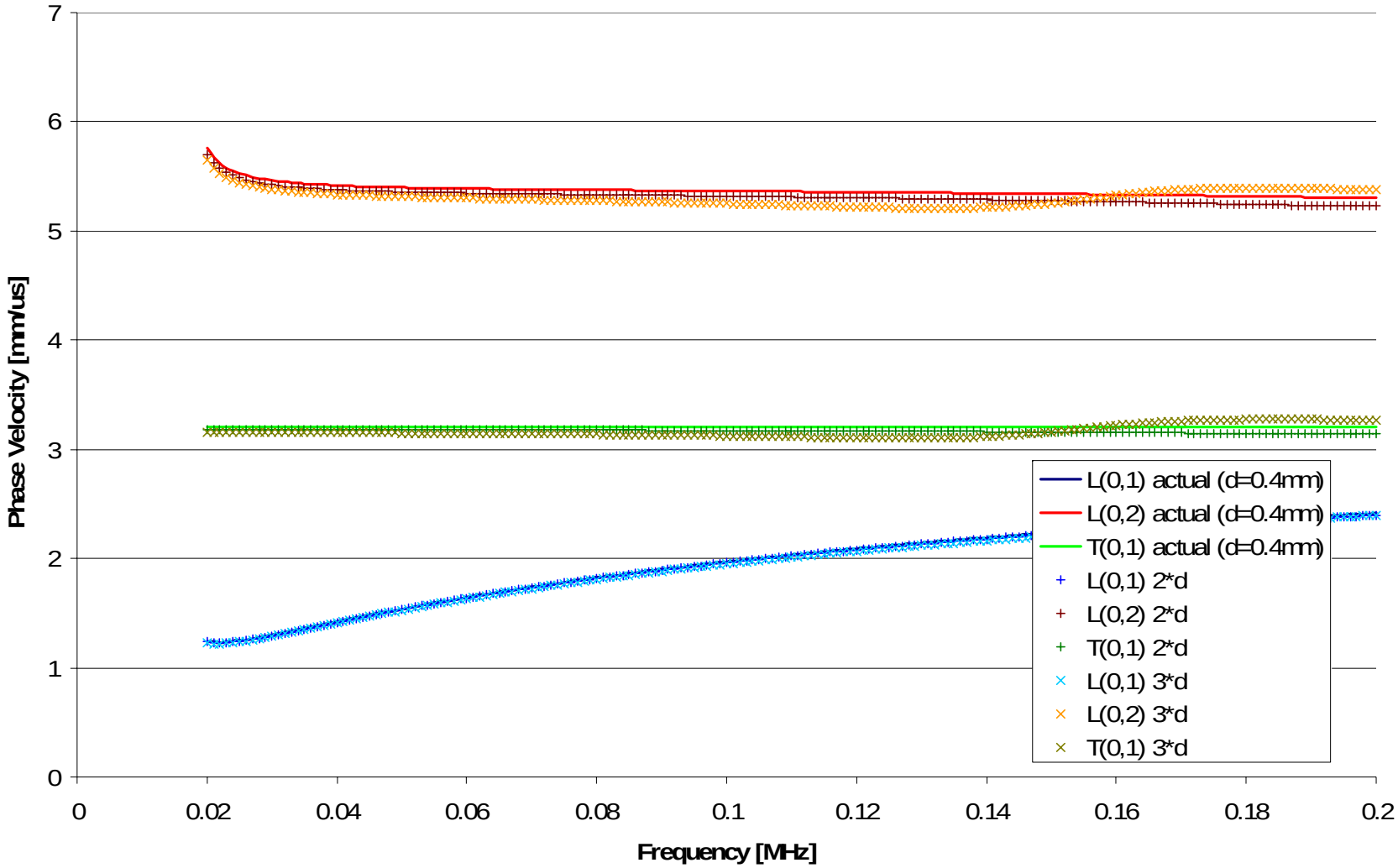

Figure 6.4 Phase velocity dispersion curve for a pipe with B50 coating, illustrating the effect of variation in coating thickness. Results are shown for the actual coating thickness, double actual-thickness, and triple actual-thickness. Results show that coating thickness has a noticeable effect on the L(0,2) and T(0,1) phase velocity dispersion curves, while the L(0,1) mode is unaffected. Though the variations in the curves are relatively small, they are noticeable and increase with frequency.

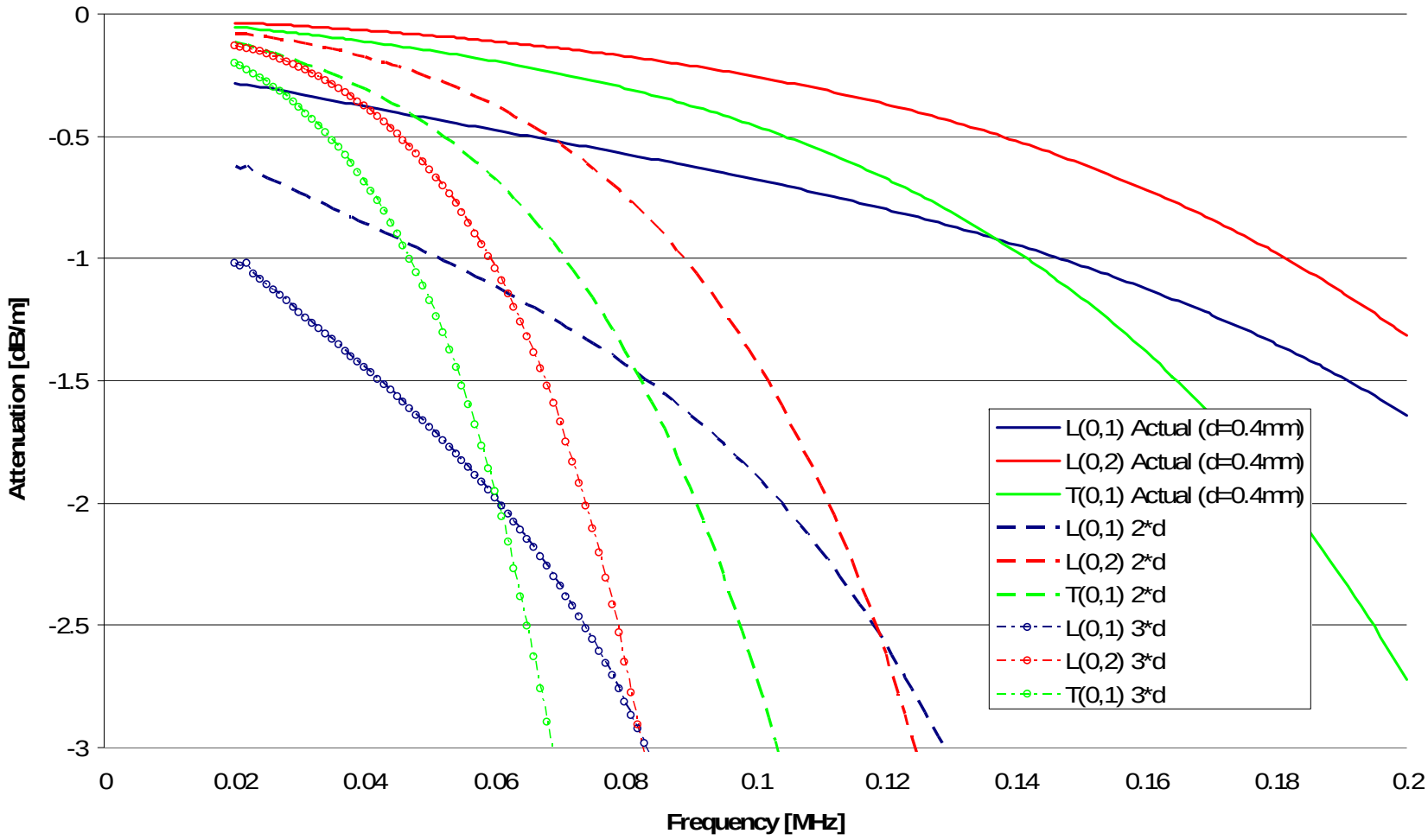

Figure 6.5 Attenuation dispersion curve for a pipe with B50 coating, illustrating the effect of variation in coating thickness. Results are shown for the actual coating thickness, double actual-thickness, and triple actual-thickness. Results show significant changes in the dispersion curves for different coating thicknesses. Variations for the L(0,2) and T(0,1) mode are relatively small at low frequencies and increase dramatically with frequency. The L(0,1) mode is very sensitive to coating thickness, even at low frequencies. This indicates that accurate measurement of coating thickness is critical.

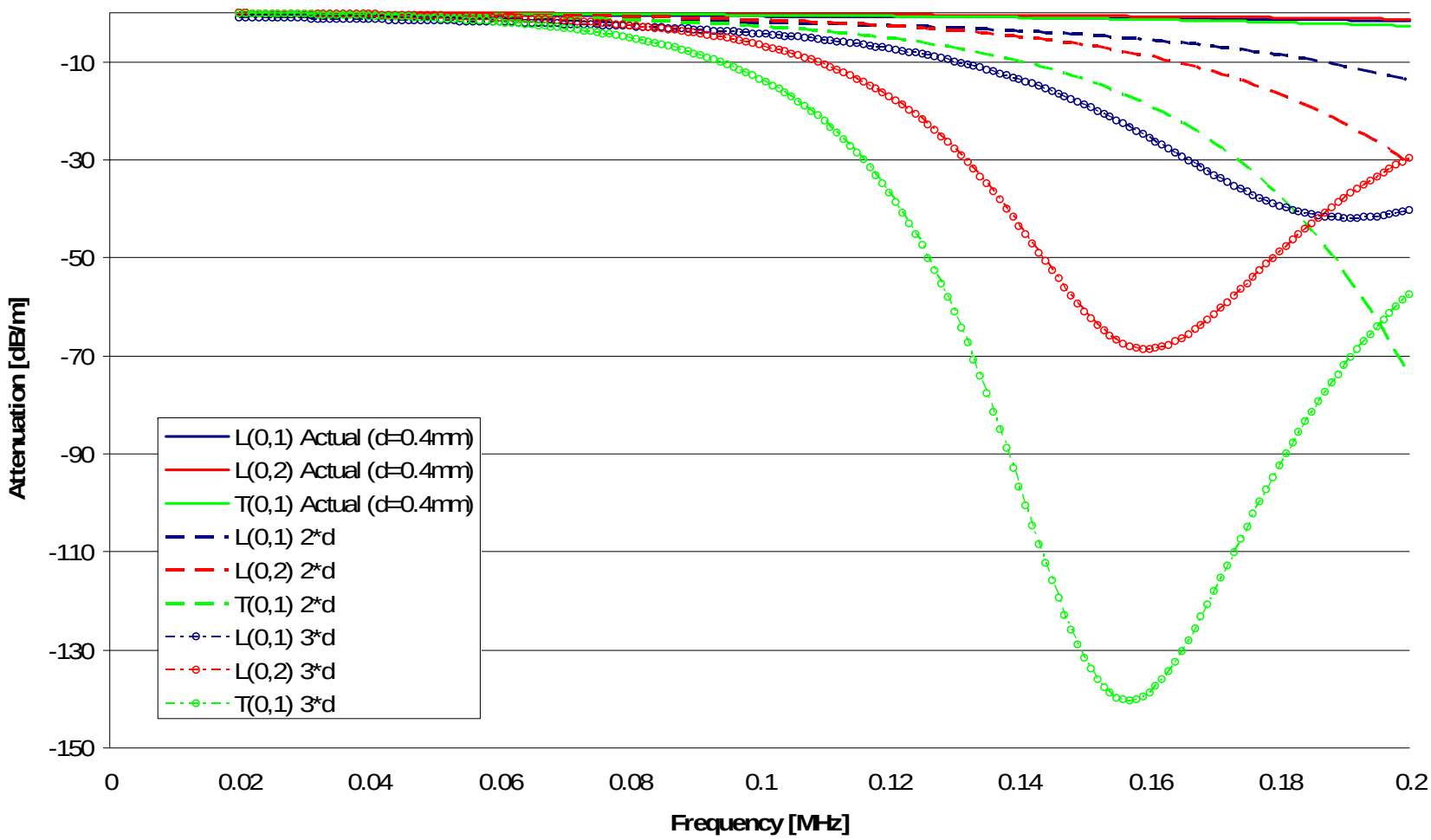

Figure 6.6 Figure 6.5 with an expanded y-axis to better see the attenuation trends at higher frequencies. Results show regions where attenuation reaches a maximum and then begins to decrease again. This is very useful information for high-frequency guided-wave inspection.

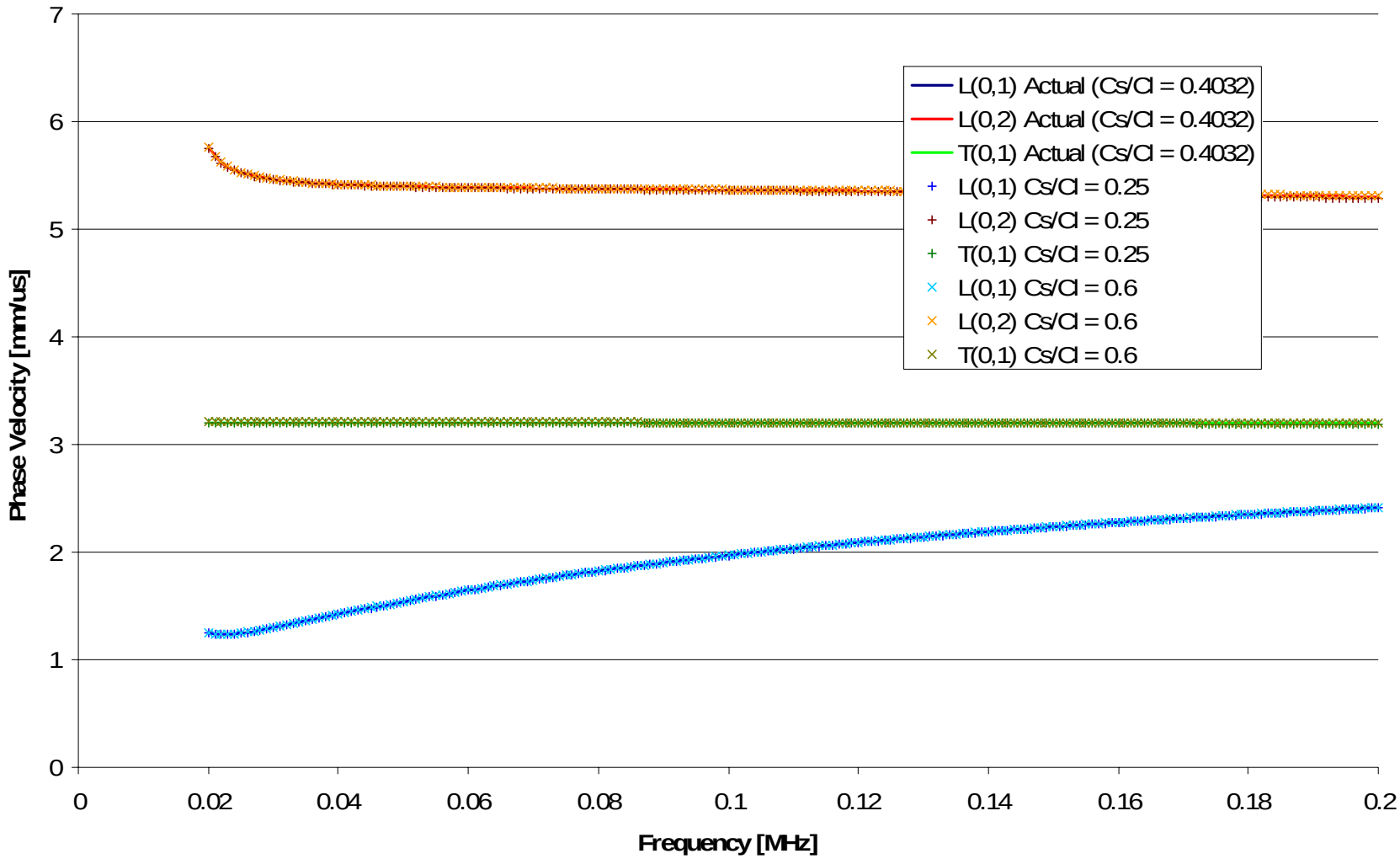

Figure 6.7 Phase velocity dispersion curve for a pipe with B50 coating, illustrating the effect of variation in wave velocity. Results are shown for the ratio of shear velocity to longitudinal velocity. The actual ratio is plotted along with the common shear wave velocity approximation of $0.6C_L$ and a smaller approximation of $0.25C_L$. Results show virtually no change in phase velocity for any of the velocity ratios plotted.

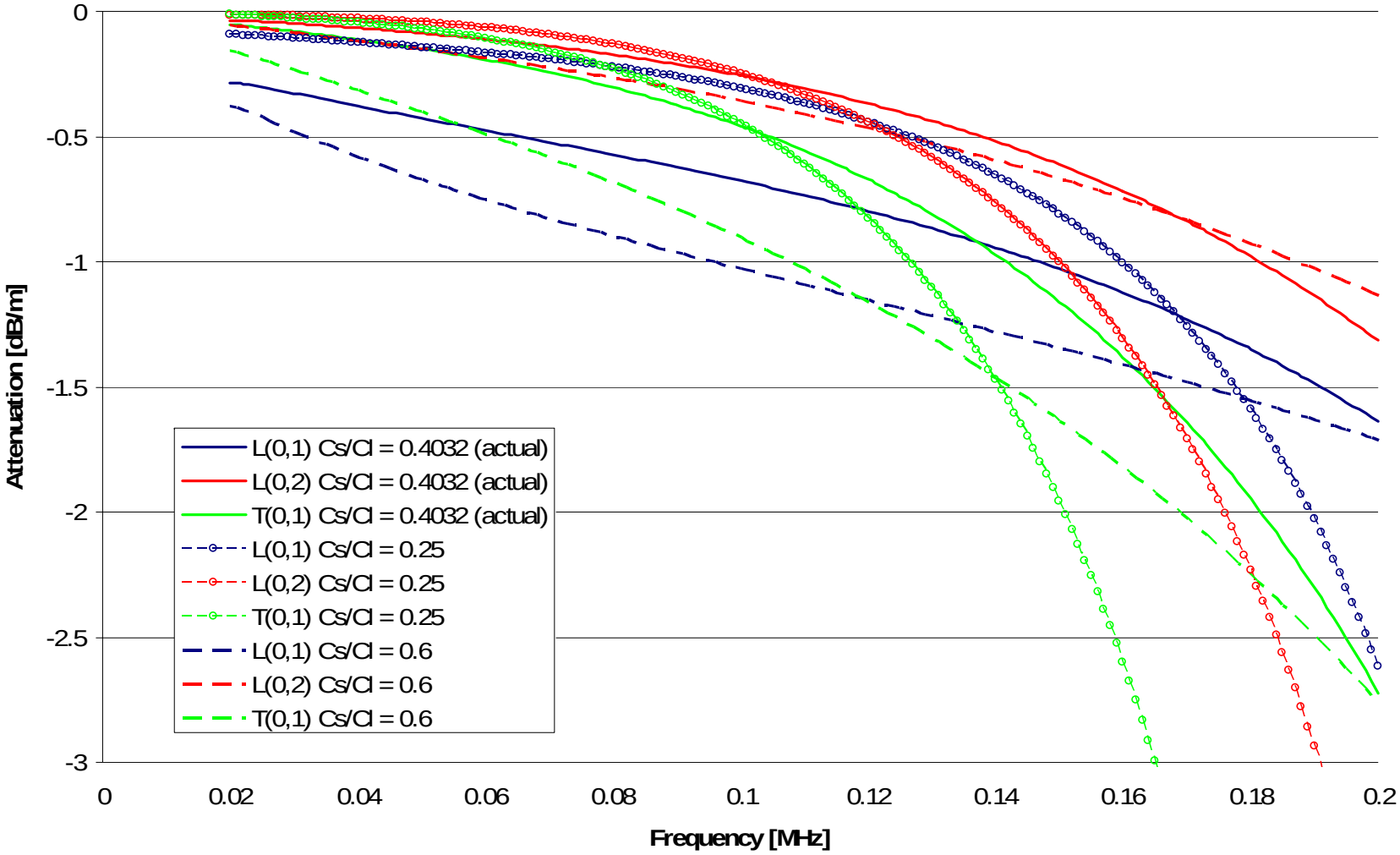

Figure 6.8 Attenuation dispersion curve for a pipe with B50 coating, illustrating the effect of variation in wave velocity. Results are shown for the ratio of shear velocity to longitudinal velocity. The actual ratio is plotted along with the common shear wave velocity approximation of $0.6C_L$ and a smaller approximation of $0.25C_L$. Results show that the L(0,2) is relatively inert at low frequencies. The T(0,1) and L(0,1) modes are more drastically affected at low frequencies. Varying the velocity ratio changes the shape of the attenuation dispersion curves rather than just scaling them.

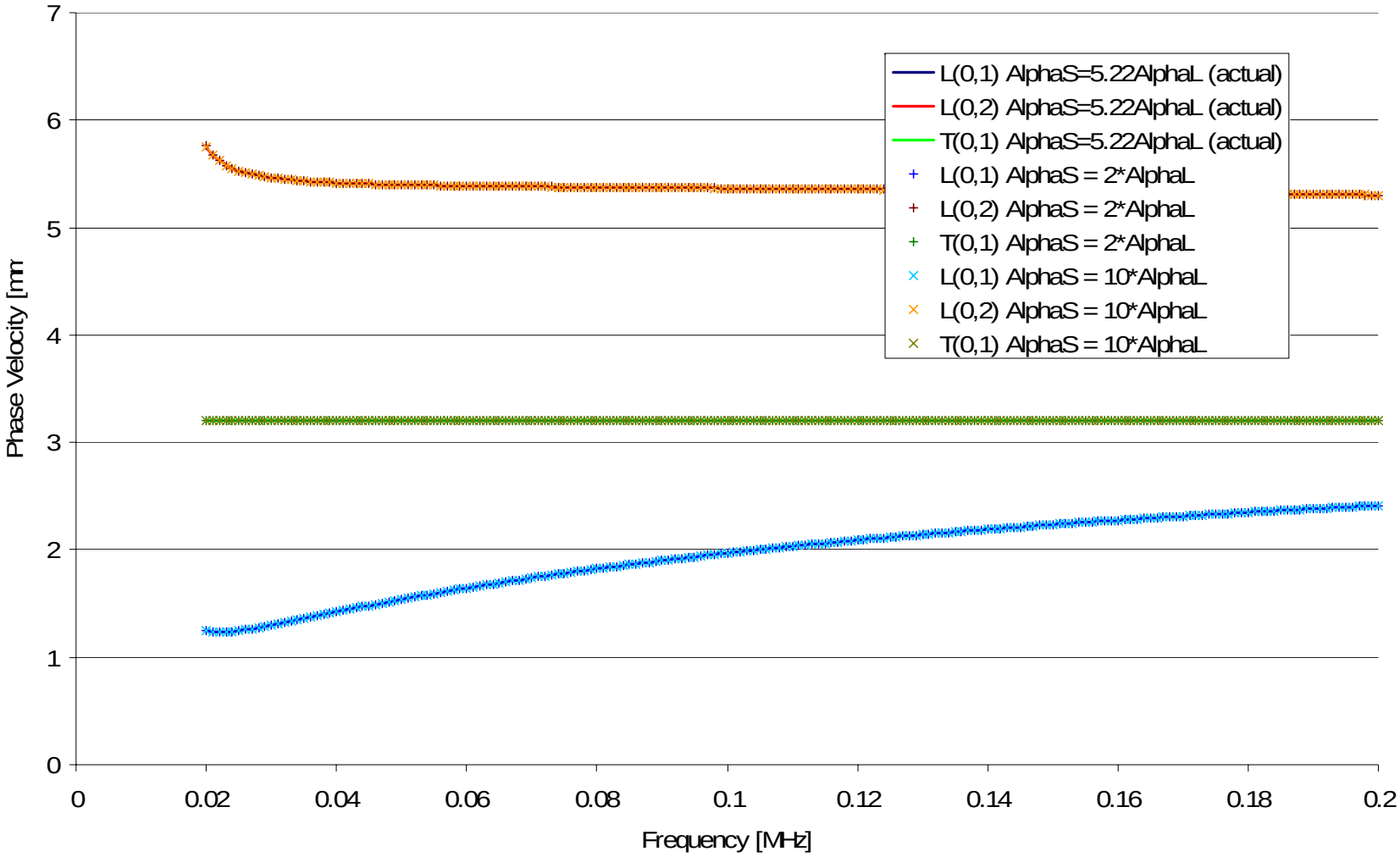

Figure 6.9 Phase velocity dispersion curve for a pipe with B50 coating, illustrating the effect of variation in attenuation constants. Results are shown for the shear attenuation constant as a multiple of the longitudinal attenuation constant. The actual relationship is displayed as well as a smaller approximation of $\alpha_S=2\alpha_L$ and a larger approximation of $\alpha_S=10\alpha_L$. Results show that variation in bulk wave attenuation has no effect on phase velocity.

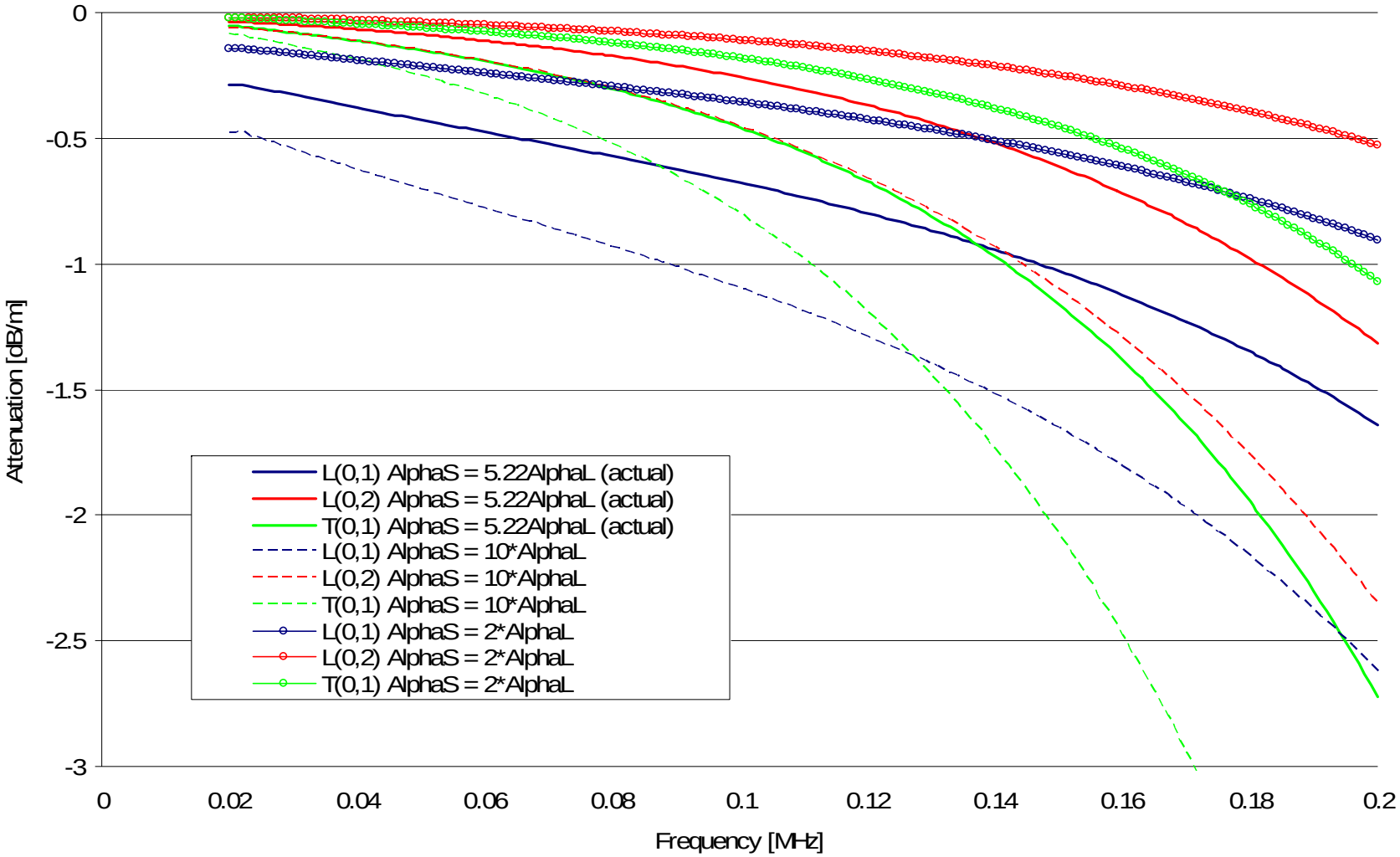

Figure 6.10 Attenuation dispersion curve for a pipe with B50 coating, illustrating the effect of variation in attenuation constants. Results are shown for the shear attenuation constant as a multiple of the longitudinal attenuation constant. The actual relationship is displayed as well as a smaller approximation of $\alpha_S=2\alpha_L$ and a larger approximation of $\alpha_S=10\alpha_L$. Results show that variations in bulk wave attenuation have a scaling effect on the attenuation dispersion curves. The effects of the variations increase monotonically with frequency for the range shown. Effects on L(0,2) and T(0,1) are minor at low frequencies.

Results and Discussion

Reviewing Figures 6.2 through 6.10, the following observations can be made:

- Variations in the coating properties have a much more pronounced effect on the attenuation dispersion curves, as opposed to the phase velocity dispersion curves.
- It appears that variations in the bulk wave velocities and bulk wave attenuation constants do not have a dramatic effect on the phase velocity dispersion curves for the values tested.
- Small differences in the phase velocity dispersion curves can be seen for the different values of coating density and thickness, with the change caused by thickness variation being most prominent.
- A decrease in phase velocity is seen with increasing coating thicknesses at low frequencies.
- A decrease in phase velocity is seen with increasing coating density.
- Attenuation is affected most significantly by changes in coating thickness.
- The L(0,2) and T(0,1) mode are less attenuative than the L(0,1) mode at low frequencies.

Based on the above observations, several conclusions can be drawn. Most importantly, measuring the coating thickness accurately is a critical task as the attenuation dispersion curves are significantly affected by this parameter. The phase velocity dispersion curves are also moderately affected and therefore, a large error in thickness estimation could lead to incorrect defect location and inspection distance predictions. For the same reasons, an accurate density measurement must be taken.

Based on Figures 6.7 and 6.8, it is reasonable to state that if an accurate longitudinal velocity measurement is taken, a shear velocity approximation can be made with very little introduced error for low frequencies. This is advantageous as shear wave probes are more costly than their longitudinal counterparts and in-turn will significantly increase the cost and complexity of a coating characterization tool.

The same conclusion is reached for the shear wave attenuation constant as was for the shear wave velocity. If an accurate longitudinal attenuation constant can be measured, the shear wave attenuation constant can be approximated. Error in this approximation will only affect the attenuation dispersion curves by a fraction of a decibel and will have virtually no effect on the phase velocity dispersion curve. By making this shear attenuation approximation, the need for a shear wave transducer in a coating evaluation tool is completely eliminated. It is believed that the level of error which is introduced through these estimations is acceptable when compared to the cost-benefit of eliminating such a probe from the final tool design.

7. VECTOR Tool

In-situ pipeline coating evaluation is invariably needed as coating properties are drastically affected by age and surrounding environment. A schematic of a portable, ultrasonic, coating-evaluation tool, as proposed by FBS, inc., is shown in Figure 7.1. Such a tool would be used for material characterization, establishment of inspectability, and coating integrity investigation.

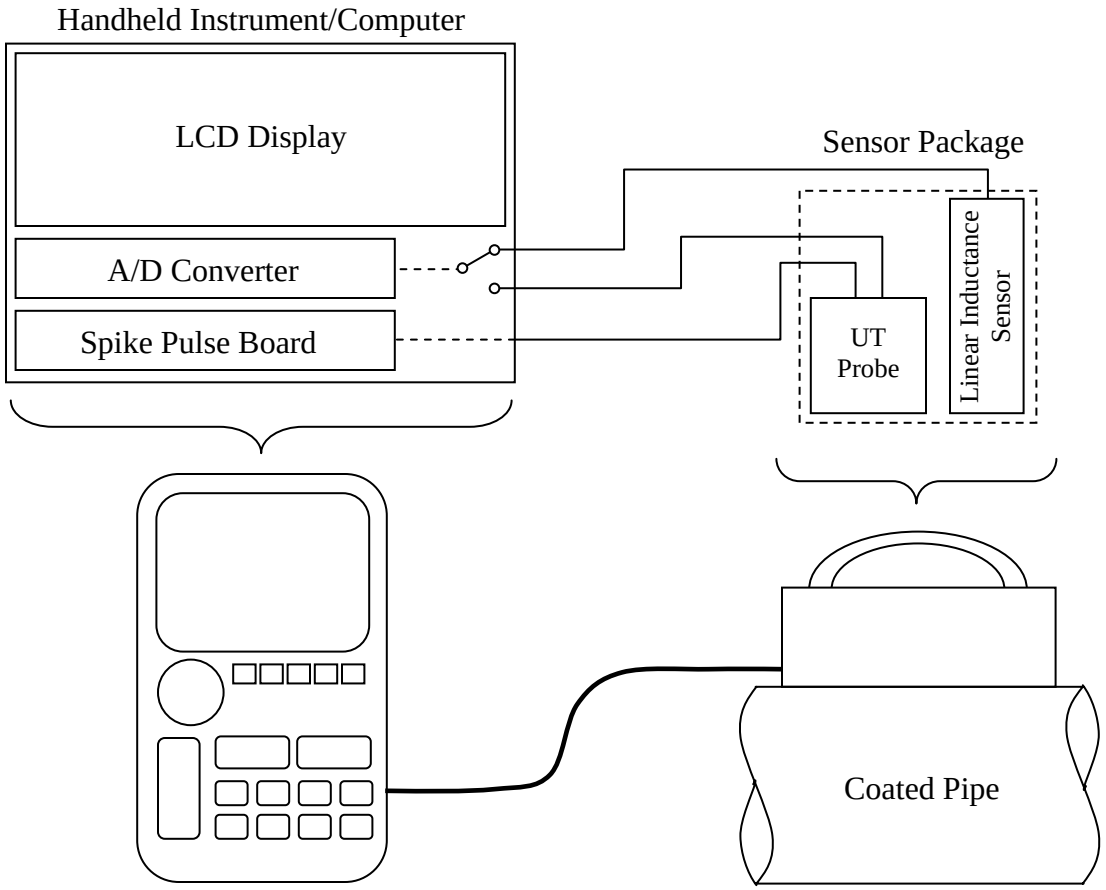

Figure 7.1 Schematic of a handheld, ultrasonic, coating-evaluation tool.

Interface pulse reflections will be gated by the user via a software interface designed for inexperienced users with minimal training. Data analysis will be done in near real-time aboard the handheld computer with results being viewable on an LCD display.

While the design of the handheld instrument/computer will be the result of a Phase II effort, a preliminary design and prototype sensor package has been completed and tested. As illustrated in Figure 1, the sensor package consists of a longitudinal-wave, ultrasonic transducer at normal incidence, and a linear inductance sensor for coating thickness acquisition. Design drawings of the ViscoElastic-Coating Technology-Oriented

Reconnaissance (VECTOR) instrument can be seen in Figure 7.2. Figure 7.3 shows a three-dimensional model of VECTOR with the key features labeled.

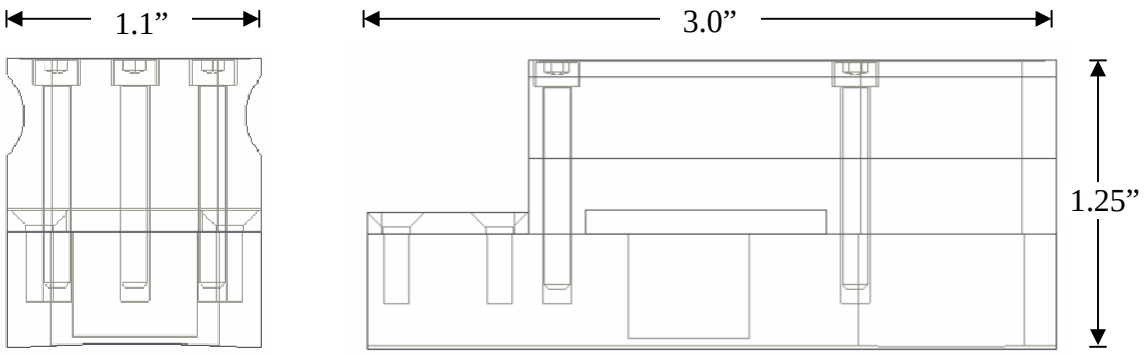

Figure 7.2 Dimensions of VECTOR sensor package

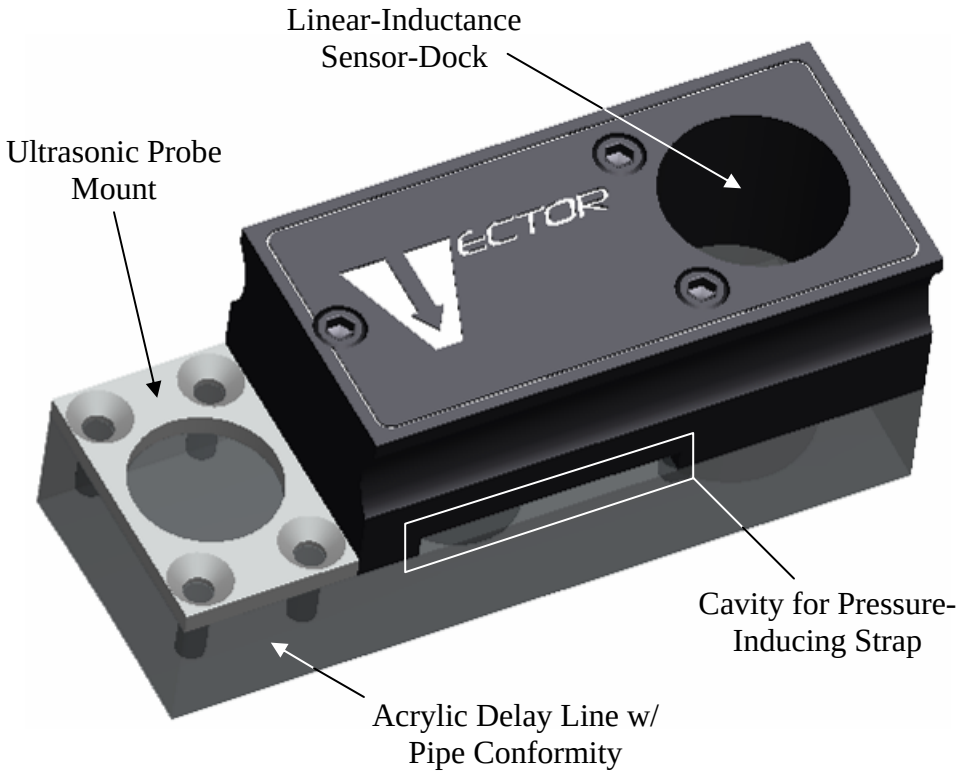

Figure 7.3 Illustrated model of VECTOR device showing key design points

The tool is designed to have a removable acrylic delay-line with the pipe conformity machined directly into the bottom of the delay-line. In this manner, the tool can easily be adapted for use on differently sized pipe. A docking station for the linear-inductance sensor was built into the instrument to that the coating thickness near the point of ultrasonic inspection can be measured. The linear-inductance sensor can then be removed to perform thickness mapping, if desired. In a similar manner, the transducer mount was designed to allow rapid exchange of transducers, if different frequencies are required. The mount is removable so that various sized transducers can still be used with the tool. To ensure intimate coupling between the delay-line and the coating, a cavity was designed into the device so that a strap could be used to apply pressure to the tool if necessary. Future versions of VECTOR may also incorporate a temperature sensor to monitor the coating temperature at the time of data collection. This may be important for cataloging coating properties as viscoelastic behavior is substantially modified by temperature. Figure 7.4 is a photograph of the completed prototype VECTOR sensor housing. Field-testing of the VECTOR instrument will be addressed in the following section.

Figure 7.4 Photograph of Prototype VECTOR sensor-housing device.

Then linear inductance sensor, or linear variable differential transformer, consists of a series of wire coils wrapped around an isolated, magnetic, cylindrical core. As the magnetic core slides through the coils a current is generated, which is then converted into a voltage. Calibrating the sensor to a specific metal allows the voltage reading to be translated into a standoff measurement. Therefore, if calibrated to a coated pipe, the sensor can be used to measure the coating thickness. The particular sensor used has a dynamic range of 8mm and a resolution of 0.01mm. Two screen shots of the LabView interface that was created to control the linear inductance sensor can be seen in Figure 7.5 on the next page. The software was programmed to dynamically control the voltage range of the A/D converter for maximum resolution capability. Another key feature of the software is the built-in calibration routine designed for maximum control of the sensor.

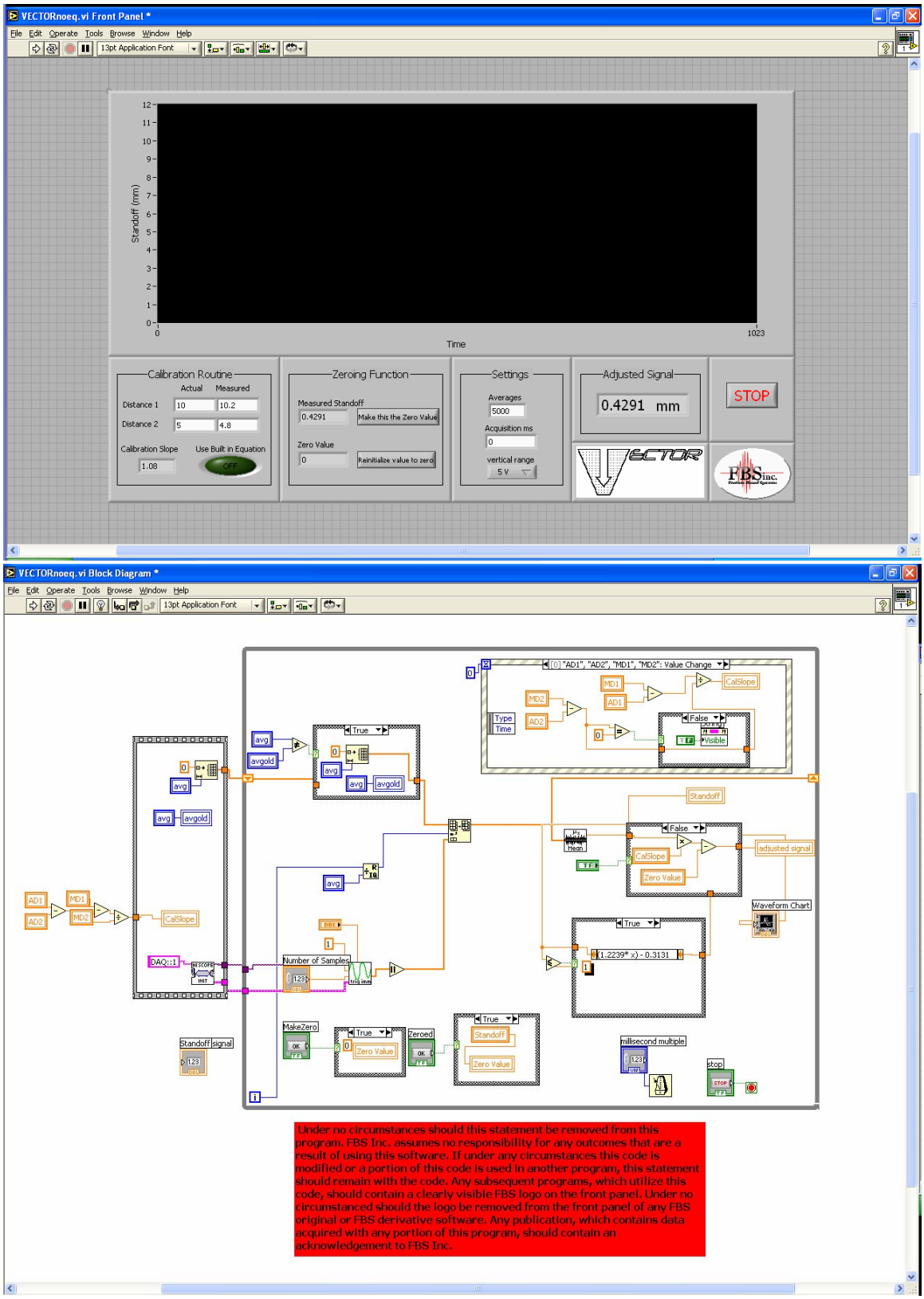

Figure 7.5 LabView code and interface designed for control of the linear inductance sensor.

8. VECTOR Field Test (Johnson City, NY)

Field-tests of the VECTOR instrument were hosted by the Northeast Gas Association on May 16th -19th at NY Search test facility in Johnson City, New York. The instrument was used to characterize two coatings, a Fusion Bonded Epoxy on a 12" diameter pipe, and what was believed to be a Fibrous Coal Tar on a 16" diameter pipe. The results from the coating analysis were then compared to the results of an ultrasonic guided-wave pipe inspection, which was being performed concurrently. The results for each coating are presented below with a discussion of the results, and their relation to the guided-wave inspection, to follow. The analysis procedure is not described here as this can be found in previous sections.

Fusion Bonded Epoxy

Figure 8.1 shows a photograph of the VECTOR tool on the coated pipe. A thickness measurement performed with the linear-inductance sensor produced a measured coating thickness of 0.576 mm. Based on this measurement, a 10 MHz broadband transducer was used to perform the coating characterization. The RF waveform obtained can be seen in Figure (8.2a) and the Fourier transforms of the reference wave-packet, front-wall wave-packet, and coating interface wave-packet can be seen in Figure (8.2b).

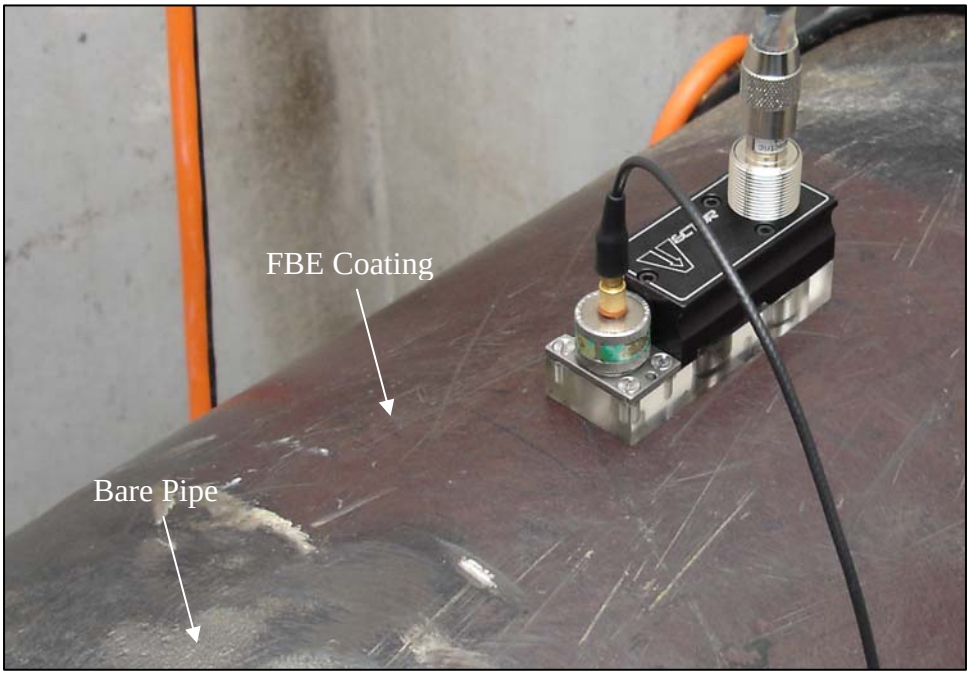

Figure 8.1 Photograph of VETOR tool on 12" diameter pipe with Fusion Bonded Epoxy coating.

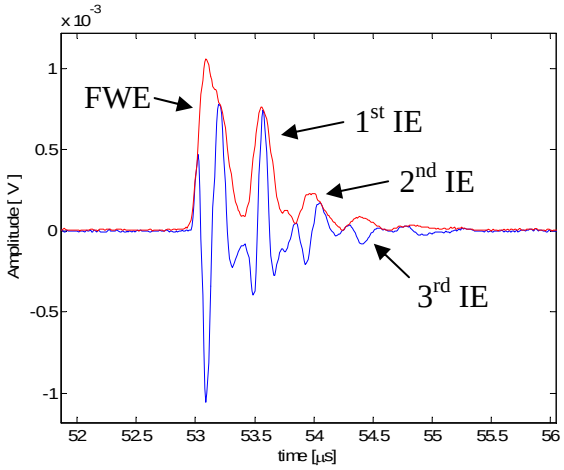

Figure 8.2a RF Waveform showing multiple reflections from the coating-pipe interface.

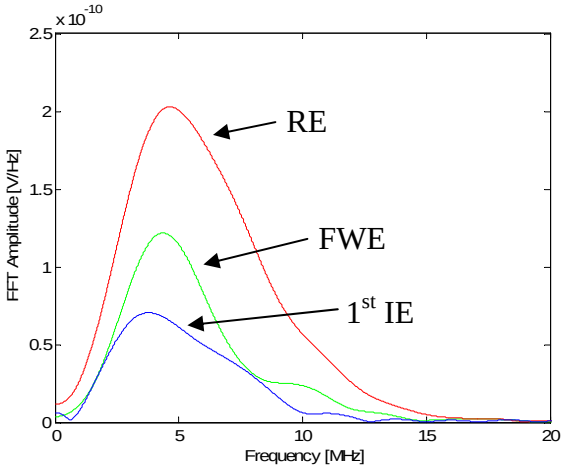

Figure 8.2b Fourier Transforms of the reflected signals. The reference waveform is not shown in (1a).

In Figures (8.2a) and (8.2b), FWE refers to the Front-Wall Echo, IE refers to the Interface Echo, and RE refers to the Reference Echo. The reference RF waveform is not shown in Figure 8.2 because is a constant reference, independent of the coating.

The bulk-wave attenuation result in shown, in Figure 8.3. The attenuation shows an approximately linear trend with frequency. Based on this information, and the measured coating density, the guided-wave attenuation and phase velocity dispersion curves were generated. These can be seen in Figures 8.4 and 8.5, on the next page.

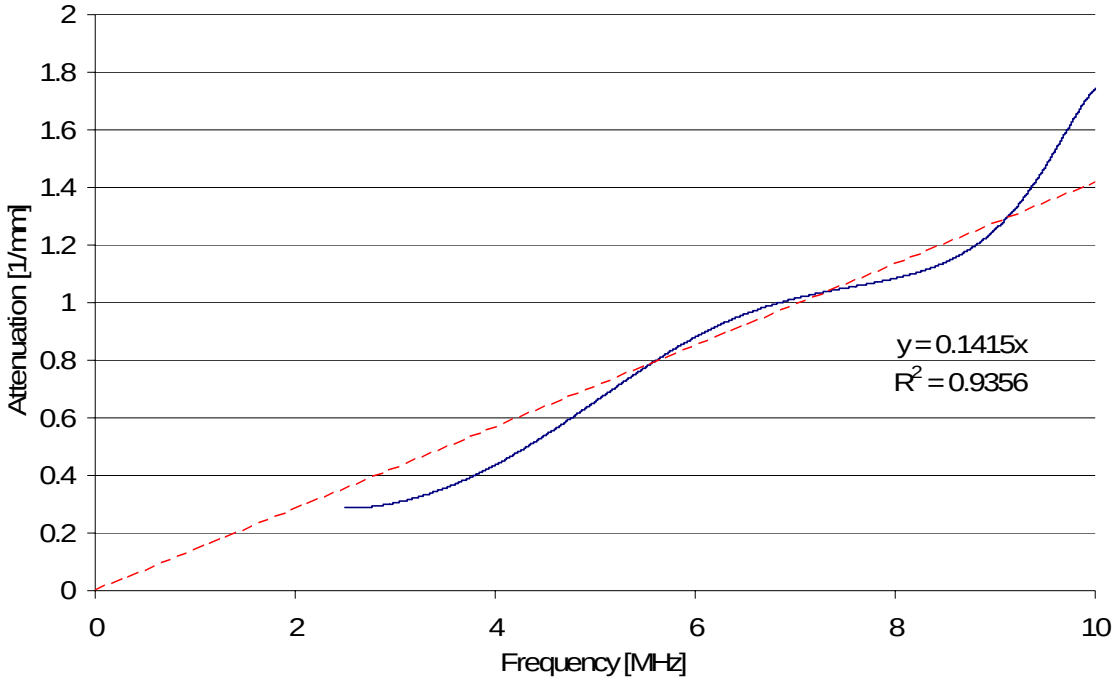

Figure 8.3 Bulk wave attenuation trend for Fusion Bonded Epoxy coating on 12” diameter pipe.

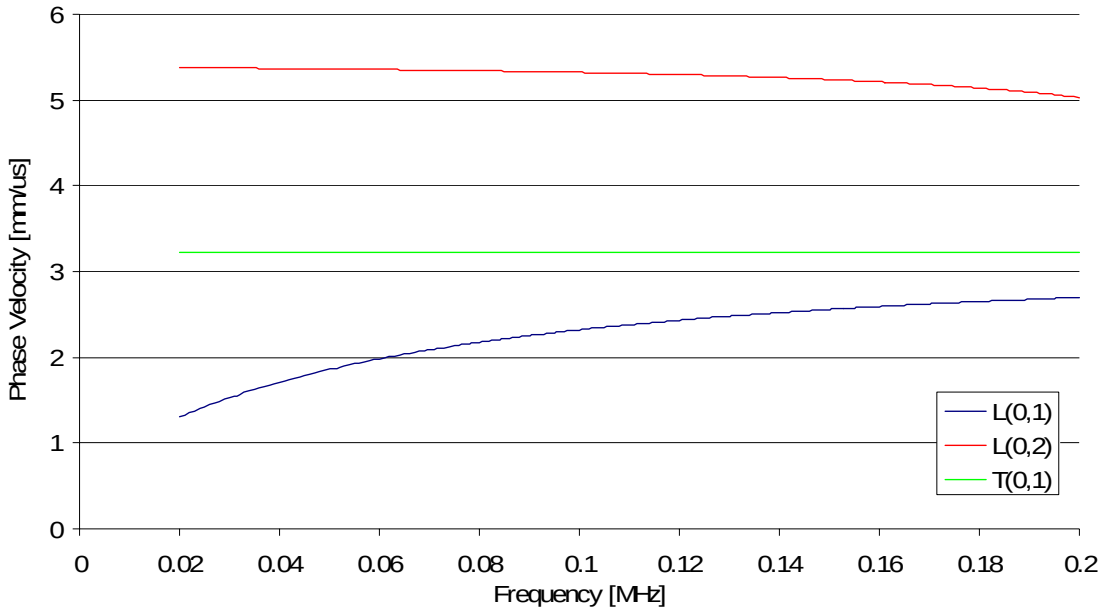

Figure 8.4 Phase velocity dispersion curve for 12" diameter pipe with Fusion Bonded Epoxy coating.

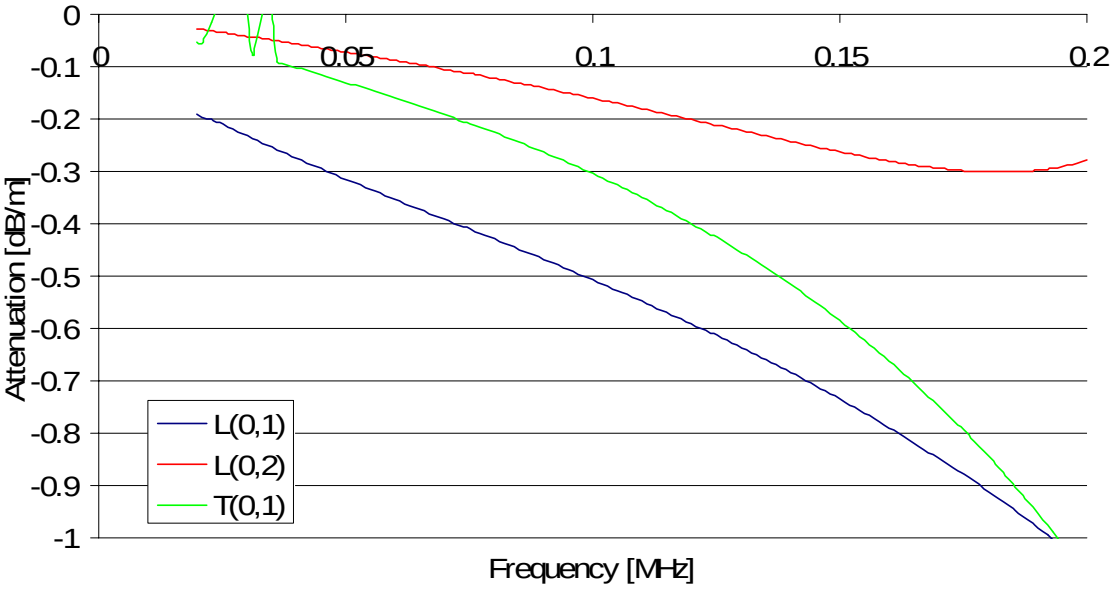

Figure 8.5 Attenuation dispersion curve for 12" diameter pipe with Fusion Bonded Epoxy coating.

Fibrous Coal Tar

Figure (8.6a) shows a photograph of the VECTOR tool on the 16” pipe with Fibrous Coal Tar coating and (8.6b) shows a close-up image of the coating, making visible the fibers and the coating thickness. A thickness measurement performed with the linear-inductance sensor produced a measured coating thickness of 4.42 mm. Based on this measurement, it was determined that a 5 or 10 MHz broadband transducer would be sufficient to perform the coating characterization. Both were used with similar results. The results for the 10 MHz transducer are presented here as it is slightly more broadband and therefore produces more useable information. The RF waveform obtained can be seen in Figure (8.7a) and the Fourier transforms in (8.7b).

Figure 8.6a VECTOR tool on 16” diameter pipe with Fibrous Coal Tar coating.

Figure 8.6b Close-up of Fibrous Coal Tar coating.

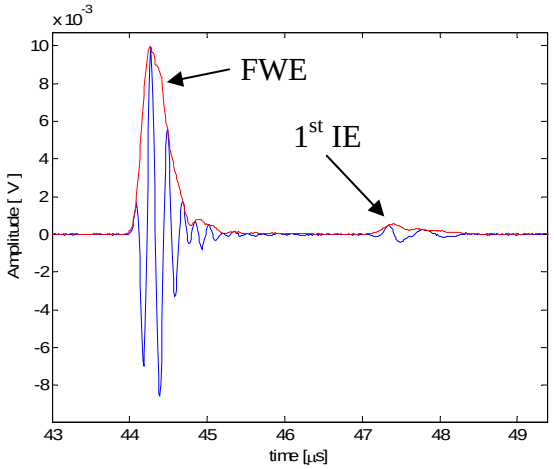

Figure 8.7a RF Waveform showing single reflection from the coating-pipe interface.

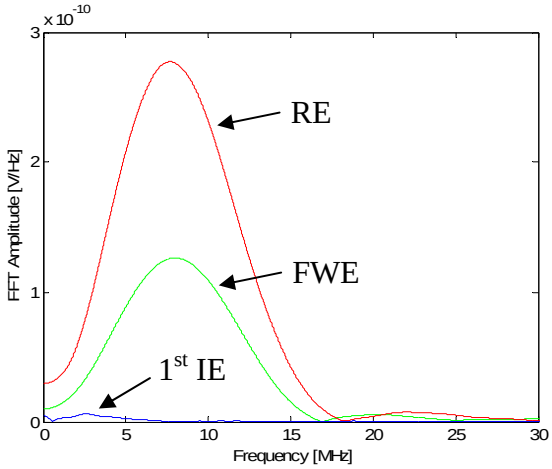

Figure 8.7b Fourier Transforms of the reflected signals.

The bulk-wave attenuation result in shown, in Figure 8.8. The attenuation data agrees well with the linear trendline. Based on this information, and the measured coating density, the guided-wave attenuation and phase velocity dispersion curves were generated. These can be seen in Figure 8.9 and Figure 8.10 on the next page.

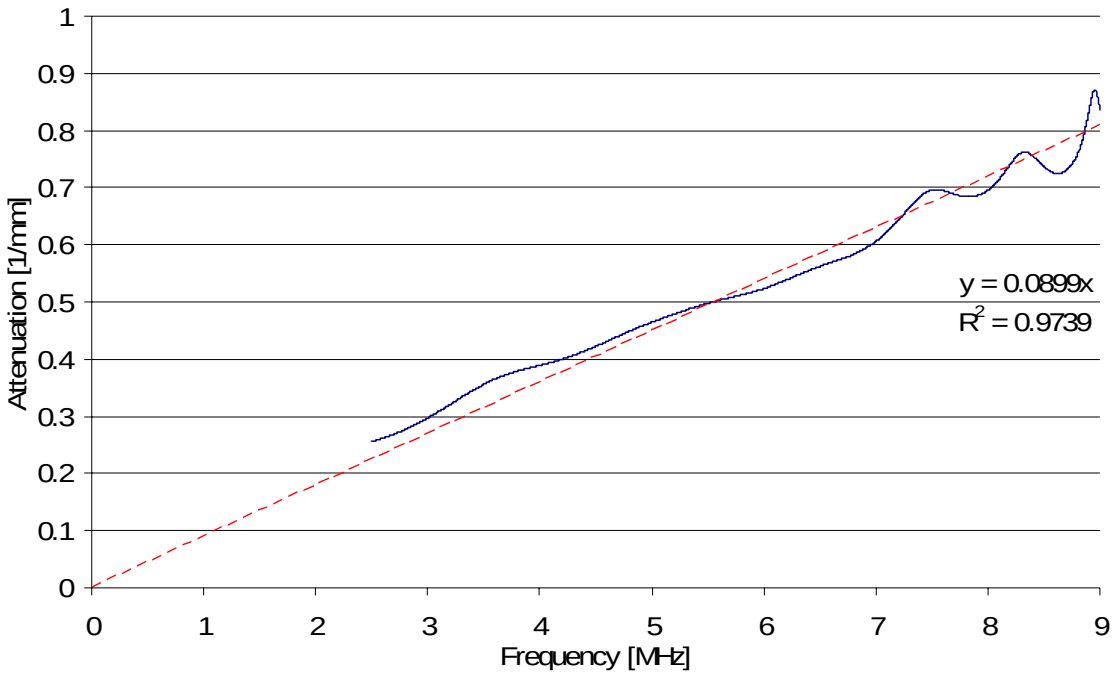

Figure 8.8 Bulk wave attenuation trend for Fibrous Coal Tar coating on 16" diameter pipe.

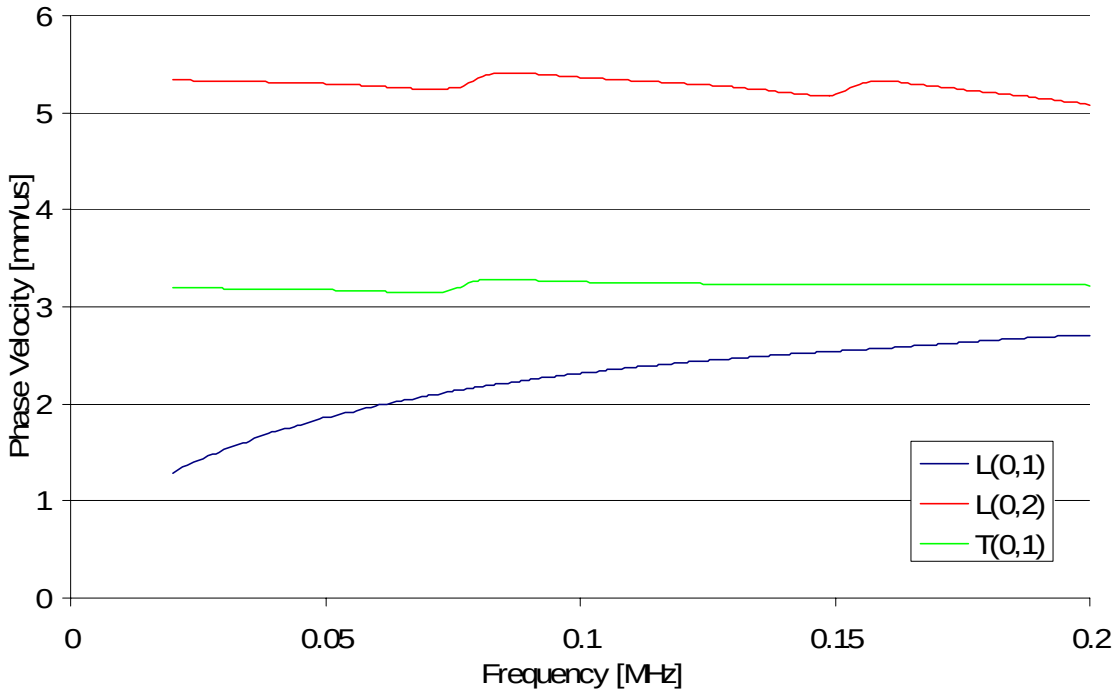

Figure 8.9 Phase velocity dispersion curve for 16" diameter pipe with Fibrous Coal Tar coating.

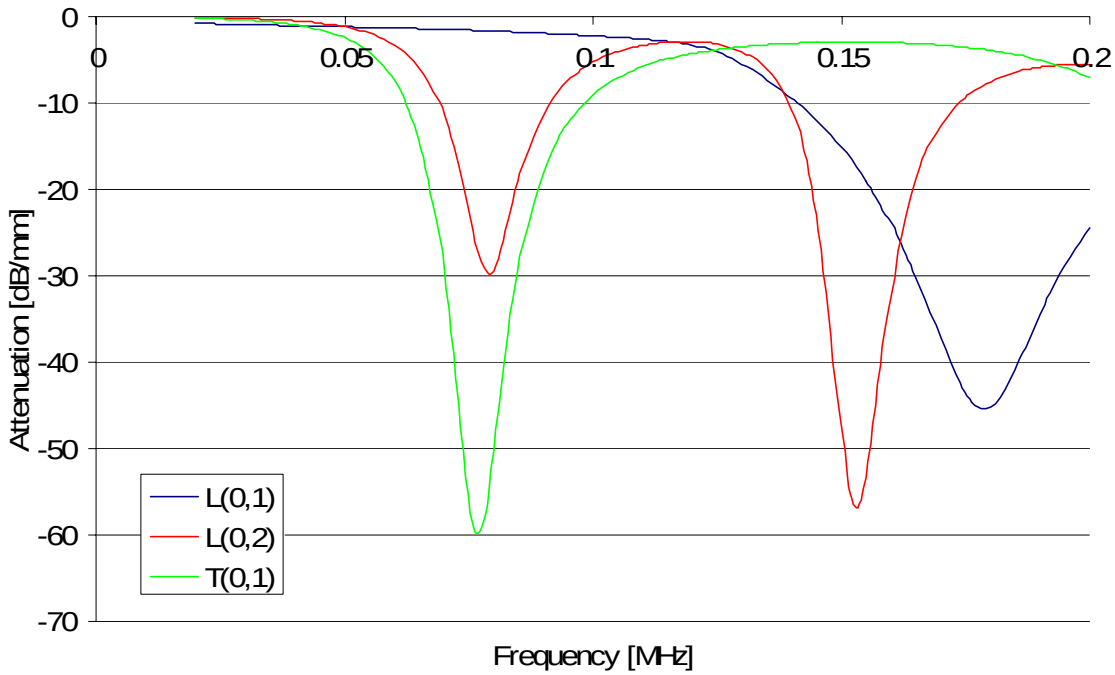

Figure 8.10 Attenuation dispersion curve for 16" diameter pipe with Fibrous Coal Tar coating.

Results & Discussion

All measured properties and approximated shear-wave properties obtained from the field testing of VECTOR are summarized in Table 8.1. Using the information contained in Table 8.1, the attenuation dispersion curves were generated. These curves can be seen in Figures 8.5 and 8.10.

Coating	t (mm)	ρ (g/cc)	C_L (mm/us)	C_S (mm/us)	α_L/ω (1/mm)	α_S/ω (1/mm)
12" FBE	0.576	0.5	2.70	1.22	0.022	0.113
16" FCT	4.42	0.4	2.82	1.27	0.014	0.072

Table 8.1. Coating properties measured using VECTOR tool. Shear wave approximations were made as per earlier discussion.

Based on the attenuation dispersion curve for the 12" diameter pipe with Fusion Bonded Epoxy coating, a test procedure would be recommended which would advise the use of the second longitudinal mode over the first torsional or first longitudinal mode. In this case, this recommendation would hold for all frequencies shown in Figure 8.5. If a torsional test is desired, it would be recommended to use as low a frequency as possible to avoid excessive attenuation.

Using the information provided in Figure 8.10, for the 16" diameter pipe with Fibrous Coal Tar coating, it would be advised to use the second longitudinal mode at frequencies

less than 50 kHz. Above this frequency, the curves show that the first longitudinal mode would be the optimal inspection mode, though no known commercial inspection tool will generate this mode with high efficiency and therefore is not generally used for pipeline inspection. Given this information, it would be recommended that the L(0,2) mode be used at all frequencies up to approximately 125 kHz, at which point it becomes more efficient to use the first torsional mode.

The recommendations made above agree with the observations of the team performing the guided wave inspection at the test site. In both cases it was found that the second longitudinal mode was the least attenuative at the chosen inspection frequencies, which ranged from 30 to 80 kHz for the 12” pipe and up to 50 kHz for the 16” pipe.

Comparing the field coating results to those of the laboratory specimens in Section 5, it can be said that for the given coating properties and thicknesses the Fibrous Coal Tar coating is slightly more attenuative than the Bitumen Tape (BT) coating and the Fusion Bonded Epoxy coating on the 12in. field-pipe is comparable to the B50 mastic coating on the lab-pipe. Based on the detailed results contained in the NE Gas Report [2006], these attenuation predictions appear realistic as the penetration distance for the 12in. FBE pipe was much greater than that of the 16in. FCT pipe.

9. Viscoelastic Material Properties

As there is no comprehensive source for viscoelastic material properties, it would be useful to derive the viscoelastic material properties from the acoustic data presented in previous sections. Unlike elastic materials, viscoelastic material properties have an imaginary component. This results from the solution of the wave equation for viscoelastic materials. Detailed solutions of the wave equation for viscoelastic media can be found in Christensen [1981], Haddad [1995], or Barshinger [2001].

Following Luo [2005], the measured phase velocities and attenuation constants can be used to calculate the frequency dependent, complex wave velocity,

$$c^*(\omega) = \frac{1}{\frac{1}{c(\omega)} - i\frac{\alpha(\omega)}{\omega}}. \qquad [9.1]$$

In a similar manner, the complex shear modulus, G^*, and the complex Young's modulus, E^*, can be calculated from,

$$G^* = c_2^{*2}\rho, \qquad [9.2]$$

and,

$$E^* = \left[\frac{3 - 4\left(\frac{c_2^*}{c_1^*}\right)^2}{1 - \left(\frac{c_2^*}{c_1^*}\right)^2}\right] G^*. \qquad [9.3]$$

In Eqs. [9.2] and [9.3] the subscript 1 refers to longitudinal wave properties, and subscript 2 refers to shear wave properties. The real parts of Eqs. [9.2] and [9.3] are related to the stiffness of the viscoelastic material, while the complex parts are associated with the energy dissipation of the material. With this knowledge of the viscoelastic material properties, it is possible to calculate the Rayleigh damping associated with the material, which is useful for numerical modeling. This will be presented in the section regarding finite-element modeling. The viscoelastic material properties, calculated using Eqs. [9.1], [9.2], and [9.3], for the coating materials used in this study can be found in Table 9.1 on the following page.

Coating	c_L* [km/s]	c_S* [km/s]	G* [Pa]	E* [Pa]
2LFBE	2.9881e3 +1.8825e2i	1.3234e3 +1.8759e2i	6.8649e8 +1.9861e8i	1.9019e9 +5.1464e8i
B50	1.8816e3 +1.8591e2i	6.5099e2 +2.5388e2i	4.3119e8 +3.9666e8i	1.2756e9 +1.1015e9i
1LFBE	1.8954e3 +9.3632e1i	8.4938e2 +9.4961e1i	5.6995e8 +1.2905e8i	1.5720e9 +3.3241e8i
BT	1.8850e3 +1.6833e2i	7.3923e2 +2.9880e2i	5.4861e8 +5.3011e8i	1.6305e9 +1.4333e9i
B300M	1.4871e3 +1.3830e2i	6.5107e2 +1.3725e2i	2.4303e8 +1.0723e8i	6.7926e8 +2.7957e8i
EP	1.6691e3 +1.3460e2i	6.7746e2 +2.5039e2i	3.9625e8 +3.3925e8i	1.1659e9 +9.0546e8i
WT	1.5982e3 +5.3699e1i	7.0391e2 +1.0643e2i	4.8416e8 +1.4983e8i	1.3492e9 +3.8041e8i

Table 9.1 Estimated, complex, viscoelastic material properties for coatings under study.

10. Finite-Element Modeling of Coated Pipe

The effects of structural irregularities on guided-wave propagation in pipeline are of much interest. Unfortunately, the differential equations which govern wave propagation in pipeline cannot be solved analytically when anomalies such as defects, elbows, and irregular coating patterns exist within the pipe. In circumstances such as these, Finite-Element Modeling (FEM) offers a powerful tool for the exploration of such complex physical phenomena.

Zhang [2005] and Luo [2005] provide a thorough study of axisymmetric wave propagation and focusing in pipe, in some cases with coating. In this study, guided-wave propagation in coated pipe is explored further. The viscous damping caused by the viscoelastic coating, is incorporated in the model as a stiffness proportional damping factor, per Luo [2005]. Luo shows that if the complex material constants of the coating are known, the stiffness proportional damping factor can be calculated from,

$$\beta_R = \frac{E''}{\omega E'} - \frac{\alpha_R}{\omega^2}, \qquad [10.1]$$

which simplifies to,

$$\beta_R = \frac{E''}{\omega E'} \qquad [10.2]$$

for high frequencies, such as those in the ultrasonic range. Based on Eq. [10.2] and the complex material properties determined by experiment in the previous section, the damping factors for the coatings under study can be found from Table 10.1 below.

Coating	$\omega\beta_R$
2LFBE	0.271
B50	0.864
1LFBE	0.211
BT	0.879
B300M	0.411
EP	0.777
WT	0.282

Table 10.1 Frequency dependent damping ratios for coatings under study.

Models, based on the dimensions of the actual pipe specimens used for experimental studies, were created. Excitation was done using a 7-cycle, 40kHz, Hanning-windowed toneburst, like that seen in Figure 10.1 on the next page. Loading was performed on the end of the pipe in manner that produced dominant L(0,2) mode propagation. All modeling was performed using ABAQUS/Explicit, an advanced finite-element modeling software package.

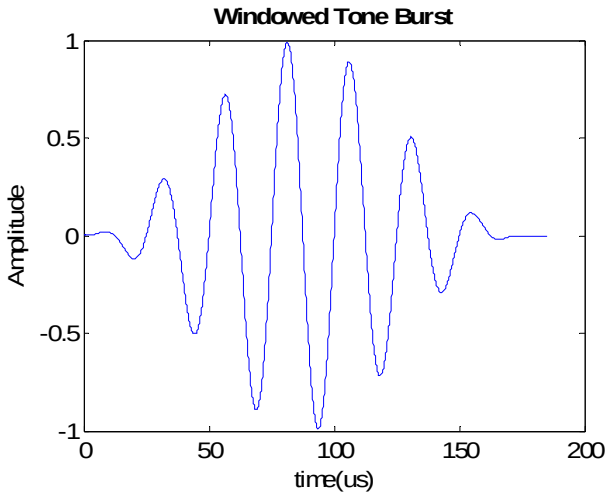

Figure 10.1 7-cycle, Hanning-windowed, 40kHz toneburst used for L(0,2) mode generation.

As an example of the visualization capabilities made possible by FEM, Figure 10.2 compares the wave propagation in a bare pipe with the wave propagation in a bare pipe of the same size. Although the calculation was performed for the entire pipe, for visibility reasons, the model has been sliced down the pipe's longitudinal axis and only one half is shown. In this figure, the same amount of time has elapsed for both the coated pipe and bare pipe. This can be seen by looking at the frame number in the upper right-hand corner or at the time information in the description of the models. Also, the color scales have been adjusted to be the same for both models. In both cases, wave packet has already been reflected from the back-wall of the pipe and is beginning the third trip along the pipe. This propagation path is shown in the figure. The Von Mises stress is the physical attribute which is being plotted.

Some very interesting information can be obtained from Figure 10.2. First, the attenuation introduced by the wax coating is significant compared to that of the bare pipe. This agrees with the analytic prediction and experimental results discussed in previous sections. Secondly, the group velocity is noticeably affected by the presence of the coating. Based on the data obtained from the model, the group velocity for the bare pipe is approximately 5.1 mm/us while the group velocity for the coated pipe is approximately 4.83 mm/us. This means that for very thick, attenuative coatings, the error in defect location predictions will increase with axial distance. This presents another reason for the necessity of coating considerations in guided-wave inspection.

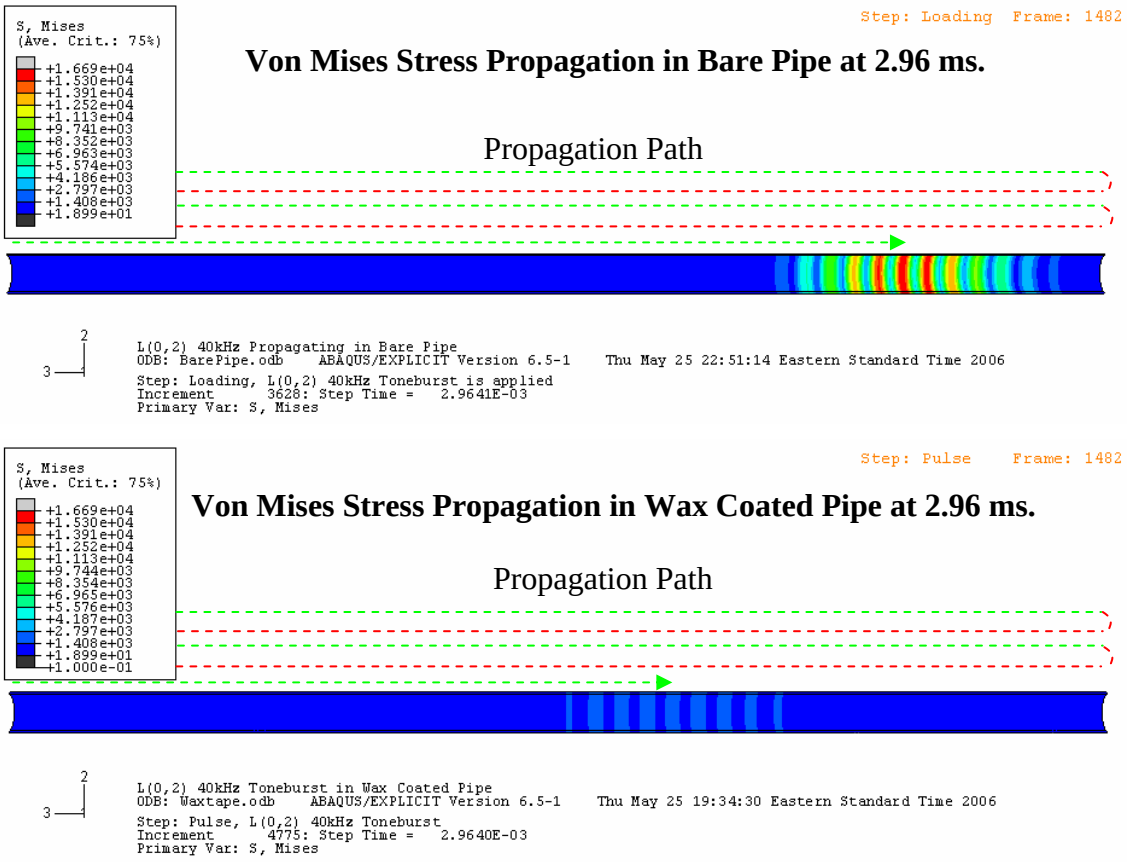

Figure 10.2 Comparison of 40kHz, L(0,2) mode propagation in a bare pipe (top) and a wax coated pipe (bottom). The green dotted-lines represent forward propagation and the red dotted-lines represent backward propagation. These results show that in addition to being highly attenuative, the wax coating alters the group velocity of the wave propagating in the coated pipe.

Figures 10.3 and 10.4 on the following page show contracted views of the wax coated pipe. The color scale representing the Von Mises stress has been decreased so as to see the stress leakage from the pipe into the coating. It is this leakage that is responsible for the attenuation of the guided-wave in the pipe. For the wax coating under investigation, the stress leakage into the coating is rapidly dissipated. For more elastic coating layers, the energy leakage might manifest in the second layer as an energy packet propagating at a velocity different than that of the energy in the pipe wall. This is a point for future study.

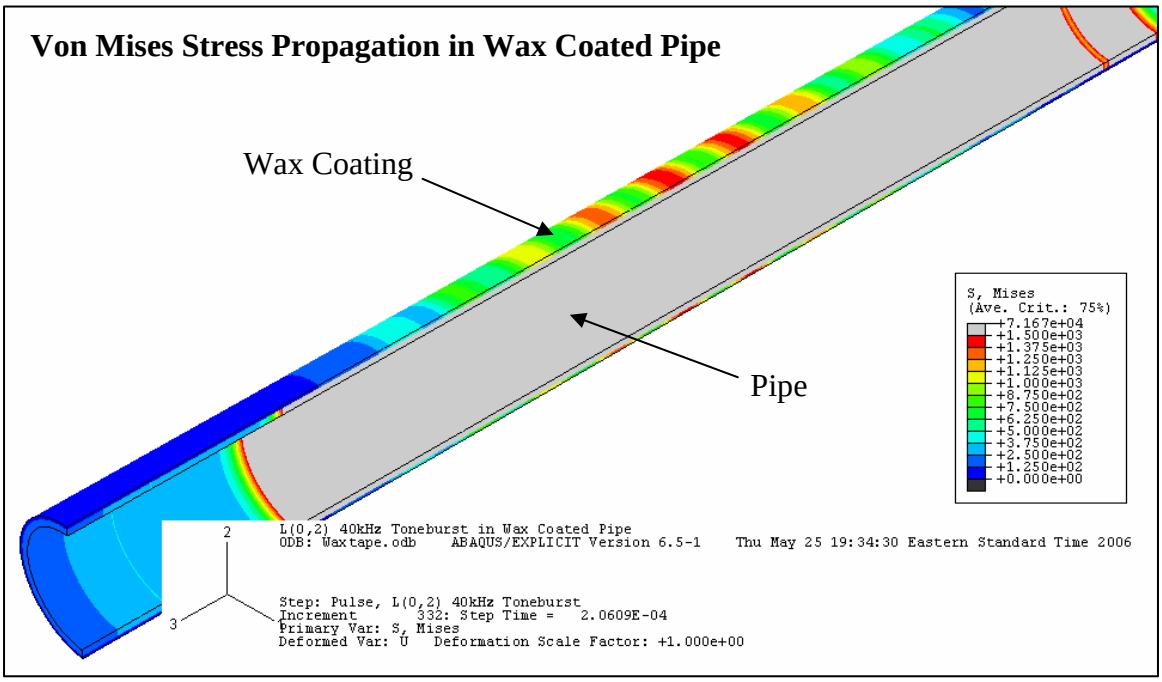

Figure 10.3 Contracted view of pipe showing energy leakage from the pipe wall into the wax coating. The gray color represents energy saturation in reference to the scale shown.

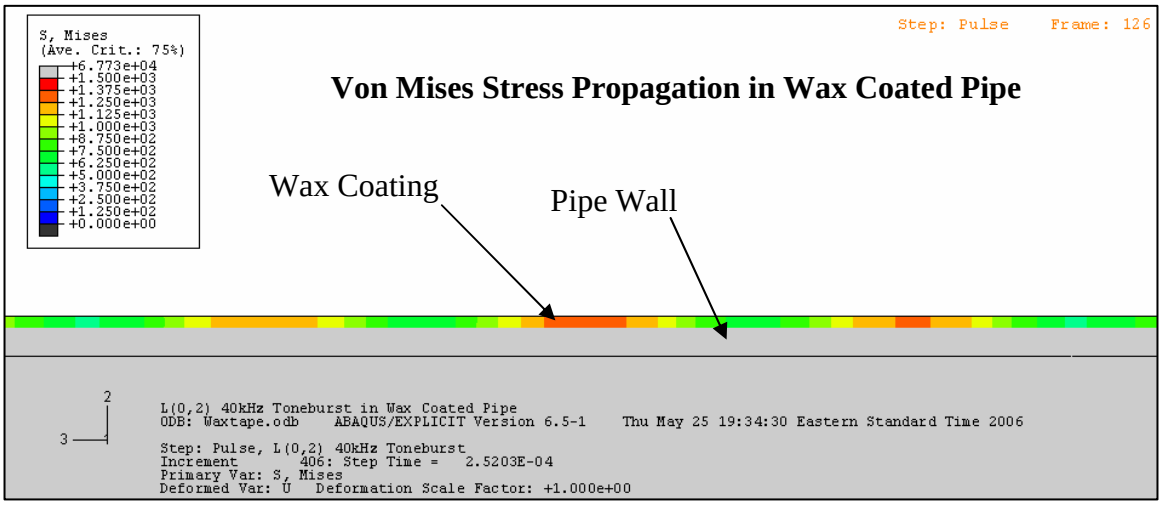

Figure 10.4 Contracted view of pipe showing energy leakage from the pipe wall into the wax coating. The gray color represents energy saturation in reference to the scale shown. This means that the energy present in the pipe is much large than that in the coating.

ABAQUS/Explicit models were created for three different cases: a bare pipe, a wax coated pipe, and a 2LFBE coated pipe. The axial particle displacement component at the end of the pipe, corresponding to the point of excitation, was recorded. An example waveform for the bare pipe can be seen in Figure 10.5. Figure 10.6 shows the analytic envelopes of the RF waveforms obtained for each pipe. The differences in velocity and attenuation can be more easily seen in this figure.

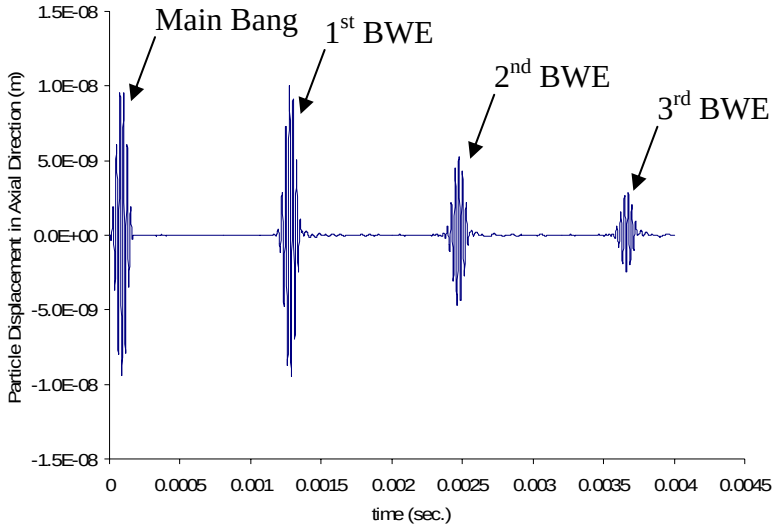

Figure 10.5 RF waveform obtained from FEM analysis for bare pipe.

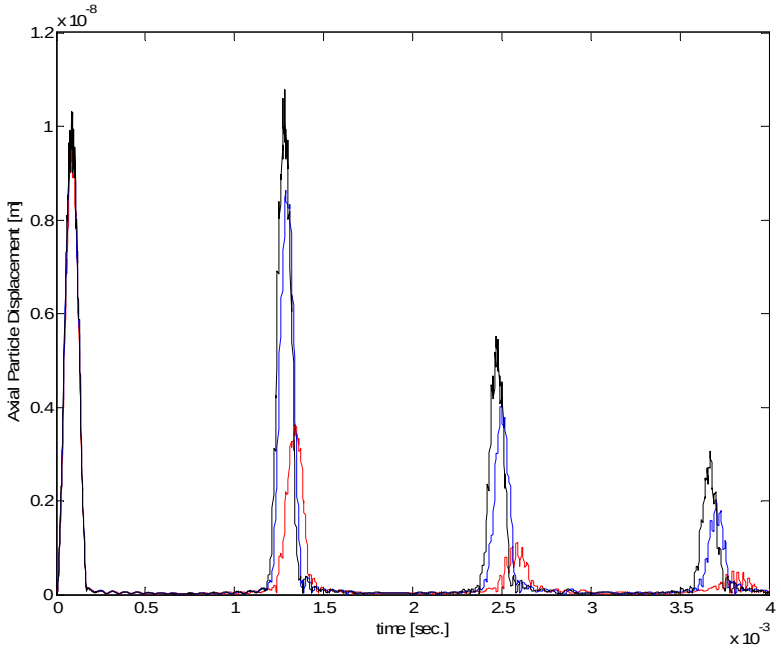

Figure 10.6 Analytic envelopes of bare pipe (black), 2LFBE coated pipe (blue), and wax tape coated pipe (red).

11. Guided Wave Focusing in Coated Pipes

Nearly all field evaluations of pipeline that take place today are done using axisymmetric excitation. Axisymmetric loading refers to the uniform loading of a pipe around the entire circumference (See Figure 11.1a). Advantages of this technique include its simple nature, less complex equipment requirements, and ease of interpretation of results. While axisymmetric loading is often sufficient, there are often times when it would be advantageous to have all the energy generated by the transducers to meet, constructively, at some desired point along the length and circumference of a pipe. This is achieved via guided wave focusing. Zhang [2005] provides a detailed review of the focusing technique.

By segmenting the inspection tool (See Figure 11.1b), and then phasing the individual segments, it is possible to create constructive wave interference at a desired point along a pipe. Figure 11.2, on the following page, shows the wave propagation profiles for the different types of loading. For the axisymmetric case, the energy is distributed evenly around the circumference of the pipe. For the focusing case, the energy is localized in a desired area.

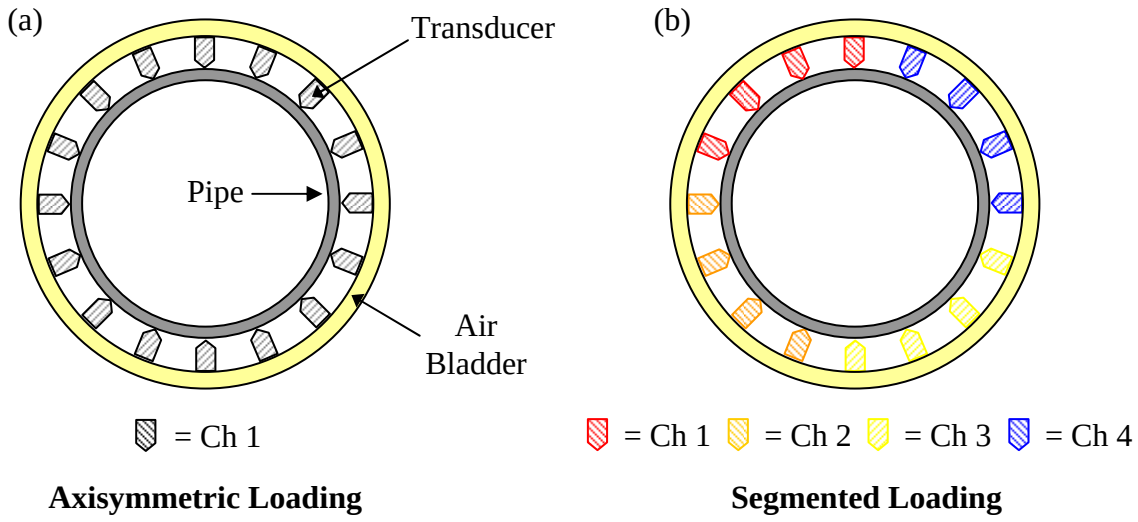

Figure 11.1 (a) Illustration of tool configuration for axisymmetric loading showing all transducers connected to one channel. (b) Tool configuration for focusing, which allows time delays (phasing) to be applied to individual channels.

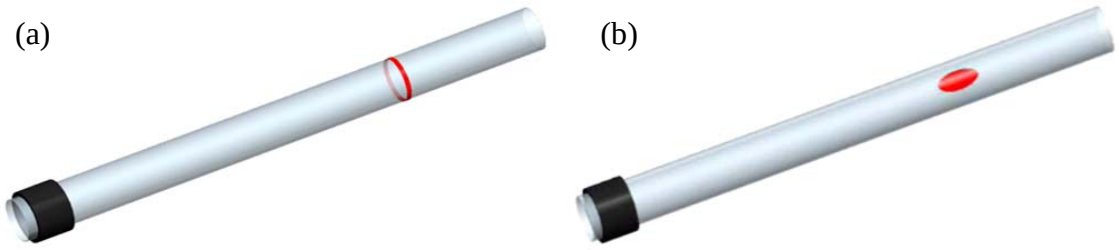

Figure 11.2 (a) Illustration of distribution of wave energy for axisymmetric loading. (b) Illustration of distribution of wave energy for focusing via phased loading.

The use of guided wave focusing has been proven to increase sensitivity, generate higher power penetration, and decrease false alarm rates. A majority of these studies though, were performed on bare pipe. For this reason it is desirable to examine some focusing results for the various coated pipe specimens introduced in the previous sections.

Experimental Verification of Guided Wave Focusing in Coated Pipe

An experiment was designed so as to assess guided wave focusing ability in pipe with various viscoelastic coatings. The experimental setup can be seen in Figure 11.3.

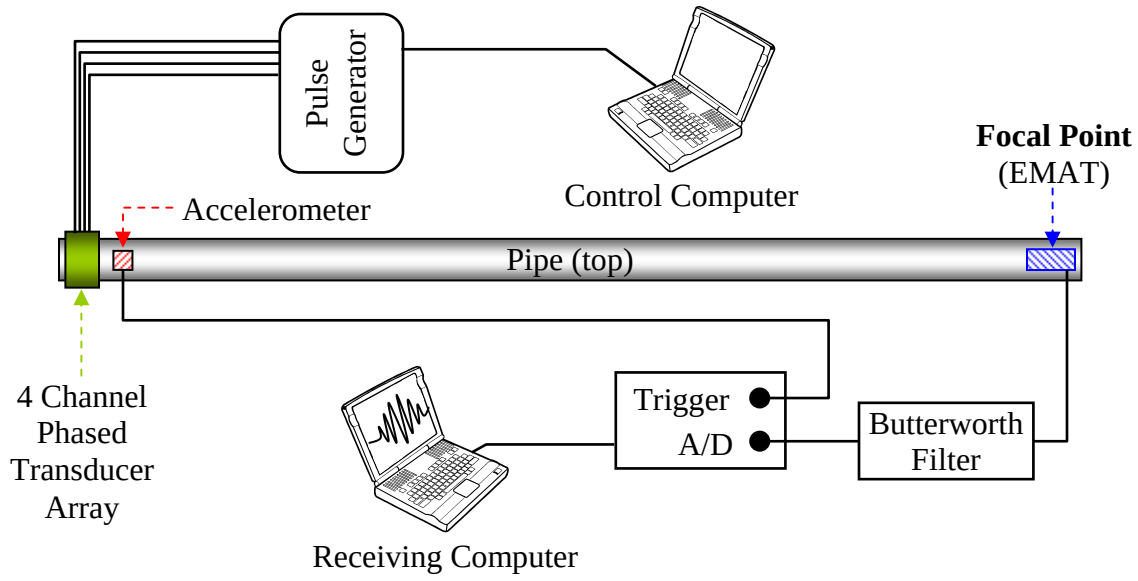

Figure 11.3 Experimental setup for guided wave focusing experiment.

All focusing experiments were performed on the 10 ft. coated pipe specimens described in the pipe specimen section. A 75 kHz, Hanning-windowed toneburst was used as an excitation signal with the transducers arranged in a manner so as to generate the first torsional mode, T(0,1). Time delays were calculated to produce a focal spot at the end of the pipe opposite to that of excitation and at the 90° circumferential position. An Electromagnetic Acoustic Transducer (EMAT) was place at this position to receive data (See Figure 11.3). Before being stored, data was passed through a Butterworth filter to remove frequency content outside the range of interest. EMAT data acquisition was triggered by an accelerometer placed near the point of wave excitation. For each coated specimen, and for a bare specimen, axisymmetric data was taken in addition to the focusing data. The axisymmetric data serves as a baseline with which to evaluate focusing ability. The focal spot was spun in 90° increments around the circumference of the pipe so as to obtain a rough focusing profile. If focusing was achieved, the energy at the 90° circumferential position was larger than that of any other circumferential position. Figures 11.4 through 11.11 show the experimental results for the different specimens, starting with the bare pipe specimen.

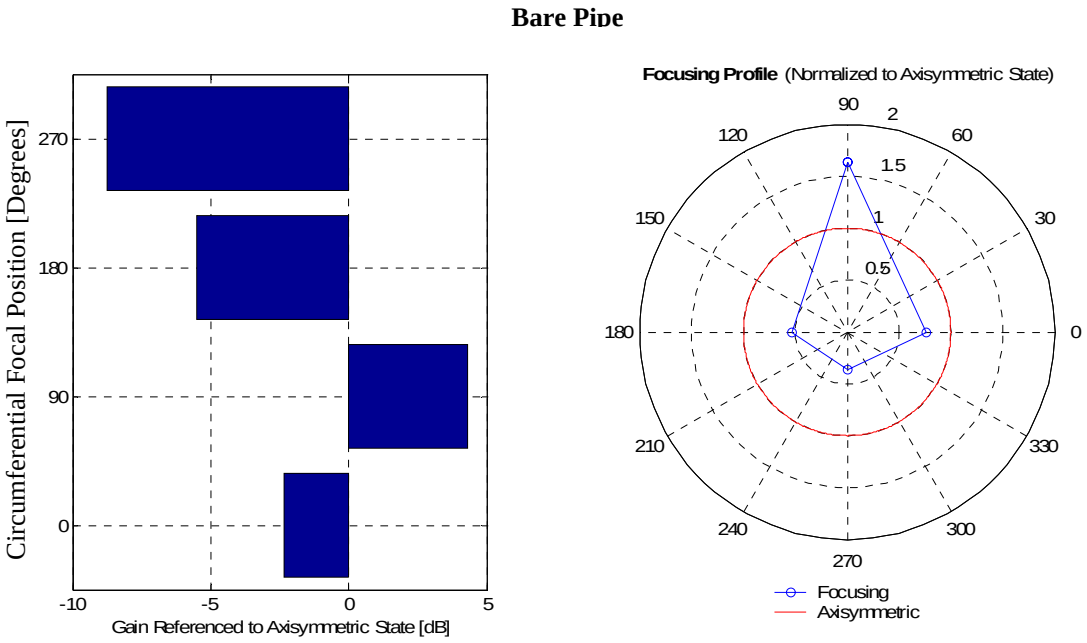

Figure 11.4 Focusing results for a bare pipe. The plot on the left shows the difference in dB as referenced to the axisymmetric amplitude. The figure on the right shows the focusing profile.

0.2mm Bitumastic 50 Coating

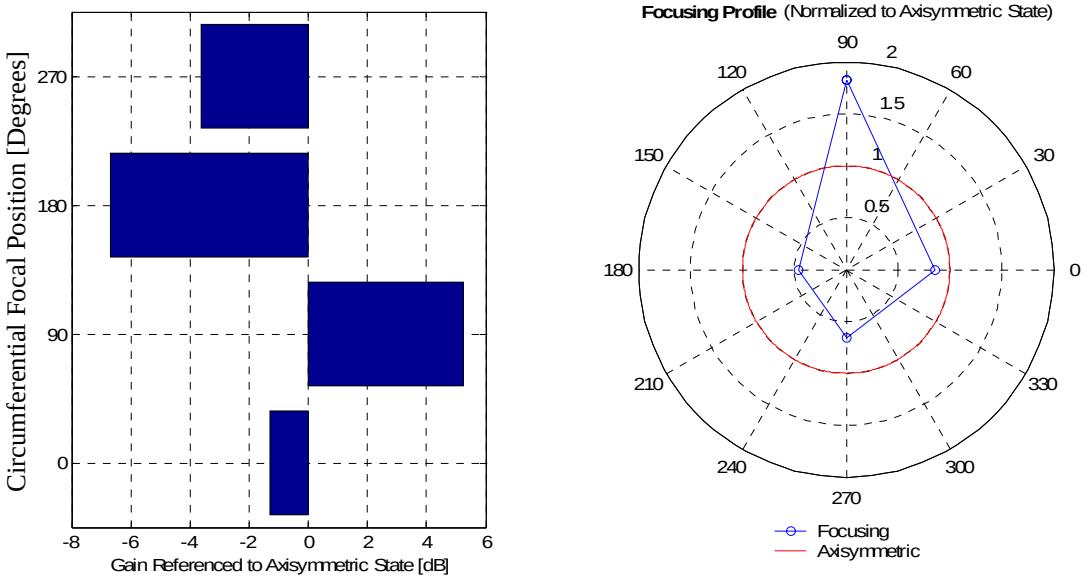

Figure 11.5 Focusing results for pipe with a 0.2mm Bitumastic 50 coal-tar mastic coating. The plot on the left shows the difference in dB as referenced to the axisymmetric amplitude. The figure on the right shows the focusing profile.

0.15mm Bitumastic 300M Coating

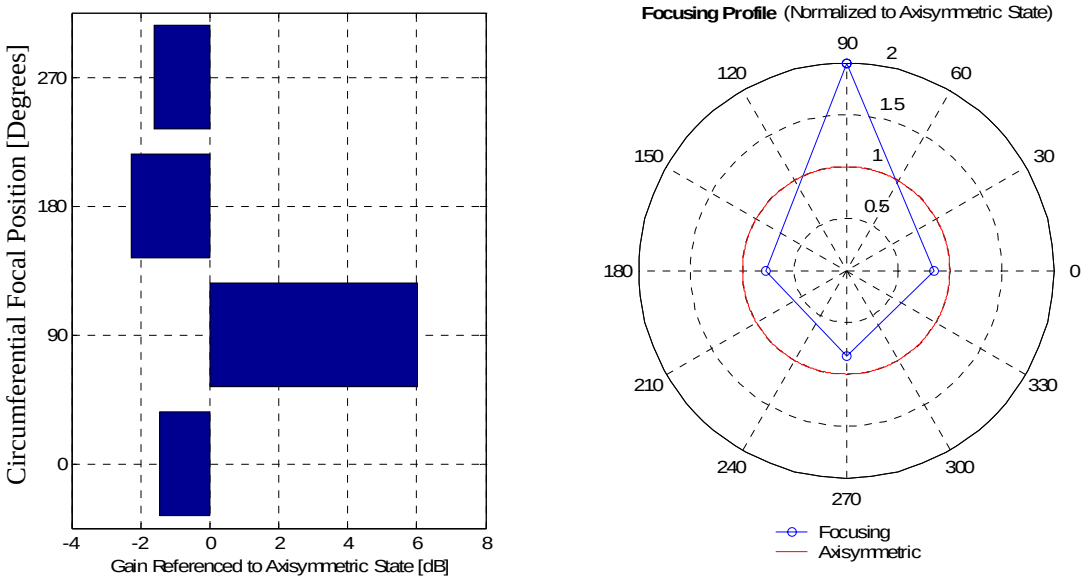

Figure 11.6 Focusing results for pipe with 0.15mm Bitumastic 300M coal-tar epoxy coating. The plot on the left shows the difference in dB as referenced to the axisymmetric amplitude. The figure on the right shows the focusing profile.

0.8mm Bitumen Tape

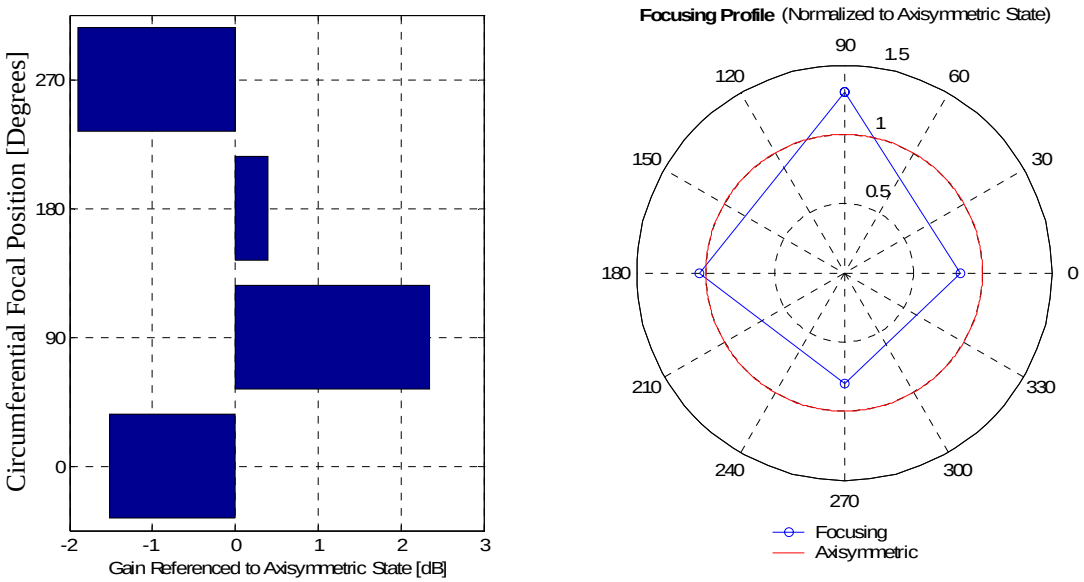

Figure 11.7 Focusing results for pipe with cold-applied 0.8mm bitumen tape coating. The plot on the left shows the difference in dB as referenced to the axisymmetric amplitude. The figure on the right shows the focusing profile.

0.25mm Single Layer FBE

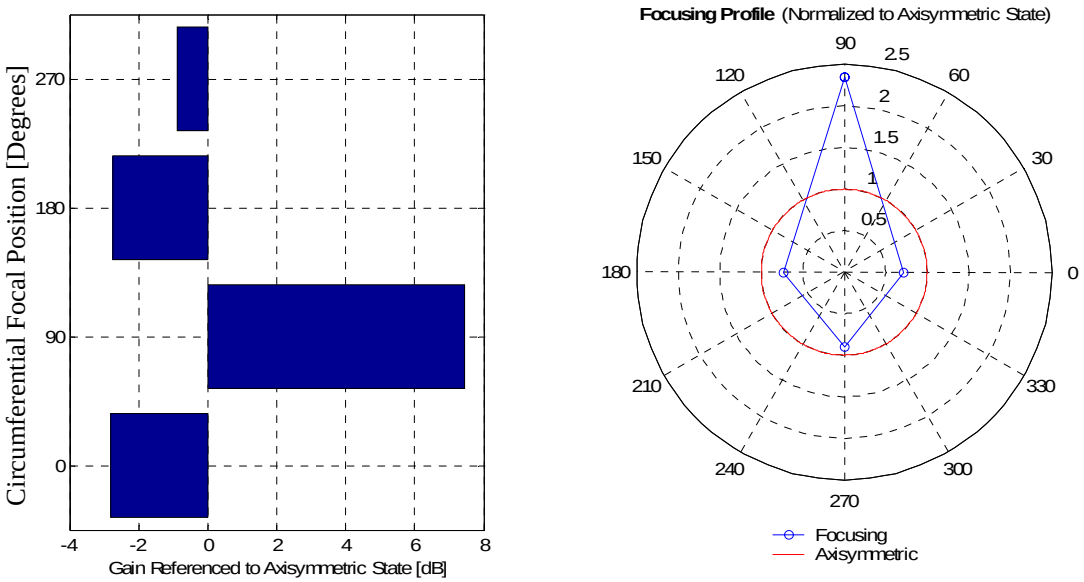

Figure 11.8 Focusing results for pipe with 0.25mm single layer fusion-bonded epoxy coating. The plot on the left shows the difference in dB as referenced to the axisymmetric amplitude. The figure on the right shows the focusing profile.

1.5mm Dual Layer FBE

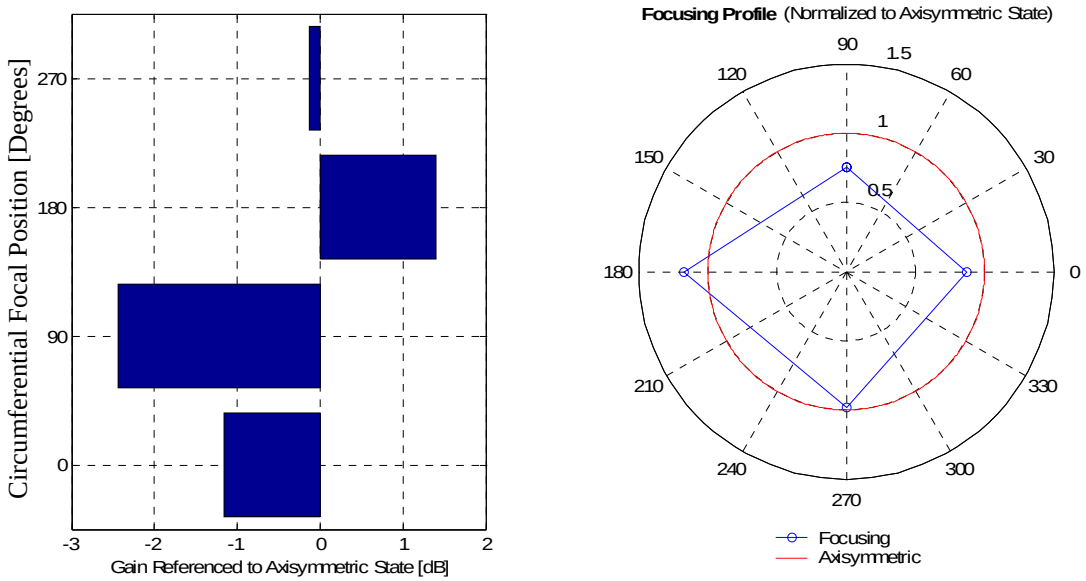

Figure 11.9 Focusing results for pipe with 1.5mm dual layer fusion-bonded epoxy coating. The plot on the left shows the difference in dB as referenced to the axisymmetric amplitude. The figure on the right shows the focusing profile.

0.13mm Enamel

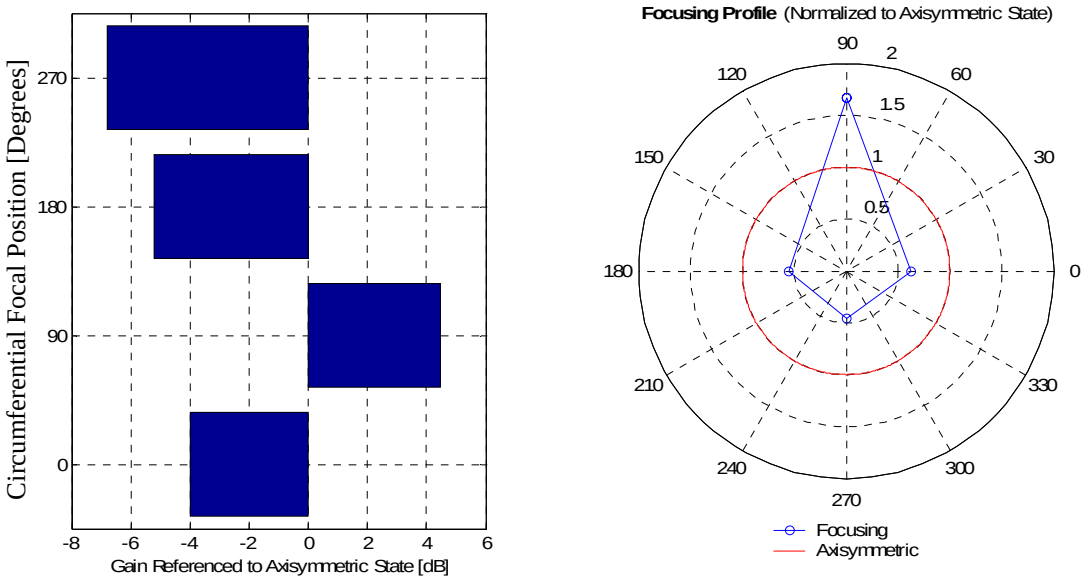

Figure 11.10 Focusing results for pipe with 0.13mm enamel paint coating. The plot on the left shows the difference in dB as referenced to the axisymmetric amplitude. The figure on the right shows the focusing profile.

2.5mm Wax Tape

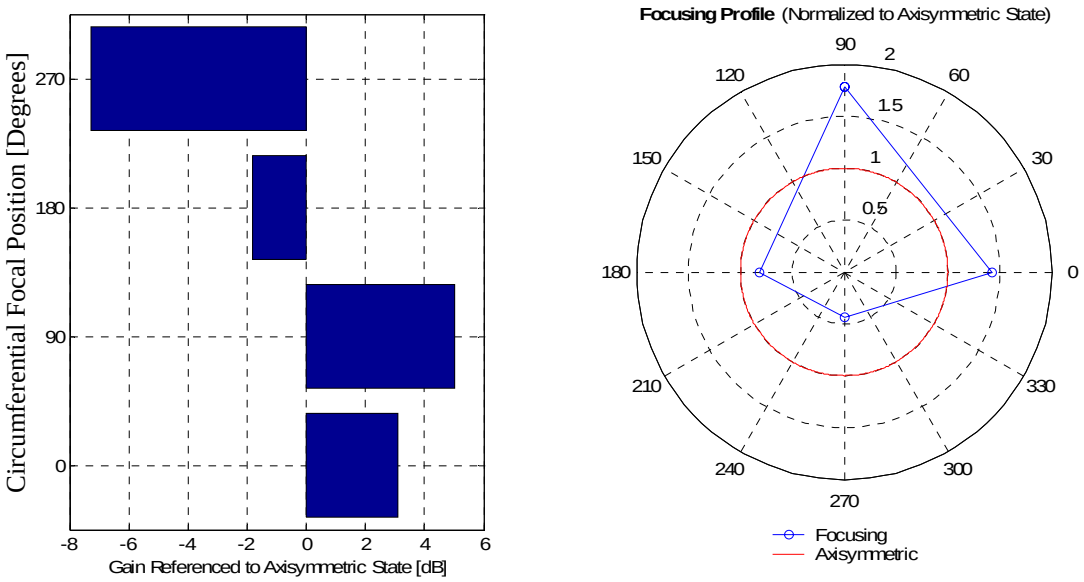

Figure 11.11 Focusing results for pipe with 2.5mm wax-wrap coating. The plot on the left shows the difference in dB as referenced to the axisymmetric amplitude. The figure on the right shows the focusing profile.

It can be seen from Figures 11.4 through 11.11 that focusing ability is undoubtedly affected by coating presence. It appears that for thin coatings the bare pipe approximations are acceptable. Some, but not all, of the thicker (>0.75mm) coatings inhibit focusing ability. The exception in this case is the wax coating, which does not seem to greatly affect focusing ability. This could be a result of bonding condition or some other characteristic of the coating and merits further attention. From this study it can be said that for some coating conditions, bare pipe approximations will no longer produce acceptable focusing results. A summary of the experimental results can be seen in Table 11.1.

Coating	Apprx. Thickness (mm)	Apprx. Focusing Gain (dB)
Bare Pipe	0	4
Bitumastic 50	0.2	5
Bitumastic 300M	0.15	6
Bitumen Tape	0.8	2.5
Single Layer FBE	0.25	7
Dual Layer FBE	1.5	-2.5
Enamel	0.13	4.5
Wax Tape	2.5	5

Table 11.1 Summary of focusing study results showing the coating type, approximate coating thickness, and the gain in dB compared to axisymmetric excitation.

It is important to note that the amplitude gain achieved by focusing translates directly into improved penetration power. This is illustrated in Fig. 11.12 for a typical gain value achieved for 4-channel focusing in a pipe with a thin coating.

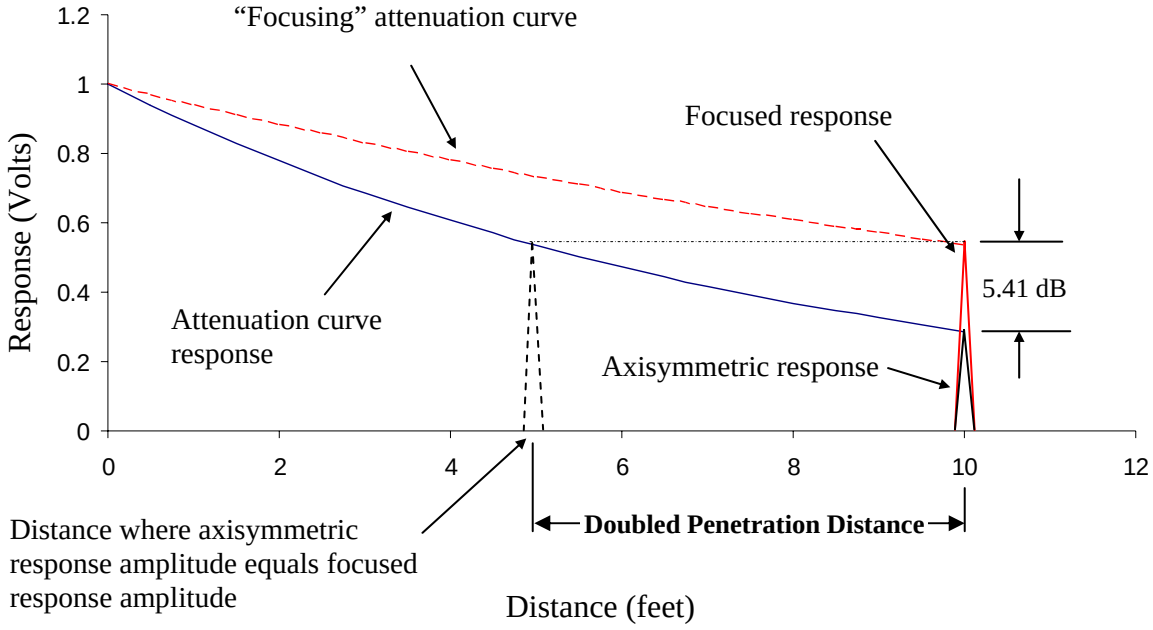

Figure 11.12 Illustration of the concept of penetration improvement with the use of focusing. The focusing response at 10 ft. is equivalent to the axisymmetric response at 5 ft. Thus 5 ft. of penetration has been gained.

Focusing ability can also be improved by increasing the number of phasing channels. Four channels were used in this experiment and in some cases, such as that in Figure 11.12, inspection distance was doubled. If eight channels are used for focusing, this improvement in penetration power is expected to increase even more, possibly by another factor of two. This will be investigated further in the future.

It has been shown that bare pipe approximations are acceptable for a majority of the coating types presented here. This approximation is expected to degrade as the focal distance becomes longer. For thin coatings, focal distances larger than 10 ft. have been achieved. It is still unclear how coating presence affects focal distance as long coated-pipe specimens are difficult to handle in a laboratory atmosphere and can often only be studied in the field. This is a point for future study.

12. Coating Interface Study

The coating bonding condition can have a dramatic effect on the attenuation of guided waves. Coatings that are intimately bonded to the surface of the pipe can generate much attenuation, even if very thin. Likewise, very thick coatings may not be as attenuative as expected if bonding conditions are not ideal. Additionally there are cases where a coating may have become disbonded from the pipe and groundwater has leaked into the interface.

An experiment was designed to analyze the effects of different bonding and interface conditions. Figure (12.1a) shows the experimental setup. Ultrasonic guided-wave data was collected on a 10 ft. steel pipe specimen using the first torsional and second longitudinal modes. The pipe was then wetted and a layer of Bitumen Tape was applied. Data was collected a second time and then the coating was removed. To replicate the effects of a dirty interface, the Bitumen Tape was covered with a thin soil layer. The clean and soiled coating images can be seen in Figure (12.1b) and (12.1c). Data was then collected a third time. Data taken on a similar pipe with a well-bonded Bitumen Tape coating was used for comparisons.

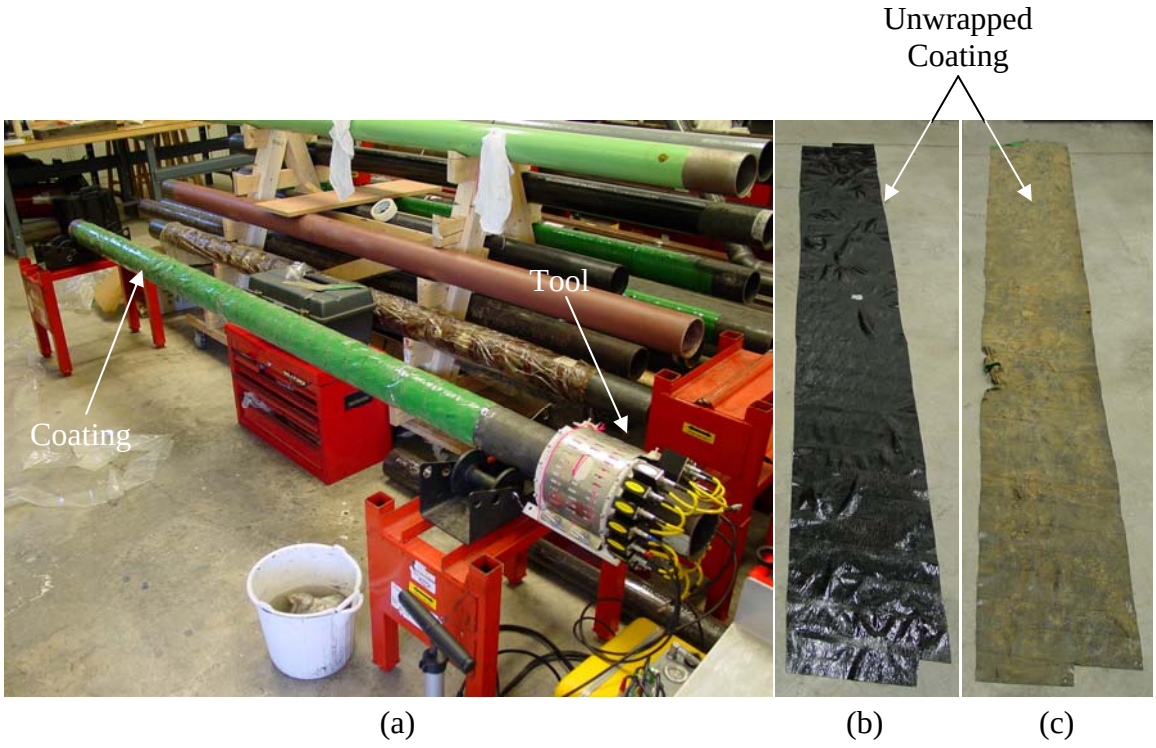

Figure 12.1 (a) Experimental setup for coating interface study. (b) Clean Bitumen Tape as was removed from the pipe after the water interface study. (c) Soiled Bitumen Tape used to simulate a dirty bonding condition.

Figure 12.2 shows the analytic envelope of an echo train obtained from the L(0,2) mode propagating in the bare pipe. To obtain the attenuation trend, the echo peaks were isolated and an exponential trend was then fit to the peak data. The blue line in Figure 2 shows the peak data with the blue circles representing the actual data points. The black dotted-line represents the exponential attenuation trend, normalized by the y-intercept value for comparison reasons.

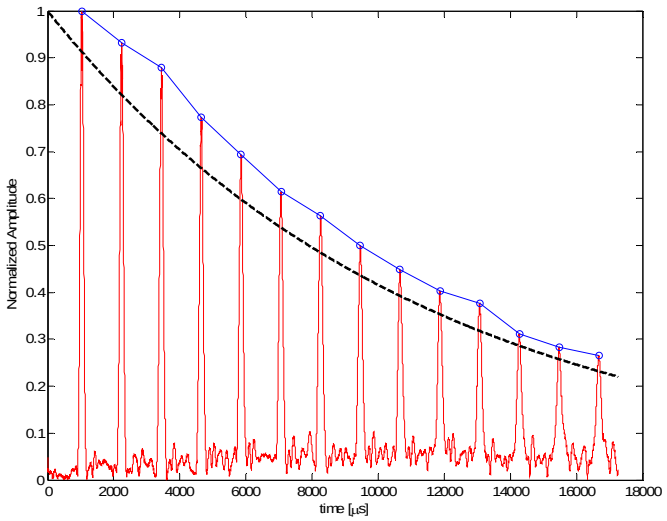

Figure 12.2 Analytic envelope of the RF waveform obtained from the L(0,2) mode propagating in a bare pipe. The red line is the analytic envelope. The blue line represents the echo-peak data, and the black line is a normalized exponential attenuation trend.

Using the technique illustrated in Figure 12.2, attenuation trends were generated for the different coating interface conditions. Figure 12.3, on the following page, shows the results for the second longitudinal mode. It can be seen that the presence of the coating, no matter the interface condition, introduces severe attenuation. The presence of water in the interface increases this attenuation compared to the clean interface. A possible reason for this is that the water acts as a coupling medium between the steel pipe and the Bitumen Tape coating. The soiled interface produces as slight decrease in attenuation compared to the clean interface condition. Again, a reason for this is that the dirty interface acts similarly to a very thin layer of air, which would result in less leakage into the coating because of the acoustic impedance mismatch.

Figure 12.4, on the following page, shows the attenuation results using the first torsional mode. It is interesting to see that the interface condition has very little effect on the guided-wave attenuation. It appears that there is a minute difference in the attenuation trends, with the water interface being more attenuative and the soiled interface being less attenuative, compared to the clean interface.

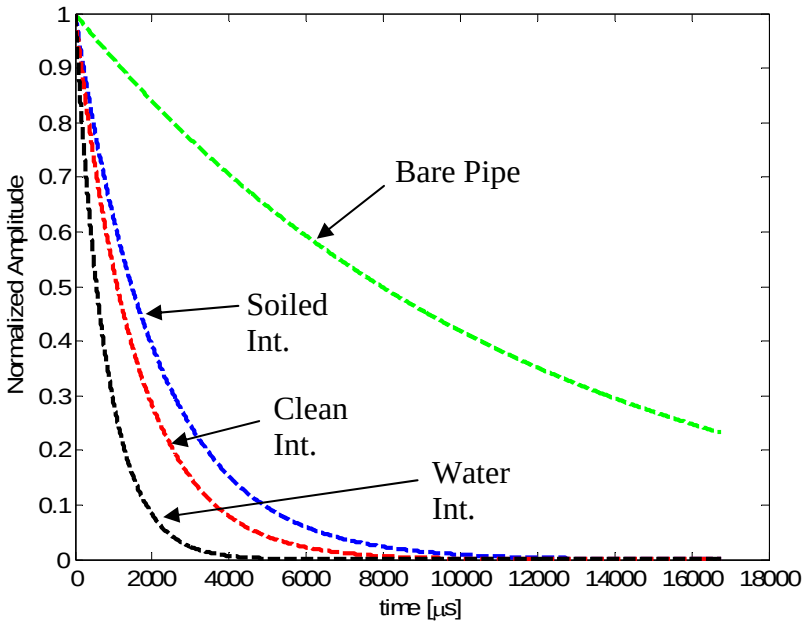

Figure 12.3 Attenuation trends of the L(0,2) mode for various coating interface conditions. The trends are labeled according to the interface (Int.) condition.

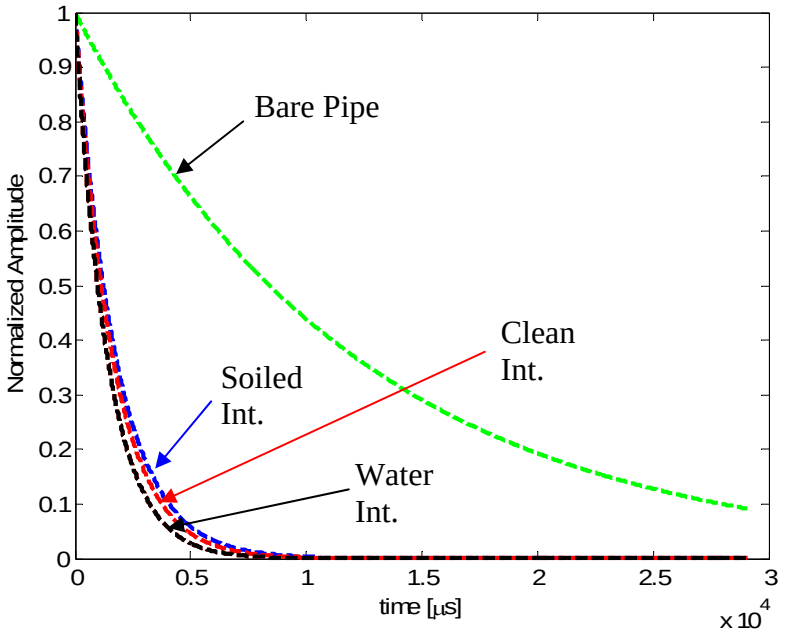

Figure 12.4 Attenuation trends of the T(0,1) mode for various coating interface conditions. The trends are labeled according to the interface (Int.) condition.

Discussion

This experiment demonstrates that the coating interface condition can have a noteworthy effect on the attenuation properties of guided waves. In this case study, the L(0,2) mode was sensitive to the different coating interface conditions, while the T(0,1) mode showed very little change for the different bonding conditions. In both cases, attenuation increased with the presence of water at the interface and decreased with the presence of soil, though, the changes were much more significant for the L(0,2) mode.

It must be noted that the results presented here pertain only to the specific coating and frequency used. The results may be entirely different for other coating types and thus more work is needed in this area. Future work will include interface modeling so that the effects of interface condition can be seen for different coatings. Pending modeling results, the coating evaluation tool will be adapted for coating bond characterization. This will be part of a Phase II effort.

13. Summary of Results

Sections 3 and 4 introduced ultrasonic techniques for measuring coating density, wave velocity, and bulk-wave attenuation. In Section 2, wave velocity and density measurements were presented for a wax coating and for a bitumen tape coating. Equations 3.8 and 3.9 show the density predictions for the wax and bitumen tape coatings, respectively. These values were obtained from the reflection coefficients which are plotted in Figure 3.4 for the wax coating and Figure 3.5 for the bitumen coating. The results obtained for the bitumen tape were shown to agree well with a density measurement obtained by gas pycnometry by Luo [2005].

Two techniques for the measurement of bulk-wave attenuation were introduced in Section 4, one for thick coatings and another for thin coatings. Experimental results obtained using the technique for thick coatings were presented for the wax coating (Figure 4.4) and for the bitumen tape coating (Figure 4.5) introduced in Section 3. Results for two thin coatings, a coal-tar epoxy (Figure 4.7) and a fusion-bonded epoxy (Figure 4.10) were also shown. The attenuation trends obtained were as expected, showing linear trends, tending toward zero attenuation at zero frequency.

Section 5 presented a study showing that the measured coating material properties produced a reliable guided-wave attenuation prediction. Figure 5.2 shows the experimentally obtained, guided-wave results and Figure 5.3 shows the predicted guided-wave attenuation results, based on the measured coating properties. Table 5.1 shows that, when ordered from least attenuative to most attenuative, the predicted results match the experimental results perfectly. This is a critical study which demonstrates the ability of the coating property measurement techniques to produce accurate guided wave attenuation results.

The theoretical dispersion curve study presented in Section 6 provided useful information on the effect of each material parameter on the dispersion trends. It can be seen in Figure 6.5 and 6.6 that coating thickness plays a critical role in guided-wave attenuation. Similarly, Figures 6.2 and 6.4 show that variations in coating density and thickness produce noticeable changes in the phase velocity dispersion curves. It can be seen in Figures 6.2 through 6.10 that low frequencies are less affected by the variation in parameters with the L(0,1) mode being the most sensitive to changes and the L(0,2) being the least sensitive. It was also shown in Section 6 that the shear wave velocity and attenuation could be estimated from the longitudinal properties with little effect on the dispersion curves.

Section 7 introduced a conceptualization for a handheld coating characterization tool. A first generation prototype of the sensor package which would accompany such a tool was designed and built and can be seen in Figures 7.3 and 7.4. The sensor package consists of a linear-inductance thickness gauge and a longitudinal bulk-wave transducer. The sensor housing was designed to include an interchangeable, acrylic, delay-line with a machined pipe conformity and docking station for the linear-inductance sensor. The sensor package

was field tested at NY Search's Johnson City, NY test facility with superb results, as seen in Section 8. Table 8.1 summarizes the measured coating properties for the two coatings analyzed: a fusion-bonded epoxy coating and a fibrous coal-tar coating. The predicted guided-wave attenuation plots for the fusion-bonded epoxy and fibrous coal-tar coatings can be seen in Figures 8.5 and 8.10 respectively. The predicted results agreed well with a guided-wave inspection study that was being performed concurrently, by FBS, inc., as part of a Northeast Gas Association study.

Table 9.1 in Section 9 lists the calculated complex material properties used for the finite-element modeling presented in Section 10. Wave propagation in three different pipes was modeled in Section 10, a bare pipe, a wax-coated pipe, and a dual-layer fusion-bonded epoxy-coated pipe. Leakage of the Von Mises Stress, from the pipe into the coating, was visualized and can be seen in Figures 10.3 and 10.4. Figure 10.2 shows that, in addition to being highly attenuative, the presence of the wax coating slows the group velocity by a small amount. This is critically important information for the precise location of defects as well as for guided-wave focusing algorithms. Attenuation trends for the three models agreed with experimental and predicted attenuation rates.

Section 11 presented the results of a guided-wave focusing study for a bare pipe and the seven different coated specimens studied in the laboratory. Figure 11.12 illustrates the idea of improved penetration power achieved by focusing. Table 11.1 summarizes the focusing results. It was found that focusing improves penetration power for 7 out of the eight specimens. It was shown that the focusing profile for the dual-layer fusion-bonded epoxy-coating (Figure 11.9) was not shaped as expected, based on the focusing calculations for a bare pipe. Penetration in the pipe with bitumen tape coating was improved by focusing but only by 2.5dB as compared to axisymmetric excitation. This was much less than the 5.25dB average gain achieved for the other coating types. This suggests that for some coating types, bare-pipe approximations will not suffice for focusing calculations. More work is needed in this area to understand exactly which parameters affect focusing ability, although two suspect properties are coating thickness and bonding condition.

A bond interface study was presented in Section 12. Clean, wetted, and soiled interface conditions were experimentally simulated so as to see the effect on guided-wave attenuation. Figure 12.3 shows that the L(0,2) mode, at the frequency studied, was highly sensitive to the interface condition, with increased attenuation caused by the wet interface and decreased attenuation caused by the soiled interface. Figure 12.4 shows that the T(0,1) mode is relatively inert to the bond condition at the frequency studied. Further work is needed in this area, including finite-element modeling of various bonding conditions. Based on the results of these future studies, the VECTOR tool may be modified to include a bond characterization routine.

14. Proposal for Future Work

A feasibility study has been completed and a protocol for the evaluation of viscoelastic coating properties has been developed and proven. Based on this protocol, the prototyping of a coating evaluation tool, called VECTOR, has begun. Field-testing of the VECTOR instrument at NY Search's test facility in Johnson City, NY has produced very promising results in addition to creating some excitement among industry members. Using the developed protocol and VECTOR tool, a coating database has been started.

It has been demonstrated that coating presence has an effect on focusing capability and further consideration of this influence is needed. Additionally, it has been shown that coating bonding condition also influences guided wave attenuation to some degree. More work is needed in these areas. The finite-element techniques demonstrated in this report will play a vital role in this future work.

Based on the work contained within this report, the following areas of future research and development are proposed for a Phase II effort:

- Full development of the VECTOR instrument, including robust, integrated, handheld computer with spike-pulser, A/D board, and graphical user interface.

- In-depth study of the effects of viscoelastic coatings on guided wave focusing ability with new focusing algorithms which will account for said effects.

- Further finite-element modeling and experimental investigation of coating interface influence on guided wave propagation and attenuation.

- Continued evaluation and databasing of coating samples obtained from willing parties and field test opportunities.

- Continued integration efforts into the ongoing, long range, guided-wave inspection efforts of the DOT.

15. References

Barshinger, J.N., *Guided Wave Propagation in Pipes With Viscoelastic Coatings*, Ph.D. Thesis, The Pennsylvania State University, 2001.

Christensen, R.M., *Theory of viscoelasticity : an introduction,* Academic Press, 1981.

Graff, K.F., *Wave Motion in Elastic Solids,* Ohio State University Press, OH, 1975.

Guo N., Lim M.K, Pialucha T., "Measurement of Attenuation Using a Normalized Amplitude Spectrum", *Journal of Nondestructive Evaluation,* **14**(1), 9-19, 1995.

Haddad, Y.M., *Viscoelasticity of engineering materials,* Chapman & Hall, London, U.K., 1995.

Haines N.F., Bell J.C., McIntyre P.J., "The Application of Broadband Ultrasonic Spectroscopy to the Study of Layered Media", *Journal of the Acoustical Society of America*, **64**(6), 1645-1651, 1978.

Kline R.A., "Measurement of Attenuation and Dispersion Using an Ultrasonic Spectroscopy Technique", *Journal of the Acoustical Society of America,* **76**(2), 498-504, 1984.

Luo, W., *Ultrasonic Guided Waves and Wave Scattering in Viscoelastic Coated Hollow Cylinders*, Ph.D. Thesis, The Pennsylvania State University, 2005.

Mak D.K., "Comparison of Various Methods for the Measurement of Reflection Coefficient and Ultrasonic Attenuation", *British Journal of NDT,* **33**(9), 441-449, 1991.

Progress Reports, subcontracted to NY Search (NE Gas) under DOT, contract on, "*Validation and Enhancement of Long Range Guided Wave Ultrasonic Testing: A Key Technology for Direct Assessment of Buried Pipeline*", 2005-2006.

Rose, J.L., *Ultrasonic Waves in Solid Media,* Cambridge University Press, Cambridge, U.K., 1999.

Zhang, L., *Guided Wave Focusing Potential in Hollow Cylinders*, Ph.D. Thesis, The Pennsylvania State University, 2005.